Technische Universität München

Exploring the Island of Inversion with the d(^{30}Mg, p)^{31}Mg Reaction

Dissertation
von
Vinzenz Bildstein

Lehrstuhl E12 für Experimentalphysik
Technische Universität München

Technische Universität München
Physik-Department E12

Exploring the Island of Inversion with the d (^{30}Mg, p) ^{31}Mg Reaction

Vinzenz Bildstein

Vollständiger Abdruck der von der Fakultät für Physik der Technischen Universität München zur Erlangung des akademischen Grades eines

Doktors der Naturwissenschaften (Dr. rer. nat.)

genehmigten Dissertation.

Vorsitzende:	Univ.-Prof. Dr. N. Brambilla
Prüfer der Dissertation:	
	1. Univ.-Prof. Dr. R. Krücken
	2. Univ.-Prof. Dr. P. Fierlinger

Die Dissertation wurde am 08.11.2010 bei der Technischen Universität München eingereicht und durch die Fakultät für Physik am 07.12.2010 angenommen.

Contents

Abstract

In this thesis the results of a d(^{30}Mg, p)^{31}Mg experiment at REX-ISOLDE are presented. ^{31}Mg is located directly on the border of the so-called ''Island of Inversion'', a region of the nuclear chart around ^{32}Mg where deformed intruder states of the fp shell form the ground states of the nuclei instead of the normal spherical states of the sd shell. A recent experiment has shown the ground state of ^{31}Mg to be a $1/2^{+}$ state and indicates more than 90 % intruder configuration. The question whether the low-lying excited states of ^{31}Mg are deformed intruder states as well or rather spherical states from the sd shell, indicating shape coexistence, is still open. The d(^{30}Mg, p)^{31}Mg reaction is thus a good tool to gain more insight into the nature of the Island of Inversion. In the framework of this thesis the angular distribution of protons was measured for the second excited state at 221 keV in coincidence with de-excitation γ-rays. The angular distribution was compared to DWBA calculations for different transferred orbital momenta, identifying the state for the first time as an $l = 1$ state.

The experiment was performed with the new charged particle detector setup T-REX. The setup is optimized for transfer reactions with radioactive beams in inverse kinematics. T-REX was developed, built, installed, and used for this first one neutron transfer experiment in the context of this thesis. The T-REX setup consists of ΔE - E$_{\mathrm{Rest}}$ telescopes made out of position sensitive silicon detectors that cover almost 4π of the solid angle and can be combined with the MINIBALL γ-ray detector array. It has a large solid angle for the detection and identification of the light recoils from transfer reactions. T-REX allows in combination with the MINIBALL Germanium detector array the tagging of the excited states by their characteristic γ-rays. The combination of T-REX and MINIBALL achieves an optimum resolution of excitation energies.

A whole series of experiments with the new detector array has been performed at REX-ISOLDE, using one and two neutron transfer reactions and beams ranging from ^{11}Be to ^{78}Zn.

The detector concept and experimental details are presented together with the newly developed analysis framework. The extracted γ-spectra, angular distributions, and transfer cross section scaling factors allow a deeper insight to the structure of ^{31}Mg.

Zusammenfassung

In dieser Arbeit werden die Ergebnisse eines d(^{30}Mg, p)^{31}Mg Experiments bei REX-ISOLDE vorgestellt. ^{31}Mg liegt auf der Grenze der sogenannten ''Insel der Inversion'', einer Region der Nuklidkarte um ^{32}Mg, in der deformierte Intruderzustände aus der fp-Schale die Grundzustände bilden, anstelle der normalen, sphärischen Zustände der sd-Schale. Es wurde in einem Experiment jüngst gezeigt, daß der Grundzustand von ^{31}Mg ein $1/2^+$ Zustand ist, und der Anteil von Intruderkonfigurationen an der Wellenfunktion mehr als 90 % beträgt. Die Frage, ob die niedrig liegenden angeregten Zustände von ^{31}Mg ebenfalls deformierte Intruderzustände sind oder doch sphärische Zustände der sd-Schale, ist noch offen. Die ^{30}Mg Reaktion ist ein gutes Werkzeug, um mehr Informationen über die Natur der Insel der Inversion zu erhalten. Im Rahmen dieser Arbeit wurde die gemessene Winkelverteilung von Protonen in Koinzidenz mit γ-Strahlen aus der Abregung des 221 keV Zustandes in ^{31}Mg mit DWBA Rechnungen für verschiedene transferierte Bahndrehimpulse verglichen. Daruch wurde der Zustand eindeutig als $l = 1$ Zustand identifiziert.

Das Experiment wurde mit dem neuen T-REX Aufbau zum Nachweis von geladenen Teilchen mit positionsauflösenden Silizium-ΔE - E$_{\mathrm{Rest}}$-Teleskopen durchgeführt. Im Rahmen dieser Doktorarbeit wurde T-REX für Transferexperimente mit radioaktivem Strahl in inverser Kinematik bei REX-ISOLDE entwickelt, aufgebaut und speziell für den Einsatz zusammen mit dem MINIBALL Germanium-Spektrometer optimiert. T-REX deckt einen großen Raumwinkel von fast 4π ab und erlaubt die Identifikation der leichten Rückstoßkerne von Transferreaktionen. Die Kombination von T-REX mit dem MINIBALL Germanium-Spektrometer ermöglicht es, in Transferreaktionen erzeugte angeregte Zustände anhand ihrer charakteristischen γ-Strahlung zu identifizieren, und erreicht eine optimale Auflösung der Anregungsenergie.

Das Detektorkonzept und Details des experimentellen Aufbaus werden zusammen mit der neu entwickelten Analysesoftware vorgestellt. Die extrahierten γ-Spektren, Winkelverteilungen und Skalierungsfaktoren für die Transferwirkungsquerschnitte erlauben einen tieferen Einblick in die Struktur von ^{31}Mg.

Chapter 1

Introduction

One of the most successful concepts in nuclear structure is the shell-model as first introduced by Jensen and Mayer [Hax49, Goe49], which correctly predicts the experimentally observed ''magic numbers''. A nucleus is said to be ''magic'' if the single-particle energy gap between the last filled orbital and the next empty orbital is large compared to the next orbital below. For these nuclei residual interactions, which are weaker than the energy gap in the single-particle spectrum, induce only weak correlations, so that the nuclei exhibit typical single-particle properties.

If on the other hand the gap between the orbitals is small or a shell is only partially filled, the residual interactions can easily promote nucleons to single-particle states at higher energies leading to a more collective behavior.

The established ''magic numbers'' (2, 8, 20, 28, 50, 82, and 126) can be easily reproduced by the shell-model (if it includes the spin-orbit interaction) along with the properties of the low-lying states of most stable nuclei. The magic numbers were for a long time thought to be universal across the chart of nuclei.

In 1975 however, mass measurements by Thibault *et al.* [Thi75] showed deviations for ^{31,32}Na from the expected masses for a closed neutron shell $N = 20$, that could not be explained by the shell model. The increased masses and two-neutron separation energies were explained by Campi *et al.* [Cam75] to arise from the deformation of the exotic sodium isotopes due to the filling of the $f_{7/2}$ orbital intruding into the sd shell.

This was evidence that the established shell gaps can disappear and new shell gaps may appear when going away from the ''valley of stability'' and the region where this inversion of the ordering of orbitals was first observed was called ''Island of Inversion''. The discovery of the Island of Inversion and the advancement of the technical possibilities to study nuclei further away from stability has led to a multitude of experiments probing the nature of the change in shell structure around $N = 20$ and other magic numbers.

One explanation for the change of the shell structure is the monopole component of the residual interaction. It shifts the single-particle energies leading to effective single-particle energies and can lead to the closing of the classic shell gaps and the opening of new gaps [Ots01]. This can explain the disappearance of the $N = 20$ shell in the oxygen isotopes, leading to an unbound ^{28}O, while ^{24}O was shown to be doubly magic [Kan09, Ots10a] with the new shell closure $N = 16$.

Recent work by Otsuka and collaborators [Ots01, Ots02, Ots05, Ots06, Ots10b] showed that the effect of the monopole part of the residual interaction could explain many of the observed changes in nuclear shell structure. This interaction is strongly

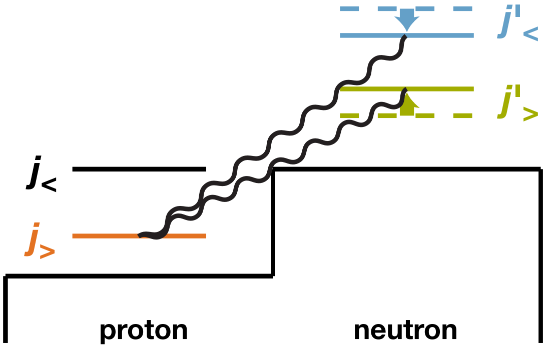

Figure 1.1: Monopole part of residual interaction acting between protons and neutrons in orbits $j_> = l + 1/2$ and $j'_< = l' - 1/2$.

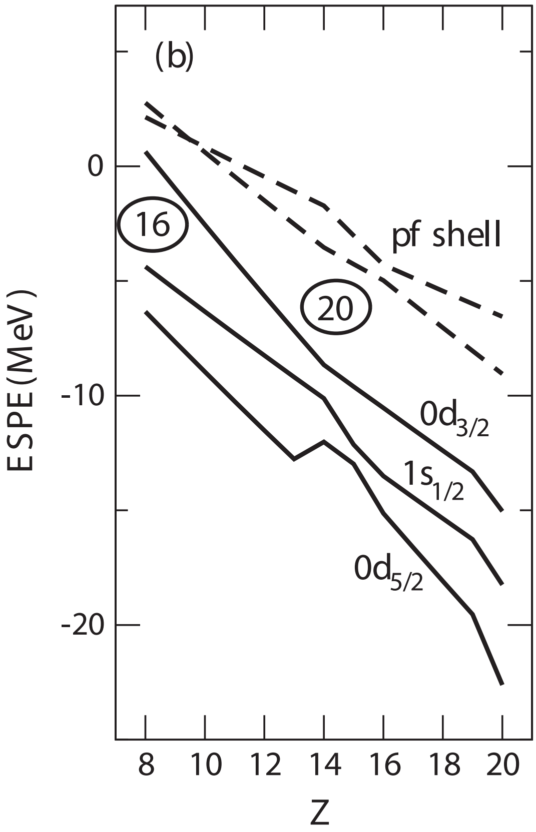

Figure 1.2: Effective single-particle energies for $N = 20$ isotones. The removal of protons from the $\pi d_{5/2}$ orbital ($j_>$) reduces their attractive interaction on the neutron in the $\nu d_{3/2}$ orbital ($j_<$). This leads to a disappearance of the $N = 20$ shell gap and the opening of a new $N = 16$ shell closure for the oxygen isotopes. Adopted from [Ots02].

attractive between protons and neutrons that occupy orbitals with different couplings of orbital angular momentum and spins (meaning $j_> = l + 1/2$ and $j'_< = l' - 1/2$) as shown in figure 1.1.

The effective single-particle energies for the $N = 20$ isotones are shown in figure 1.2. As long as the $\pi d_{5/2}$ shell ($j_>$) is filled, the $\nu d_{3/2}$ shell ($j_<$) is pulled down by it. Going from $Z = 14$ to $Z = 8$ the $\pi d_{5/2}$ shell is emptied and the attractive force between the protons in this shell and the neutrons in the $\nu d_{3/2}$ shell is diminished. This results in the closing of the $N = 20$ shell gap and the opening of the $N = 16$ gap. For the oxygen isotopes the $\nu d_{3/2}$ shell is above the Fermi energy leading to ^{24}O as the heaviest bound oxygen isotope while adding just one proton pulls it down far enough to allow six more neutrons to be bound in the fluorine isotope ^{31}F.

For the isotopes in the Island of Inversion (around the $N = 20$ isotope ^{32}Mg) neither $N = 20$ nor $N = 16$ are good shell gaps so that quadrupole correlations between the

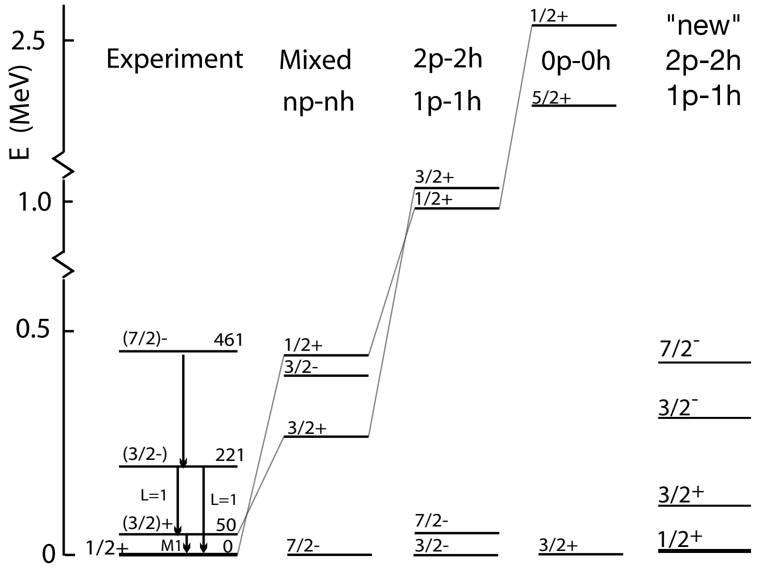

Figure 1.3: Low-lying experimental level scheme of ^{31}Mg, compared to various shell model calculations. The theoretical calculations are from left to right, a Monte Carlo shell model code in the $sd - p_{3/2}f_{7/2}$ space, the ANTOINE shell model code in the full $sd - pf$ space with one/two neutrons blocked in the pf-shell, a calculation using the USD interaction with only the sd space, assuming a $N = 20$ shell closure, and finally the calculation from [Mar05] which reproduces the experimental spin assignment and yields more than 90 % intruder configuration for the ground and the first excited state. Adopted from [Ney05] and [Mar05].

valence nucleons can be as large as the gaps between the single-particle energies of different orbits. These correlations can lower deformed intruder configurations from the fp-shell, resulting in low-lying collective excitations, shape coexistence, and deformed ground states.

1.1 Neutron Rich Magnesium Isotopes

One method to determine the collectivity of a nucleus is the Coulomb excitation method (sometimes abbreviated to Coulex). In Coulomb excitation experiments the projectile (target) is excited by the electromagnetic field of the target (projectile). The excitation cross section for pure Coulomb excitation can be expressed by the same electromagnetic multipole matrix elements that characterize the electromagnetic decay of the involved nuclear states.

The determination of the Coulomb excitation cross section thus allows studying the electromagnetic properties of the low-lying nuclear states from which the collectivity and deformation of the nucleus can be determined. For example, one can extract from the excitation cross sections the reduced matrix element $B(E2\!\uparrow) = B(E2;\, 0^+_{\mathrm{gs}} \rightarrow 2^+_1) \propto Q^2 \propto \beta^2$ for the quadrupole transition from the ground state to the first excited 2^+ state.

Coulomb excitation experiments performed at REX-ISOLDE have shown that ^{30}Mg has a very low $B(E2\!\uparrow)$ value that is consistent with a sd-shell configuration

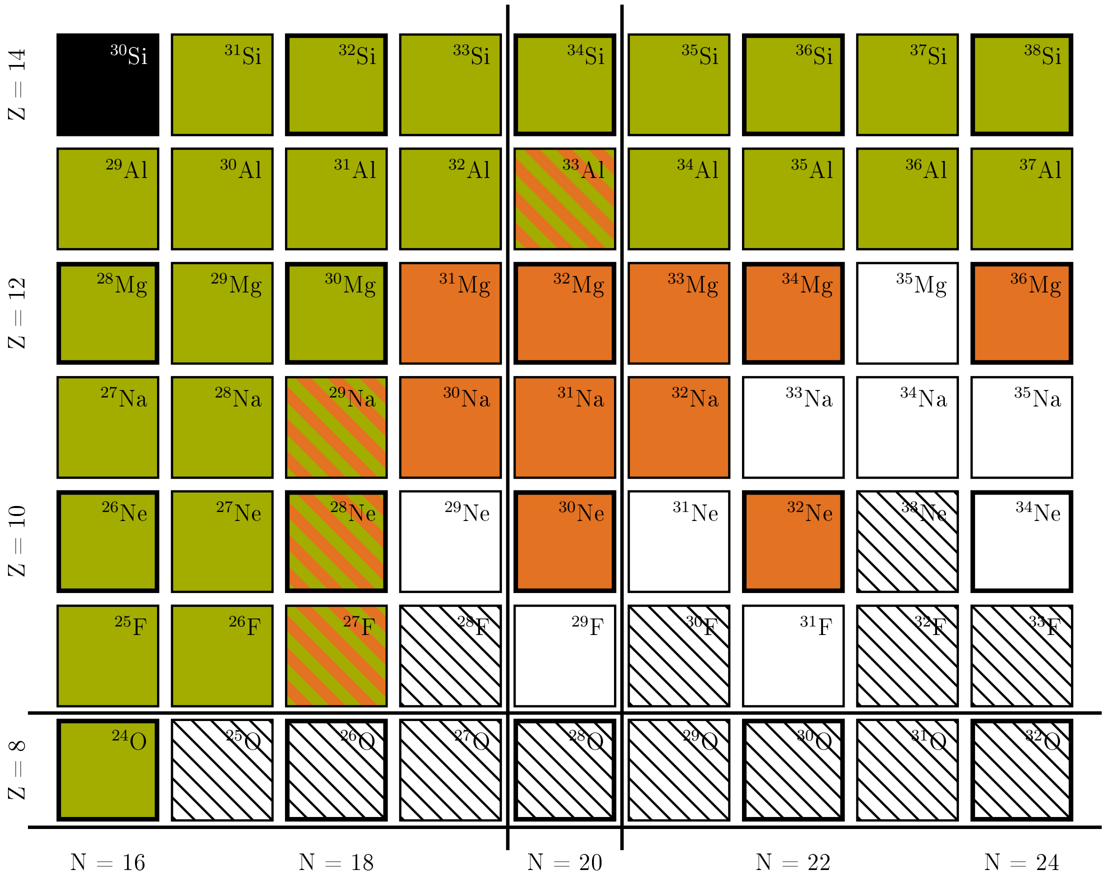

Figure 1.4: The region of the nuclear chart where the Island of Inversion lies. Nuclei whose ground states are dominated by normal sd configurations are shown in green, those dominated by the deformed fp intruder configurations in orange. The nuclei with ground states that are mixtures of both are shown in orange-green stripes. Empty squares and hatched squares represent nuclei were the configuration is unknown and unbound nuclei, respectively.

while ^{32}Mg has a large $B(E2\!\uparrow)$ value which indicates a deformed ground state and the disappearance of the $N = 20$ gap [Nie05, Mot95].

The measurement of the spin and parity of the ground state of ^{31}Mg, which should thus lie directly on the "shore" of the Island of Inversion, yielded a $1/2^+$ ground state [Ney05]. This was only reproducible using a residual interaction which results in more than 90 % intruder configuration from the fp-shell [Mar05], see also figure 1.3, indicating a very abrupt change in the ground state configuration going from ^{30}Mg to ^{31}Mg. It also leads to the question what the configurations of the excited states are and whether their so far only tentative spin assignments [Klo93, Ney05, Mac05, Ter08, Mil09] are indeed correct.

Transfer reactions are an excellent tool to study the single-particle properties, especially of the excited states, and will be discussed in the next chapter. One possibility to study the single-particle properties of the excited states in ^{31}Mg is the d (^{30}Mg, p) ^{31}Mg transfer reaction in inverse kinematics.

Such an experiment was already performed at MINIBALL in 2003 [Pan05], using a setup with a small angular coverage. The data from this experiment showed the need for a new setup better suited for transfer reactions in inverse kinematics since the limited ϑ range covered by the particle detector made it impossible to unambiguously assign an orbital angular momentum to the second excited state at 221 keV.

This thesis comprises the design and construction of such a new setup, called T-REX, which will be presented in chapter 3. Chapter 4 describes the analysis software that was written to analyze the data taken with the new setup. The results of the d $(^{30}\text{Mg}, \text{p})\,^{31}\text{Mg}$ experiment that was performed in the frame of this thesis, are presented in chapter 5 where the experimentally obtained angular distributions are compared to DWBA[1] calculations. The last chapter summarizes the results and gives an outlook on the rich experimental program that was started by the construction of T-REX.

---

[1] **D**istorted **W**ave **B**orn **A**pproximation

Chapter 2

Transfer Reactions

In the first part of this chapter the theoretical description of transfer reactions using the DWBA theory will be briefly presented, based on a recent book on nuclear reaction theory [Tho09]. The second part will concentrate on the special properties of transfer reactions in inverse kinematics and the challenges they pose. The last part will outline the Nilsson model, which can be used to describe deformed nuclei.

2.1 Theoretical Description of Transfer Reactions

In few nucleon transfer reactions one or more nucleons are transferred from the projectile to the target or vice versa. These transfer reactions are direct reactions in such as they involve only very few nucleons on the surface of the nuclei. As a direct reaction a one-nucleon transfer reaction can be modeled in the simplest case as a one-step transition between the initial and final scattering states.

At lower energies (below or at the Coulomb barrier) compound reactions are possible, where the projectile and the target form a highly excited compound nucleus, which de-excites via particle emission (mostly neutrons, protons, and α-particles). Compound reactions can have a high cross-section and create a large background of particles, which are emitted isotropically in the center of mass system. They have to be either accounted for by subtracting the isotropic background from the (in most cases) forward peaked angular distributions of the transfer reactions or suppressed by tagging the transfer reactions with γ-rays emitted from the excited states of the ejectile. For the latter case all compound reaction channels that do not populate the same final state as the transfer reaction are suppressed. This means that for neutron transfer reactions on neutron rich nuclei the cross-section for populating the same nucleus via a compound reaction is very small since it is unlikely that the neutron rich compound nucleus emits one (strongly bound) proton and no (weakly bound) neutron.

2.1.1 DWBA

To best describe experimentally observed elastic scattering cross sections, the effective interaction of the nuclei needs to have a negative imaginary part. This imaginary part describes the flux that is removed from elastic scattering by other competing reactions. Potentials that have such a form of real and negative imaginary part are called optical potentials for the similarity of their description of the refraction and absorption of flux to that of light passing through a cloudy refractive medium.

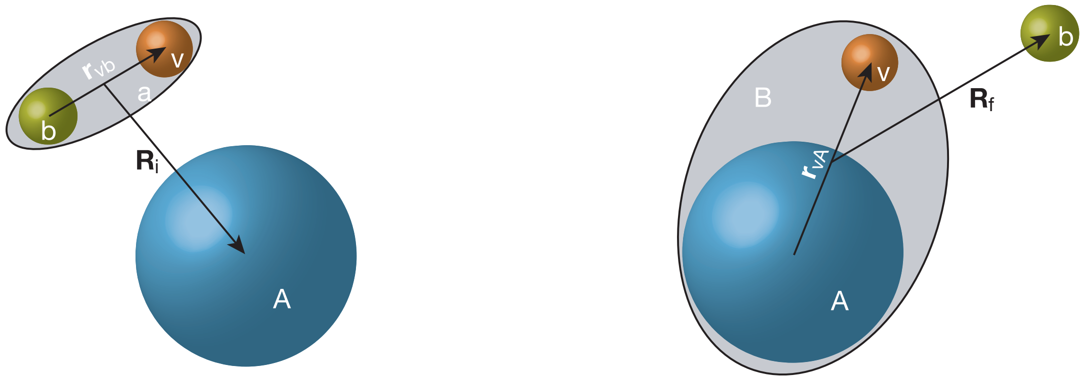

entrance channel

exit channel

Figure 2.1: Illustration of a transfer reaction $A(a,b)B$, where $a = b + v$ transfers v onto the target A, forming the bound state $B = A + v$.

The distorted wave Born approximation theory has been quite successful in describing transfer reactions. Let's consider a transfer reaction of the form $A(a,b)B$, where $a = b + v$ transfers v onto the target A, forming the bound state $B = A + v$, as shown in figure 2.1. The exact transfer matrix element can then be written either in the prior form for the entrance channel or the post form for the exit channel

$$\begin{aligned} \mathbf{T}^{exact}_{prior} &= \langle \Psi^{(-)exact} \mid V_{vA} + V_{bA} - U_i \mid \Phi_{I_b:I_a}(\mathbf{r}_{vb})\chi_i(\mathbf{R}_i)\rangle \text{ and} && (2.1) \\ \mathbf{T}^{exact}_{post} &= \langle \Phi_{I_A:I_B}(\mathbf{r}_{vA})\chi^{(-)}_f(\mathbf{R}_f) \mid V_{vb} + V_{bA} - U_f \mid \Psi^{exact}\rangle \, , && (2.2) \end{aligned}$$

where $\Psi^{(\pm)exact}$ are the exact solutions, $\Phi_{I_A:I_B}$ is the overlap function between A in spin state I_A and B in spin state I_B and $U_{i,f}$ are the optical potentials that generate the distorted wave functions $\chi_{i,f}$.

The DWBA theory replaces one of the exact solutions $\Psi^{(\pm)exact}$ of the three-body problem with a distorted wave multiplied with a corresponding bound state $\Psi^{(\pm)exact} = \Phi(\mathbf{r})\chi(\mathbf{R})$. Using $\mathcal{V} = V_{vA} + V_{bA} - U_i$ in the prior form and $\mathcal{V} = V_{vb} + V_{bA} - U_f$ in the post form one obtains the T matrix for the transfer process

$$\mathbf{T}^{DWBA}_{fi} = \langle \chi^{(-)}_f(\mathbf{R}_f)\Phi_{I_A:I_B}(\mathbf{r}_{vA}) \mid \mathcal{V} \mid \Phi_{I_b:I_a}(\mathbf{r}_{vb})\chi_i(\mathbf{R}_i)\rangle . \qquad (2.3)$$

V_{bA} is the core-core interaction between b and A, V_{vb} and V_{vA} are the binding potentials in the entrance and exit channels. U_i and U_f are the above-mentioned optical potentials of the incoming and outgoing channels.

The physical input needed is thus

(i) the optical potentials for the incoming and outgoing distorted waves, U_i and U_f,

(ii) the core-core interaction between b and A, V_{bA}, and

(iii) the overlap functions $\Phi_{I_A:I_B}(\mathbf{r}_{vA})$ and $\Phi_{I_b:I_a}(\mathbf{r}_{vb})$.

The overlap functions are described by single-particle states in a Woods-Saxon potential, with the depth of the potential fitted to reproduce the correct binding energy and the right Nlj quantum numbers.

Comparing the shape of the angular distributions obtained from DWBA calculations with the experimentally observed cross sections, one can determine the orbital angular momentum transfer to the singe-particle state populated in the reaction. The normalization between the DWBA calculation and the experiment yields the spectroscopic factors

$$\frac{d\sigma^{exp}}{d\Omega} = S^{exp} \frac{d\sigma^{DWBA}}{d\Omega} \tag{2.4}$$

which can be compared to structure calculations. The ability to extract these spectroscopic factors depends strongly on the energy of the beam used, which determines whether the reaction is peripheral, at the surface or more in the interior of the nucleus. The reaction is only then direct and can be described by the DWBA if it is at the surface of the nucleus. At large impact parameters (low energies and very forward scattering angles) the reaction can be completely peripheral and no longer sensitive to the interior of the nucleus and it is better to extract ANCs[1]. If on the other hand the energy is high (well above the Coulomb barrier) and the scattering angles are large so that the impact parameters are smaller than the radius of the nucleus, the DWBA is not expected to give reasonable results.

The optical potentials used in the DWBA have a real and an imaginary part, the latter taking into account all reactions that remove strength from the elastic scattering channel. The real part describes the attractive interaction between two nuclei and has typically a Woods-Saxon shape

$$V(r) = -\frac{V_r}{1 + \exp\frac{r-R_0}{a}} \tag{2.5}$$

with a depth V_r of around 50 MeV for protons and 100 MeV for deuterons, a radius $R_0 = (A_1^{1/3} + A_2^{1/3})r_0$ where r_0 is in the range of 1.2–1.5 fm and a diffuseness a of around 0.6 fm.

The imaginary part is the derivative of equation (2.5), typically with a radius of the order of r_0, the same diffuseness and a depth of 10–20 MeV.

DWBA calculations are very sensitive to the optical potentials used, with the spectroscopic factors obtained from different parametrizations varying by factors of 2–3 and also significantly different angular distributions. The parameters used for the optical potentials can either be derived from global parameter sets, which were fitted to a range of nuclei and energies or from elastic scattering data for the required channels at the appropriate energy.

Hence the experimental angular distributions obtained from the d(^{30}Mg, p)^{31}Mg reaction will be compared in chapter 5 to DWBA calculations obtained with different global parameter sets as well as optical parameters that were fitted to the elastic scattering data, measured in the same experiment. The code used in this thesis to perform the DWBA calculations is FRESCO [Tho06].

2.2 Transfer Reactions in Inverse Kinematics

Transfer reactions in inverse kinematics with radioactive ion beams suffer from the much lower beam intensity, in comparison to the normal kinematic transfer reactions, which use a light beam, e.g. deuterons, impinging on a thin target. Despite the great

---

[1] **A**symptotic **N**ormalization **C**oefficients

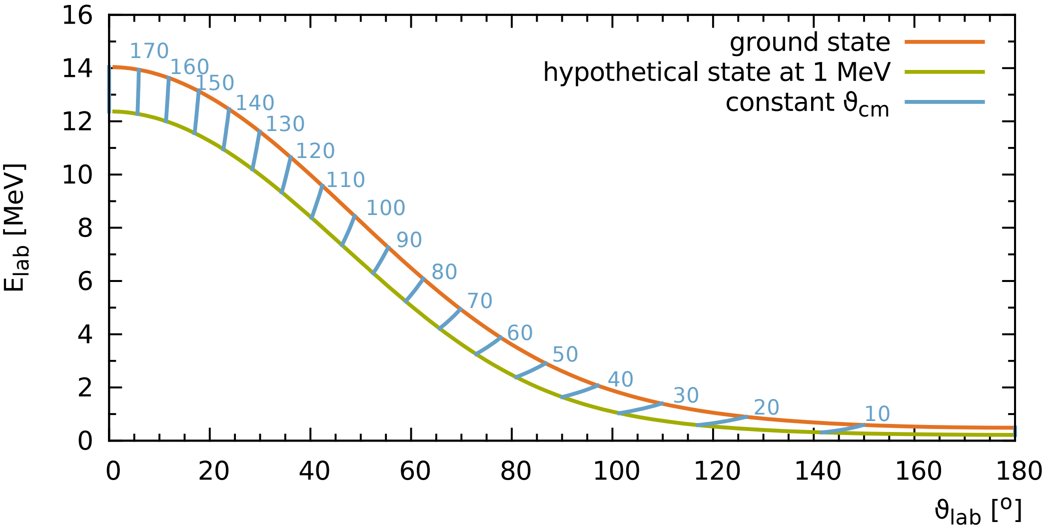

Figure 2.2: Kinematics of recoils from a (d, p) reaction in inverse kinematics at the example of d (^{30}Mg, p) ^{31}Mg.

technological advances achieved at radioactive beam facilities the beam intensities are still more than 6 orders of magnitudes lower than those achieved for stable beams. This requires the use of much thicker targets to compensate the lower beam intensities at least partly.

Thicker targets induce however a higher energy loss of the (relatively high Z) beam, which amounts to 10–30 % for the 1 mg cm^{-2} deuterated polyethylene targets, typically used at REX-ISOLDE. Due to the much higher mass of the beam particles, compared to the deuterons in the target, all beam-like ejectiles are emitted at very small angles (typically less than 5°) and can not be detected directly.

The protons emitted in a (d, p) reaction in inverse kinematics are emitted in backward direction for large impact parameters (0° scattering in the center of mass frame) and have a distinct energy-ϑ_{lab} relation, as shown in figure 2.2 for the d (^{30}Mg, p) ^{31}Mg reaction. Figure 2.2 also shows that the proton energies in backward direction are very small (but this depends on the Q-value of the reaction) and that a difference of 1 MeV in excitation energy between two states yields a much smaller energy difference for the protons emitted.

This, together with the energy loss in the target, which smears out the observed proton energies, limits the achievable resolution in excitation energy very much and makes it difficult to resolve close-lying states populated in a (d, p) transfer reaction by the energy of the protons alone. If one measures the γ-rays emitted by the ejectile in coincidence with the protons, one can however identify the populated excited states (if there is no feeding from higher lying states).

Another adverse effect of transfer reactions in inverse kinematics at facilities like ISOLDE is the lower beam energy, which limits the reliability of the extraction of spectroscopic factors from the data. It has however been shown that using *relative* spectroscopic factors, that is spectroscopic factors normalized e.g. to the spectroscopic factor of the ground state, one can reproduce the results from normal kinematics ($E_d = 14\,\text{MeV}$) transfer reactions in inverse kinematics ($E_d = 5.2\,\text{MeV}$) [Mah08].

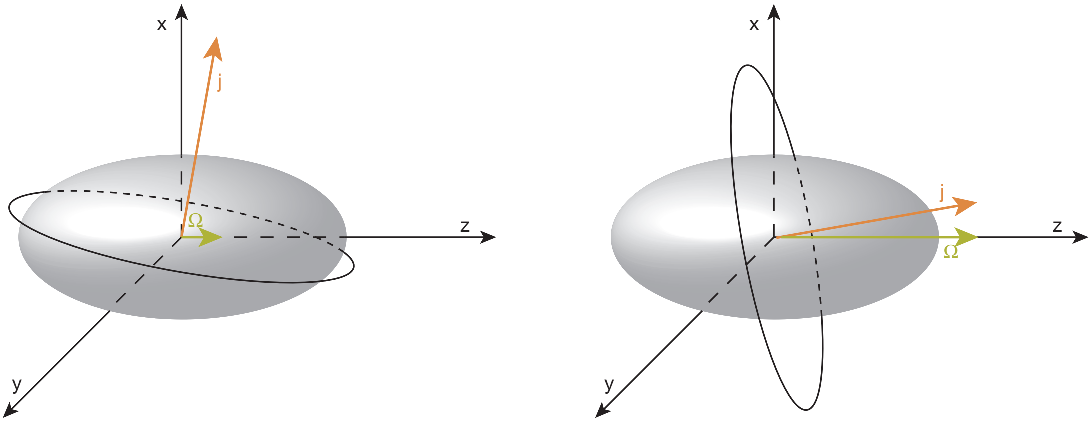

Figure 2.3: Illustration of single particle orbits with different Ω for a prolate nucleus. The left panel shows a single particle orbit with low Ω where the nucleons are on an equatorial orbit and close to the bulk on nuclear matter. The right panel shows a single particle orbit with high Ω which is further away from the bulk of nuclear matter.

2.3 The Nilsson Model

As discussed in chapter 1, one of the properties of the nuclei inside the Island of Inversion are their deformed ground states. A model that has been quite successful in the description of deformed nuclei is the Nilsson model [Nil55].

In the spherical shell model a wave function is described by the quantum numbers $[Nlj]$ where N is the principal quantum number, l the orbital angular momentum and $j = l + s$ the total angular momentum. Energy level with a total angular momentum j are $2j + 1$ degenerate due to the spherical symmetry. If the nucleus is not spherical, but e.g. prolate deformed, l and j are no longer good quantum numbers since orbitals with the same angular momentum can have different energies. This energy splitting is due to the fact that a nucleon that moves on an equatorial orbit around the prolate deformed nucleus is closer to the bulk matter of the nucleus so that its energy is lowered by the short-ranged attractive strong interaction. A nucleon whose total angular momentum is parallel to the symmetry axis of the nucleus on the other hand is further away from the bulk matter and has a higher energy (see also figure 2.3).

In the Nilsson model wave functions are described by the quantum numbers $\Omega^{\pi}[Nn_z\Lambda]$ where Ω (the projection of the single-particle angular momentum on the symmetry axis z) and π (the parity) are the only good quantum numbers, while N (the principal quantum number), n_z (the number of nodes of the wave function in direction of the z axis), and Λ (the projection of the orbital angular momentum on the z axis) are asymptotic quantum numbers, used to label the orbitals. Since the rotational angular momentum of axial symmetric nuclei doesn't contribute to the projection on the symmetry axis, the projection of the single-particle angular momentum on the symmetry axis (Ω) and the projection of the total angular momentum on the symmetry axis (K) are the same and are often used as synonyms.

Since the two orbitals with Ω and $-\Omega$ are equivalent, all energy level of the Nilsson model are two fold degenerate and each j orbital from the spherical shell model splits into $j + 1/2$ different Ω orbitals. The energy splitting between Ω orbits increases with Ω, i.e. the low Ω orbits have a smaller spacing than the high Ω orbits.

The deformed potential of the Nilsson model alters the energy eigenfunctions compared to the spherical shell model. The eigenfunctions of the Nilsson model are mixtures of states with the same Ω and π but different total (j) and orbital (l) angular momentum and can be written as

$$\psi_{Nils_i} = \sum_{N,j,l} C_j^i |Nlj\rangle \tag{2.6}$$

where $|Nlj\rangle$ are the wave functions of the spherical shell model and C_j^i are the configuration mixing coefficients.

The ψ_{Nils_i} are the wave functions in the body-fixed system (the non-rotating nucleus) where j is not a good quantum number. However the total angular momentum J must be a constant and its projection onto the symmetry axis K is a good quantum number. The Nilsson model wave function is an *intrinsic* state of a deformed nucleus, while the real nuclear states are combinations of this intrinsic motion with a rotational motion of the core.

The total angular momentum J is then a vector combination of the particle angular momentum j and the rotational angular momentum R of the core.

Transfer reactions such as (d,p) are direct reactions in which only a single nucleon is transferred into a given, empty valence orbital (ψ_{Nils_i}). In particular the process can not induce any rotational momentum into the system. The probability to populate a state with total angular momentum J is then proportional to the probability of the shell model wave function $|NlJ\rangle$ in the Nilsson wave function, which is ${C_j^i}^2$.

The quantity $(C_j^i P^i)^2$ is the same as the spectroscopic factors for spherical nuclei. ${P^i}^2$ is a pairing coefficient that represents the probability that the single nucleon orbit involved is either empty (for stripping reactions such as (d,p)) or full (for pick-up reactions like (d,t)), i.e. it is U^2 or V^2, respectively.

For further information see e.g. [Cas05].

Chapter 3

Experimental Setup

To get a complete picture of the experimental details, the following chapter gives a short summary of the ISOLDE facility and especially the REX-ISOLDE post-accelerator for radioactive ion beams. Before focusing on the details of the T-REX[1] silicon detector array, which was newly developed in the framework of this thesis, the MINIBALL spectrometer and its constraints for the overall design are discussed.

3.1 The ISOLDE Facility

For the production of short-lived radioactive secondary beams typically two significantly different methods are currently used.

- Projectile fragmentation or fission of fast beams or
- isotope separation on-line - the so called ISOL-technique.

In projectile fragmentation a heavy ion primary beam impinges on a target, producing a forward focused secondary beam consisting of a cocktail of isotopes. The isotopes are separated by a large acceptance magnetic spectrometer. This physical separation allows access to all elements produced, independent of their chemical properties (in contrast to the ISOL method). The typical energy of the secondary beam ranges from tens of $\mathrm{MeV\,u^{-1}}$ up to $1\,\mathrm{GeV\,u^{-1}}$ (e.g. GANIL, MSU, RIKEN or GSI) and allows an event-by-event particle identification.

The isotope separation method was originally used to produce a cocktail of isotopes in a thick target by an intense proton beam through spallation, fission, fusion, and fragmentation. The target was then moved to an ion source to extract the isotopes of interest (offline). The isotopes that could be produced were limited to those with lifetimes longer than the time it took for the radioactivity of the target to go down to a manageable level plus the time it took to move the target to the ion source.

The isotope separation method was improved by combining the target and the ion source so that the produced isotopes could be extracted on-line, thus creating the ISOL[2] method.

The ISOL method can produce beams with a very small emittance compared to the fragmentation method but the produced isotopes are limited to those with a lifetime of more than some ms due to the time it takes for the isotopes to diffuse out of the thick production target.

---

[1] **T**ransfer at **REX**

[2] **I**sotope **S**eparation **O**n-**L**ine

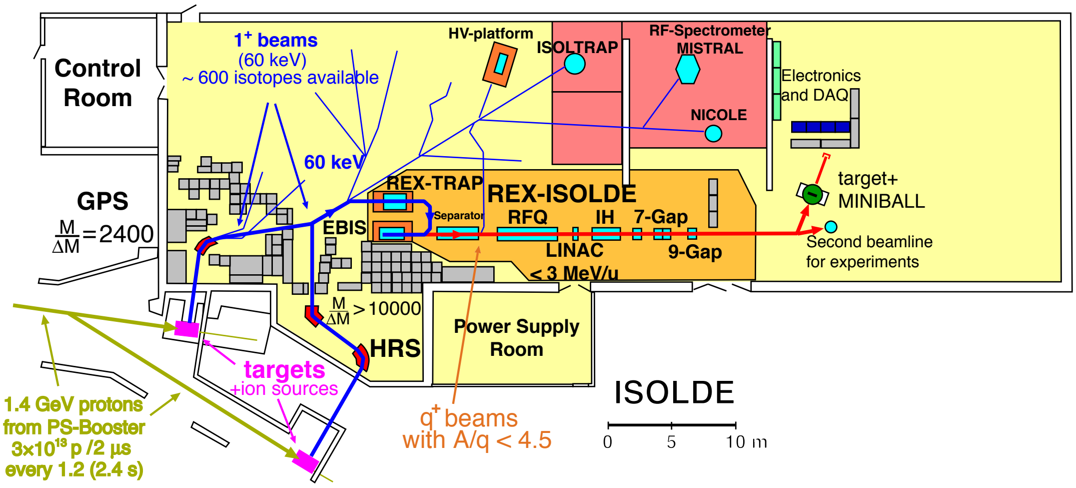

Figure 3.1: Overview of the ISOLDE experimental hall.

At the ISOLDE facility [Kug00] (see also figure 3.1) a beam of 1–1.4 GeV protons from the CERN PSB[3] is sent onto a thick, high temperature target which in the case of magnesium beams is made out of uranium carbide.The PSB consists of four synchrotron accelerator rings stacked on top of each other and provides bunches of up to 3×10^{13} protons every 1.2 seconds. The proton pulses and their distribution to the different experiments (e.g. ISOLDE, nTOF, CNGS etc.) is organized in so called super cycles of 12 to 48 proton bunches. The available proton current that can be delivered to ISOLDE is currently limited by radiation protection aspects to 2 μA.

After their production the radioactive isotopes thermally diffuse out of the target through a transfer line to the ion source where they are ionized. There are different ion sources available with different efficiencies and selectivities so that they can be selected based on the element (and sometimes isotope) of interest and the requirements on beam purity. In the case of magnesium beams the RILIS[4] [Fed00] is used. The RILIS uses two to three different lasers. The wavelengths are adjusted to transitions in the atomic shells of the isotope of interest thus first exciting and then selectively ionizing only this isotope. The probability of photo-ionization per laser pulse can reach some 10 %.

The 1^+ ions are extracted, accelerated to 30–60 keV, and sent through either the GPS[5] or the HRS[6] to get isobaric pure beams (with small contaminations from higher charge states) which are then distributed to the different experiments in the ISOLDE hall. For the present experiment the GPS separator was used since it is better suited for the RILIS and the increased mass resolution of the HRS doesn't offer any advantage.

---

[3] **P**roton **S**ynchroton **B**ooster

[4] **R**esonant **I**onisation **L**aser **I**on **S**ource

[5] **G**eneral **P**urpose **S**eparator

[6] **H**igh **R**esolution **S**eparator

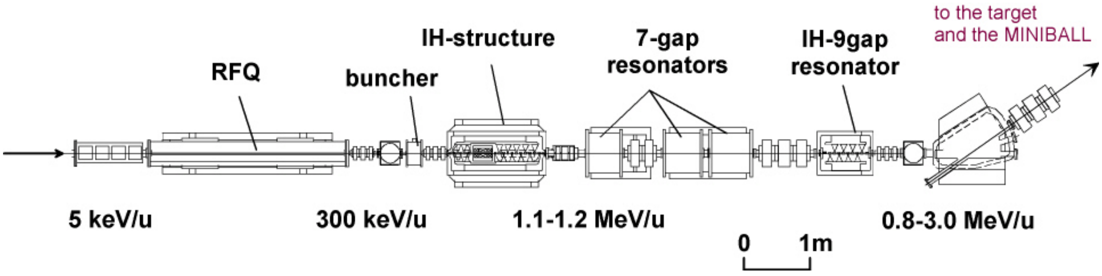

Figure 3.2: Schematics of the REX linear accelerator at ISOLDE (from [ISO]).

3.2 The REX-ISOLDE Post-Accelerator

The REX[7] accelerator [Hab00, Kes03, Ced04] at ISOLDE was built to demonstrate a new way of post-accelerating radioactive ion beams. The ions are first accumulated, trapped, and cooled in a Penning trap (REX-TRAP), then transferred to the REX-EBIS[8] to charge breed them to a higher charge state before they are accelerated in a short linear accelerator (REX-LINAC) to energies of up to 3 MeV u^{-1}. Figure 3.2 shows a schematic view of the setup.

The 30–60 keV 1^+ ions delivered by ISOLDE are slowed down to $\approx$ 50 eV by the HV potential of the REX-TRAP which allows a continuous injection of beam into the trap. An argon or neon buffer gas inside the trap (at typically 10^{-3} mbar) finally stops the ions which are additionally cooled by sideband cooling techniques [Ame05]. After the accumulation and cooling (for magnesium isotopes typically 20 ms) the ions get extracted in short bunches, re-accelerated to 30–60 keV, and injected into the REX-EBIS. The transmission of the REX-TRAP depends on the beam intensities: for less than 10^5 ions per bunch it can be as high as 45 % whereas it decreases to 10 % for 10^7 ions per bunch due to space charge effects.

The REX-EBIS uses an intense mono-energetic electron beam of 5 keV to produce ions of higher charge states from singly charged ions transferred from the REX-TRAP. In the REX-EBIS electron current densities of 150 A cm^{-2} can be reached by the compression of the electron beam with a 2 T magnetic field created by a superconducting solenoid.

The breeding time can be varied between 5 and 19 ms if the REX-EBIS is operated at 50 Hz to match the 20 ms trapping time of the REX-TRAP. Since the duration of the breeding determines the charge state distribution of the produced ions it can be optimized for a certain A/q value. The ion bunches extracted from the REX-EBIS have a typical length of 50 μs. Using the so called slow extraction this time can be stretched up to 300 μs. Only one charge state is selected by the subsequent A/q separator and accelerated in REX.

The s-shaped separator also reduces the background of stable residual ions from the rest-gas in the REX-EBIS with a mass resolution of $(A/q)/\Delta(A/q) \approx 100 - 150$ and a transmission of 75–90 %. After the separator the ions are injected into the REX-LINAC.

The REX-LINAC consists currently of four different types of resonant structures. The ions extracted from the REX-EBIS have an energy of 5 keV u^{-1} and are first

---

[7] **R**adioactive beam **EX**periment

[8] REX-**E**lectron **B**eam **I**on **S**ource

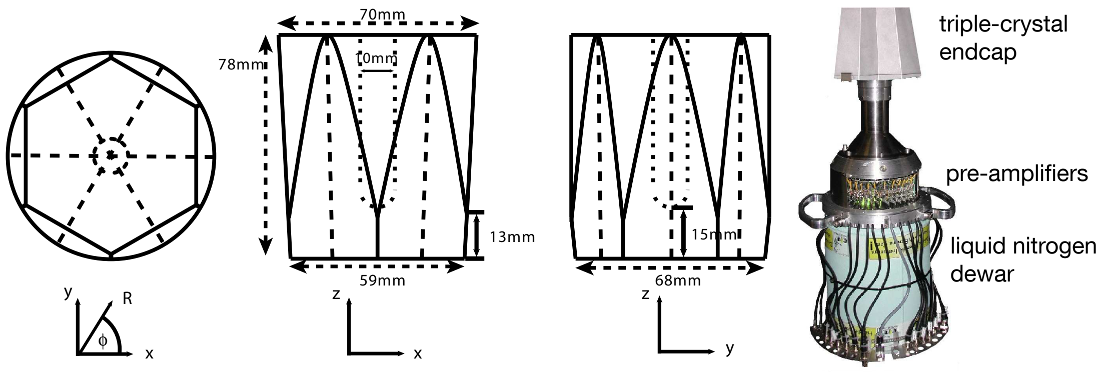

Figure 3.3: Schematic drawing of a MINIBALL germanium crystal from [Gun00] and a picture of a MINIBALL cluster on the right.

accelerated to intermediate energies of 1.2 MeV u^{-1} by the RFQ[9] and the IH[10] structure.

The following 7-gap resonators are operated at 101.28 MHz (half the frequency of the CERN proton LINAC) and a duty cycle of 10 %. These resonators accelerate the ions to energies of 2.25 MeV u^{-1}. The last resonator, which accelerates the ions to their final energy of up to 3 MeV u^{-1} is a 9-gap resonator and was installed in 2004.

The total transmission of the REX-LINAC is in the order of 80 % putting the overall efficiency of REX-ISOLDE at $\approx$ 5–10 %. This means about every tenth ion of the wanted isotope extracted from the ISOLDE-target is successfully stopped, charge bred and then re-accelerated. The energy spread of the REX beam is about 1–2 %.

A bending magnet at the end of REX is used to deliver the beam to either the 0°, 20° or 65° beam lines.

In combination with the time-dependence of the production of radioactive isotopes at ISOLDE the time structure of the beam can be quite complicated. The radioactive isotopes are produced by the proton beam every 1.2 s (or multiples thereof) and then released from the target following a release curve whose declining slope is determined by the half-life of the isotopes and their chemical properties (as shown in figure 5.9).

Due to the accumulation of the beam in the REX-TRAP, all ions released during the 20 ms trapping time are emitted in the 100–300 μs long EBIS pulse resulting in much higher instantaneous beam intensities. Also more than 95 % of the ^{30}Mg is released from the source within the first 600 ms after the proton pulse. This gives a instantaneous rate that is a factor $100 - 300$ higher than the average beam intensity in this experiment.

3.3 The MINIBALL Spectrometer

The MINIBALL spectrometer [Ebe01] is installed at the 65° beam line after the bending magnet.

The MINIBALL array consists of eight triple clusters, that contain three sixfold segmented HPGe[11] detectors each. The detectors are individually encapsulated

---

[9] **r**adio **f**requency **q**uadrupole

[10] **i**nterdigital **h**-type

[11] **H**igh **P**urity **Ge**rmanium

and segmented by subdividing the outer contact as shown by the dashed line in figure 3.3. Identifying the first interaction point of a γ-ray in a certain segment of the crystal allows a more precise determination of the direction the γ-ray was emitted. This allows a better Doppler correction which is necessary for reactions in inverse kinematics where the emitting particle has a velocity of $\approx$ 5–8 % of the speed of light (see also chapter 4).

The arrangement of three crystals into one cluster allows to increase the photopeak efficiency by adding the coincident detected energies of all crystals of one cluster together (addback) to get the full energy of γ rays that deposited energy in more than one crystal, e.g. by Compton scattering from one crystal into another one.

The eight MINIBALL clusters are positioned as close as possible to the reaction target to increase the covered solid angle, see also figure 3.12 and figure 3.13. The forward clusters are positioned at polar angles of about 70° and the backward clusters at about 135°.

3.4 T-REX

T-REX is a new arrangement of different silicon detectors, optimized for the reaction kinematics of transfer reactions in inverse kinematics. In the framework of this thesis the design and layout was developed in 2006/7. The first setup, including nearly all essential detectors and electronics, was tested with stable magnesium beam at the MLL tandem laboratory in 2007. It was constantly improved between each years experiments so that the setups of 2007 (first d(^{30}Mg, p)^{31}Mg experiment), 2008 (t(^{30}Mg, p)^{32}Mg and second d(^{30}Mg, p)^{31}Mg experiments), 2009 (^{11}Be transfer and d(^{66}Ni, p)^{67}Ni experiments), and 2010 (^{11}Be transfer, t(^{44}Ar, p)^{46}Ar, and d(^{78}Zn, p)^{79}Zn experiments) differ in some details. In the following the original setup of 2007 and the modifications made for the 2008 experiments are presented. The changes made for the 2009 and 2010 setups are discussed in appendix E.

3.4.1 Detector Setup

In order to measure the angular distribution of the protons emitted from (d,p) transfer reactions in inverse kinematics a large solid angle has to be covered both to get an as complete picture of the angular distribution as possible and to have a high efficiency of detecting the products of the weak radioactive ion beams. At the same time a sufficient granularity and position resolution of the detectors is essential in order to measure the shape of the angular distributions. To achieve this, different new setups of silicon barrels were considered, each consisting of so called CD detectors as end-caps in forward and backward direction and a barrel of silicon detectors around 90° (see appendix C).

In addition a particle identification based on the ΔE - E$_{\mathrm{Rest}}$ technique is required to distinguish the protons from transfer reactions from elastically scattered deuterons and tritons from (d,t) reactions. This is achieved by using position sensitive strip detectors as 140 μm thick ΔE detectors from Micron Semiconductors [Mic], while 1000 μm thick un-segmented pad detectors from Canberra [Can], mounted 1.7 mm behind the ΔE detectors, are used to determine the E$_{\mathrm{Rest}}$ energy. 140 μm ΔE detectors allow an identification of protons with energies as low as about 4 MeV [Ern84], while the energy loss of higher energetic protons is at about 1 MeV still well separated from the noise.

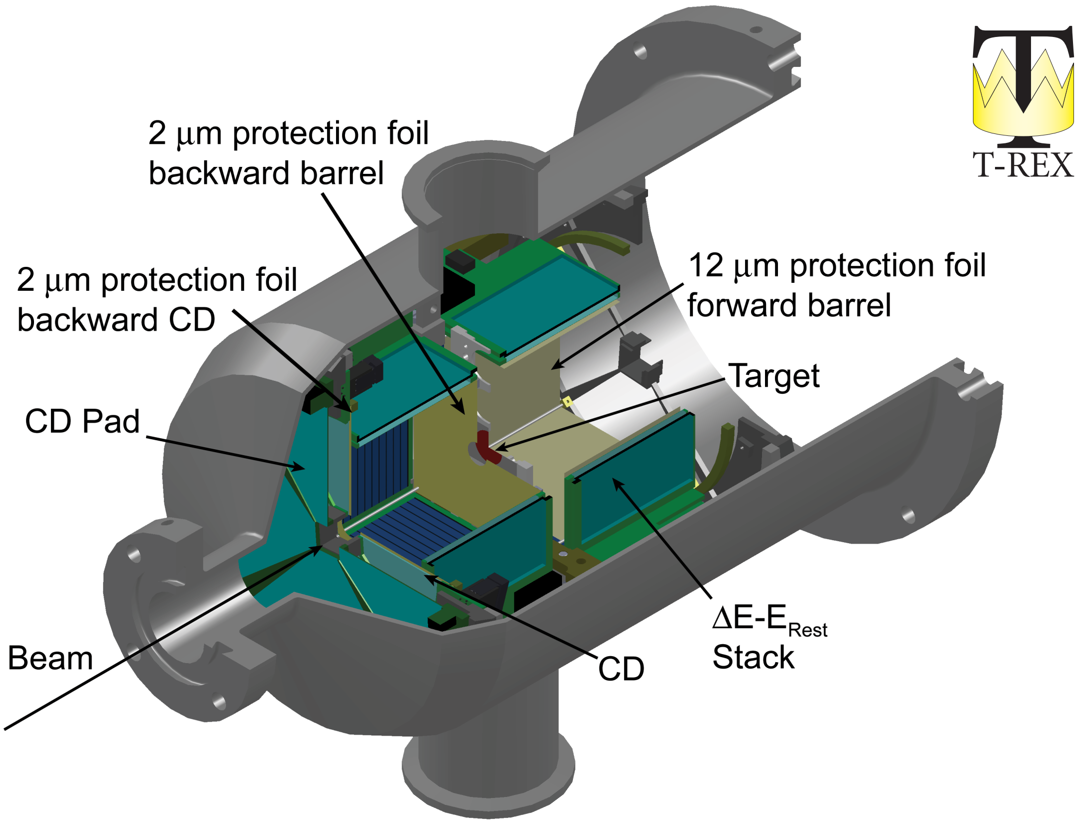

Figure 3.4: Technical drawing of the silicon barrel inside the vacuum chamber as it was used in 2008.

Since most beams used at REX-ISOLDE are heavier than any of the constituents of deuterated polyethylene (protons, deuterons, and carbon), any elastically scattered particles are emitted only in forward direction. Due to the reaction kinematics the same holds true for any tritons from a possible (d,t) reaction. Thus it was deemed sufficient to use ΔE - E$_{\mathrm{Rest}}$ telescopes only in forward direction to identify the protons, deuterons, and tritons, while in backward direction where only protons from the (d,p) transfer reaction are emitted such particle identification was not thought necessary.

However, during the first T-REX experiment with a radioactive ^{30}Mg beam at REX-ISOLDE in 2007 it was recognized that it is necessary to have ΔE - E$_{\mathrm{Rest}}$ telescopes in backward direction as well in order to be able to suppress the background of electrons from β-decays of radioactive beam particles that were stopped in the target chamber. In order to be able to use the same ΔE - E$_{\mathrm{Rest}}$ telescopes in forward and backward direction the chamber was thus re-designed after the first beam time in 2007 and since 2008 all transfer experiments are done with a barrel consisting of eight ΔE - E$_{\mathrm{Rest}}$ telescopes.

The setup of particle detectors as it was used from 2008 on is shown in figure 3.4. The beam impinges on a deuterated polyethylene target of 0.1–1 mg cm^{-2} thickness, which is mounted in one of four positions on the target ladder. Particles scattered in backward direction are detected by a ΔE - E$_{\mathrm{Rest}}$ stack of either CD detectors or Barrel detectors while only Barrel detector ΔE - E$_{\mathrm{Rest}}$ stacks are placed in forward direction at this stage.

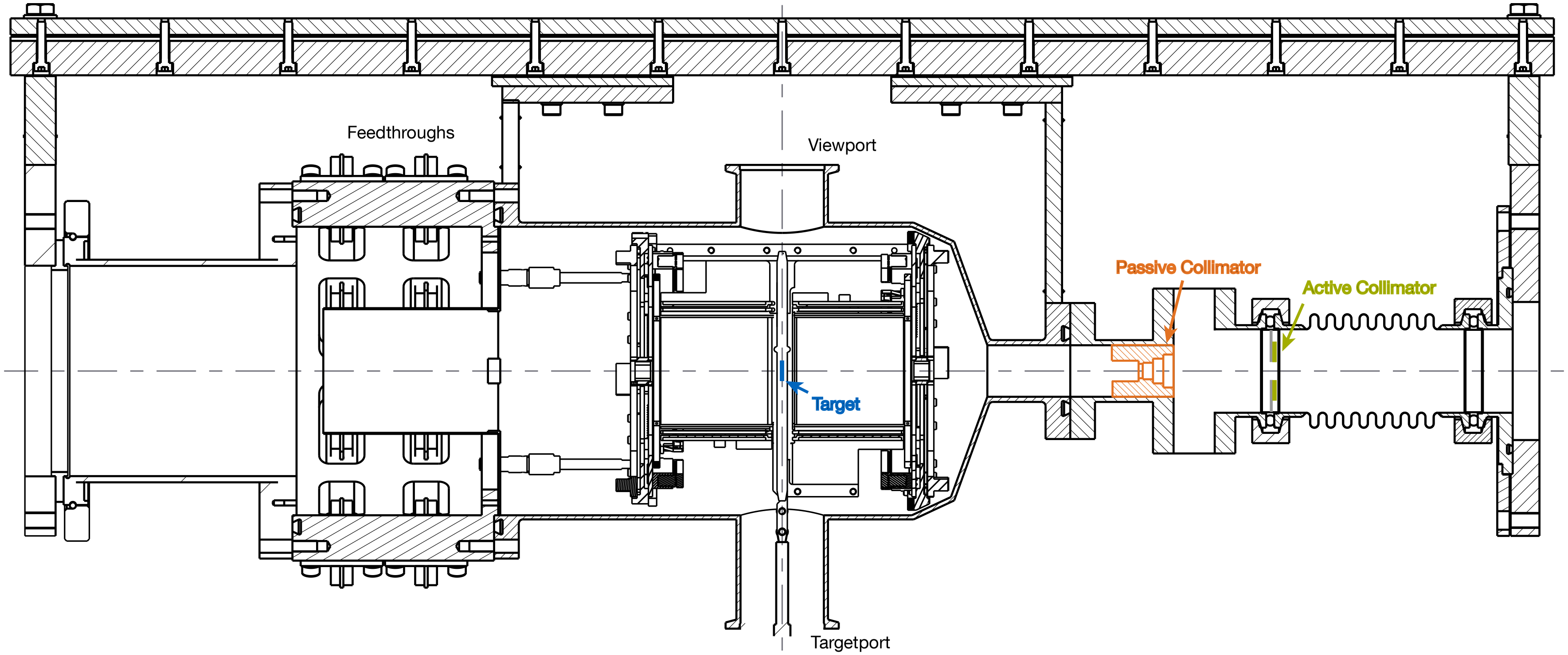

Figure 3.5: Drawing of the T-REX beam line with the beam coming from the right. The active collimator is indicated in green, the passive tantalum collimator in orange. The target position is marked blue.

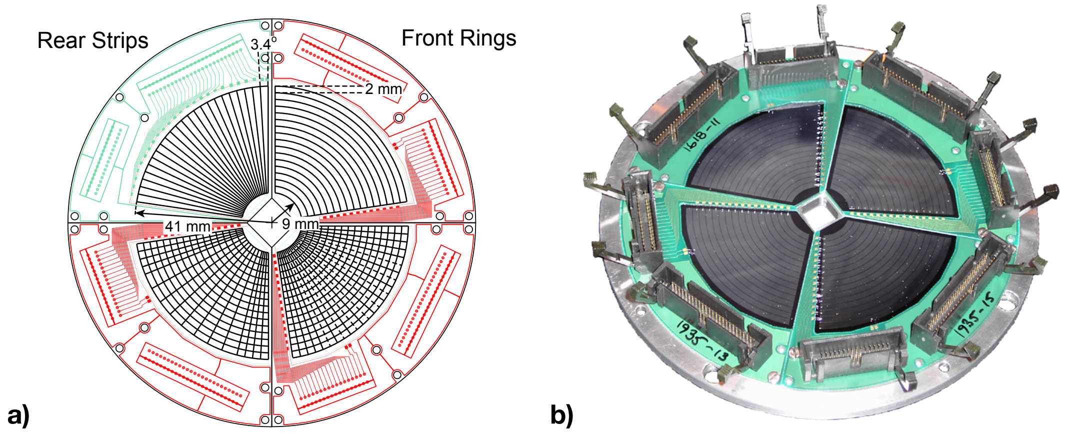

Figure 3.6: a) Drawing of a CD detector. On the top are the back and front of a quadrant (left and right, respectively). The lower part shows the electrical and physical segmentation of the detectors (left and right, respectively). The dashed lines indicate pairs of strips that are connected to reduce the number of signals from the rear to 16. b) Photo of a CD Detector.

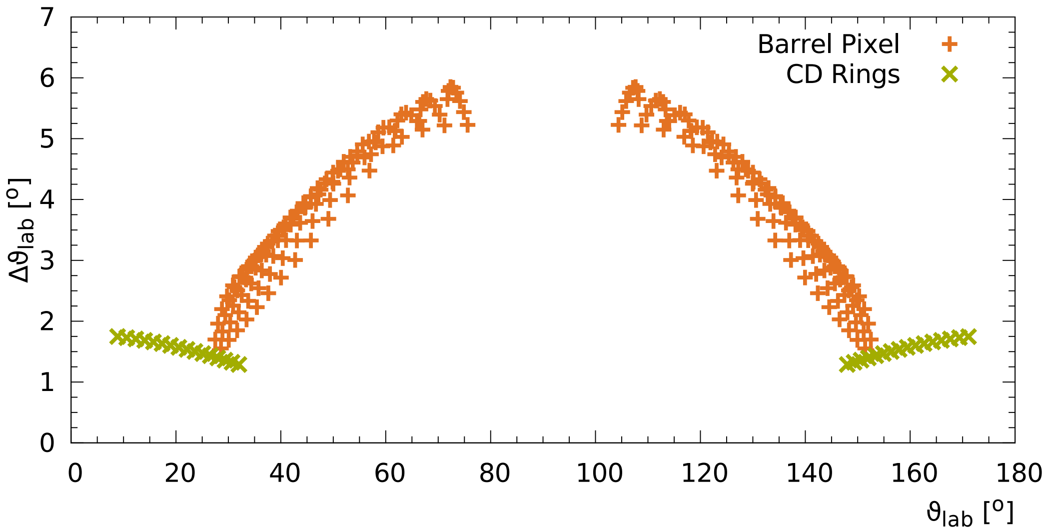

Figure 3.7: ϑ resolution of CD and barrel detectors. Rings of 2 mm width at 64 mm distance for CD detectors and $3.125 \times 3.125\,\mathrm{mm}^2$ pixel for barrel detectors.

CD Detectors

The CD detectors [Ost02] consist each of four quadrants of DSSSD[12] (Design QQQ2 from Micron Semiconductors [Mic]) with annular segmentation on the front and radial segmentation on the back (see figure 3.6a) as ΔE detectors and unsegmented pad detectors (Design QQQ1 from Micron Semiconductors) as E_{Rest} detectors. The detectors are the already existing ones from the Coulex-Setup for MINIBALL and can be placed either in backward or forward direction (the latter option was used e.g. in the ^{11}Be transfer experiment IS430).

---

[12] **D**ouble **S**ided **S**ilicon **S**trip **D**etectors

The active area of the segmented CD detectors has an inner radius of 9 mm and an outer radius of 41 mm while the outer radius of the pad detectors is 50 mm. The width of the 16 annular rings is 1.9 mm at a 2 mm pitch and each of the 24 radial strips covers a φ range of 3.4°. To reduce the number of electronic channels needed (and because transfer reactions don't need a high azimuthal resolution) the number of radial strips was reduced from 24 to 16 by connecting the inner 16 strips by pairs as shown in the lower half of figure 3.6a.

Due to the large distance of the CD detectors from the target ($d_{CD} = 64$ mm) the polar resolution of these detectors is $1.3° < \vartheta_{\text{lab}} < 1.7°$ (see figure 3.7). Each detector quadrant covers an azimuthal range of $\Delta\varphi = 81.6°$, leading to a solid angle coverage of $\Delta\Omega \approx 15\,\%\pi$ per quadrant. The covered polar range depends somewhat on the azimuthal angle since the CD detectors are partially covered (and overlapped) by the barrel detectors. The polar overlap is between $150° < \vartheta_{\text{lab}} < 160°$ and the maximum scattering angle covered by the backward CD detectors is $\vartheta_{\text{lab}} < 172°$.

The thickness of the segmented CD detector and the unsegmented pad detector behind it is 500 µm each. This is not an optimal solution for the backward direction since the energy of protons emitted under such backward angles is typically quite low ($E \lesssim 5$ MeV) and they are thus stopped in $d \lesssim 215\,\mu\text{m}$ of silicon. Also, to get an efficient identification of electrons it is better to have a very thin ΔE detector to minimize the probability that electrons are stopped in this detector. Hence it is planned to use a new CD detector with just 140 µm thickness in backward direction while the existing 500 µm detectors will be used in forward direction. New 1000 µm or 1500 µm pad detectors will be used as E_{Rest} detectors in forward direction to increase the range of protons that can be identified without punching through the ΔE - E_{Rest} stacks.

The dead-layer of the CD detectors (both segmented and unsegmented) is given as 0.4–0.5 µm due to implantation and 0.2–0.3 µm aluminum metalization in addition [Dav02].

Barrel Detectors

In order to keep the number of electronic channels small, position sensitive strip detectors with resistive strips are used for the barrel. The detectors that were chosen for the barrel part of T-REX have an active area of $50 \times 50\,\text{mm}^2$ segmented into 16 position sensitive strips (Design X1 from Micron Semiconductors with custom PCB[13], see also figure 3.8a). After considering different configurations for the silicon barrel (see appendix C) a configuration was chosen with four detectors arranged in a box shape in forward as well as in backward direction. This configuration gives the best compromise between a large range of covered polar angles, high efficiency, small size of the setup, good position resolution, and ease of access to the detectors.

To cover a maximum range of polar angles it was necessary to use a PCB design, which is only slightly larger than the detector, especially in beam direction. This led to the decision to arrange the barrel detectors with their strips perpendicular to the beam direction and to read out only one end of the resistive strips while the other ends of all strips are connected and read out together. This way only one signal had to be directed around the detector making it possible to have a only 2 mm wide PCB on two sides of the detector and no PCB on the third side while the connectors are all on the remaining fourth side.

---

[13] **P**rinted **C**ircuit **B**oard

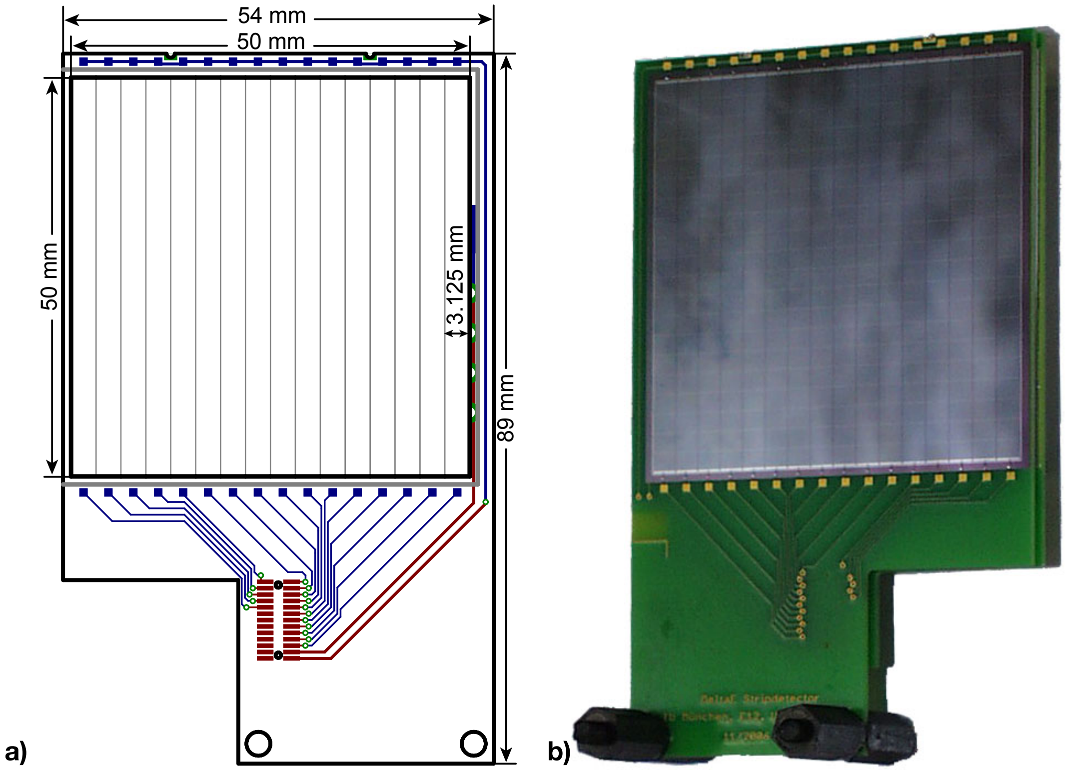

Figure 3.8: a) Schematic drawing of a barrel strip detector. The signals are routed via the connector on the bottom to the pad E_{Rest} detector. The cable is connected to a SMC connector on the E_{Rest} detector. b) Photo of a barrel detector stack. The strips run vertical while the horizontal structure stems from the technique of creating a resistive layer on the front of the detector.

Due to this the gap between the forward and backward detectors, that is necessary to allow the passing of the target ladder, could be reduced to 10 mm between the PCBs, which leads to a gap of 16 mm between the active areas of the detectors. This is necessary because for many transfer reactions the angular distributions can be quite distinctive around $\vartheta_{\text{lab}} = 90°$. Plans to further reduce this gap and thus expand the covered ϑ_{lab} range towards 90° are discussed in appendix E.

The negative detector bias is applied to the p-side strips of the detector. In order to avoid noise from the bias it is filtered by a 10 nF coupling capacitor on the side where all strips are connected together.

The distance of the barrel detectors to the beam axis was chosen to be 29 mm. Since the size of the detector is $52 \times 52\,\text{mm}^2$ and the PCB adds another 2 mm this leaves a space of 1 mm between the detectors and results in the same φ range being covered by the barrel as by the CD detectors.

The entrance/exit window of the barrel strip detectors is about $0.2\,\mu\text{m}$ and the pad detectors have windows of < 50 nm and $< 5\,\mu\text{m}$ on the junction (front) and ohmic (rear) side, respectively.

Foils

To protect the silicon detectors from high rates of elastically scattered particles there are four different places in the setup to put foils in front of them. Starting from the most forward angles, a foil can be placed a few millimeters in front of a possible forward CD detector to stop any elastically scattered beam from reaching the detectors (thickness $\approx 50\,\mu$m of Mylar™[14]).

The maximum elastic scattering angle of ^{30}Mg on ^{12}C (the heaviest constituent of a polyethylene target) is $\vartheta_{\text{lab}} \lesssim 25°$ i.e. elastically scattered beam is no problem for the barrel detectors but recoiling ^{12}C or deuterons emitted close to $\vartheta_{\text{cm}} = 0°$ are detected around $\vartheta_{\text{lab}} = 90°$ and could thus pose a rate- and/or dead-time problem. To reduce the number of elastically scattered recoils hitting the barrel detectors a typically $12\,\mu$m thick Mylar™foil can be mounted 2 mm in front of the barrel detectors. Such a foil stops elastically scattered carbon and deuterons and prevents them from hitting the strip of the barrel detectors closest to $\vartheta_{\text{lab}} = 90°$ which corresponds to a $\vartheta_{\text{cm}} \approx 15$–$30°$. This way $\approx$ 80 % of all carbons and deuterons, which would hit the barrel detectors, are stopped. It also limits the ϑ_{cm} range, in which the elastically scattered deuterons can be used to determine the optical potential, to $45° \lesssim \vartheta_{\text{cm}} \lesssim 125°$ since the energy of the deuterons between $30° \lesssim \vartheta_{\text{cm}} \lesssim 45°$ is too small to generate a trigger signal.

If the beam used is lighter than the heaviest target constituent, which is likely the case if a tritium loaded titanium foil is used as target for (t,p) experiments, back-scattering of the beam is possible. Since it is not possible to distinguish these back-scattered beam particles from the low-energy protons emitted in backward angles with a silicon ΔE - $\mathrm{E_{Rest}}$ stack it is necessary to instead stop the back-scattered beam in a thin (typically $2\,\mu$m) Mylar™foil of which two can be placed in backward directions (see figure 3.10). One is placed a few millimeters in front of the target (with a hole in the middle to allow the beam to pass through) and protects mostly the backward barrel detectors. The second foil is placed directly in front of the backward CD detector in the same way as the thicker foil used to stop elastically scattered beam particles from reaching the forward CD detector.

Beam Diagnostics

In order to improve the diagnostics of the beam position and focus, two new detectors were included in the T-REX setup.

A PCB with four PiN diodes ($10 \times 10\,\text{mm}^2$) around a 10 mm hole is placed as an active collimator in front of a tantalum collimator. This assembly is about 180 mm and 240 mm upstream of the target, see also figure 3.5. This allows monitoring the position of the beam at its entrance of the vacuum chamber during beam tuning and during the experiment since there is always a small halo of beam particles around the main beam.

A $10\,\mu$m thick poly-crystalline CVD[15] diamond detector which is segmented into 9 pixels (figure 3.9) can be mounted on the lowest position of the target ladder and used to ensure that the beam is centered and focused at the target position. Being made of diamond, the detector withstands the beam intensities of REX-ISOLDE without sustaining any damage and its thickness prevents any beam from being stopped (which would create a large background from β decays).

---

[14] bi-axially-oriented polyethylene terephthalate

[15] **c**hemical **v**apour **d**eposition

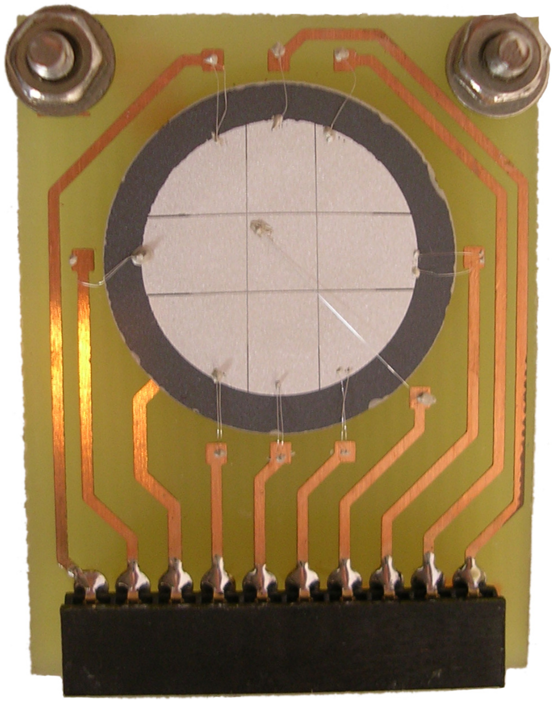

Figure 3.9: Photo of the 10 μm thick segmented polycrystalline diamond beam detector with aluminum metalization. The central pixel has a size of $3 \times 3\,\text{mm}^2$.

3.4.2 Mechanical Setup

In order to be able to switch between the ‘‘old’’ Setup and the T-REX setup without too many modifications the length of T-REX and the two end-plates (upstream and downstream) were chosen to be the same as the ones used before.

Vacuum Chamber

The vacuum chamber has to fulfill six major design criteria:

(i) it must be possible to reach a 1×10^{-7} mbar vacuum in the beamline,

(ii) the walls have to be thin to reduce the absorption of γ-rays,

(iii) it must allow a close geometry of the MINIBALL cluster for high γ-ray detection efficiency,

(iv) it should provide an electrical shielding of the detectors and cables,

(v) because of the complicated detector array with 276 channels easy access to the detectors is required and

(vi) easy replacement of the target ladder should be possible.

The chamber is mounted on a rail that runs 13 cm above the beam axis connecting the two end-plates, see figure 3.5. This allows easy access to the detectors by removing the bellow and collimator that form the beam-line between the upstream end-plate and the target chamber which creates enough space to slide the vacuum chamber so far upstream that all detectors can be accessed. If this limited access is not enough or if a detector has to be replaced the whole assembly of silicon detectors can be easily dismounted by unscrewing the whole silicon barrel from the four bolts that attach it to the downstream flange (see figure 3.11).

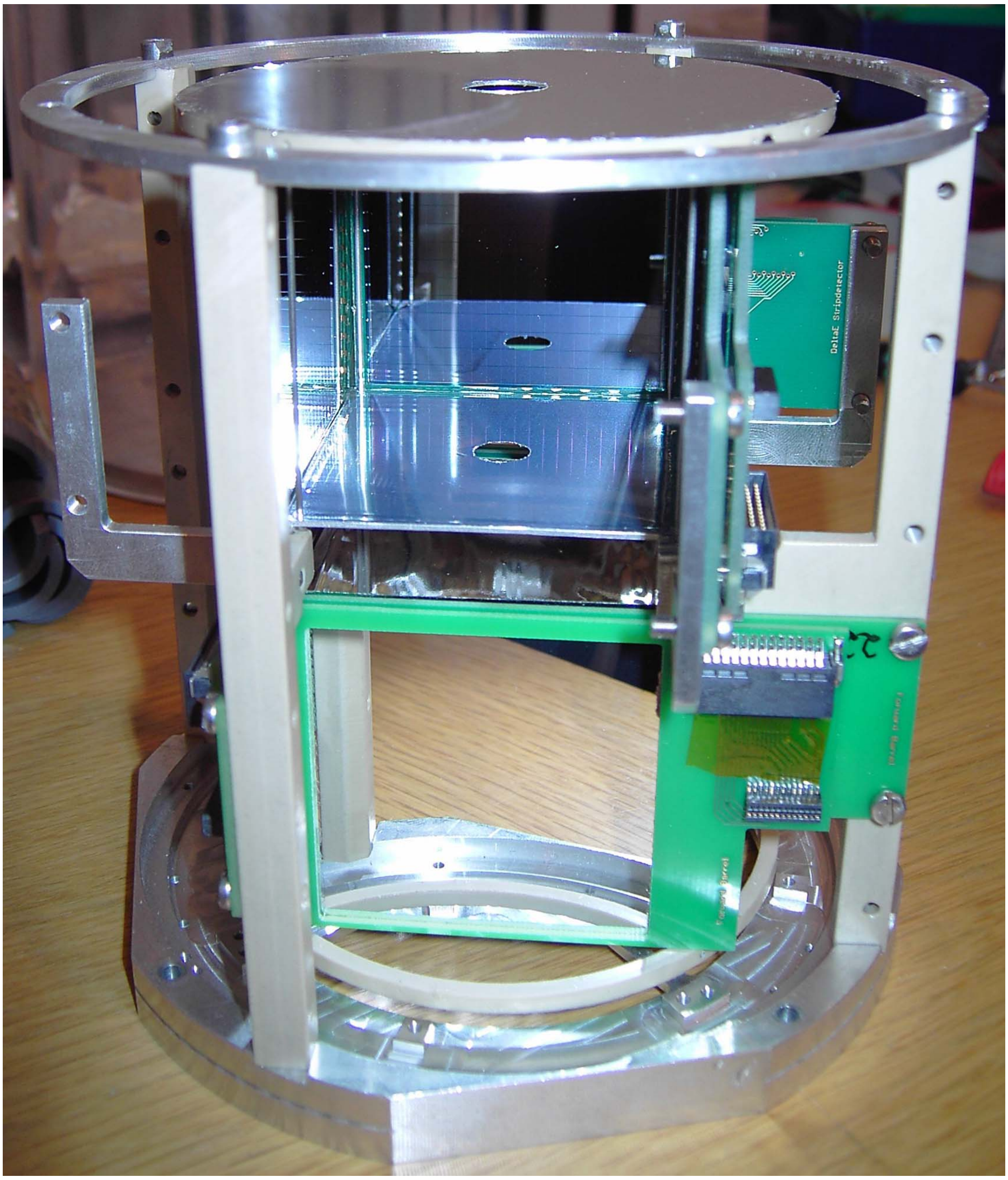

Figure 3.10: Photo of the barrel with one backward detector stack and backward CD removed (top). In the center and on the top a 2 μm aluminized Mylar™foil is mounted that protects the backward barrel and the backward CD from back-scattered beam particles. In the middle the 10 mm gap necessary to slide the target ladder in and out can be seen.

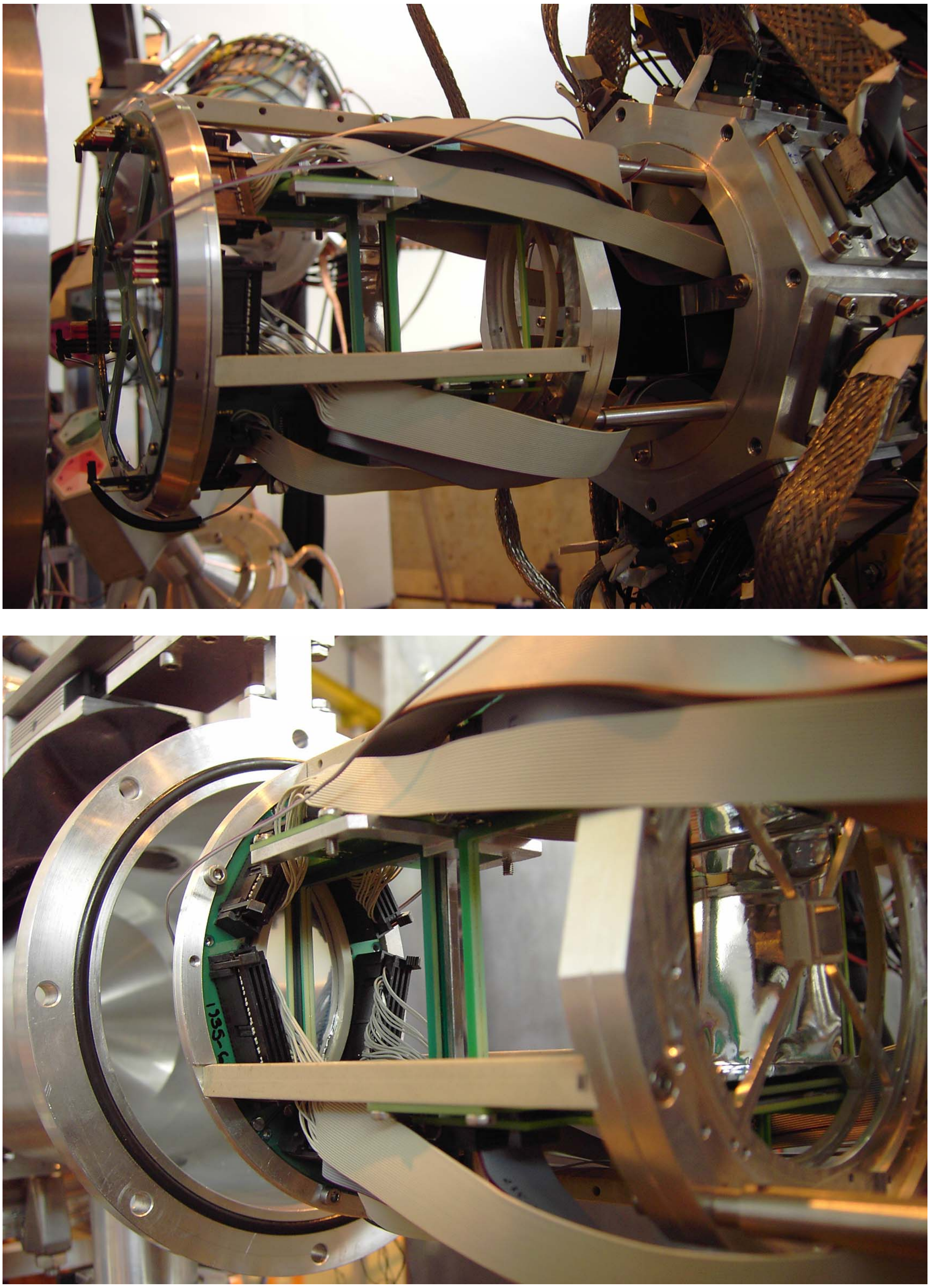

Figure 3.11: Photos of the fully equipped detector barrel mounted at its final position in the beamline (beam entering from the left). Top: On the right side the flange with the 16 feedthroughs to which the silicon barrel is attached. Bottom: looking upstream, on the left the connectors of one quadrant of the CD and on the right the view through the empty forward CD holder into the forward barrel with the 12 µm Mylar™foil.

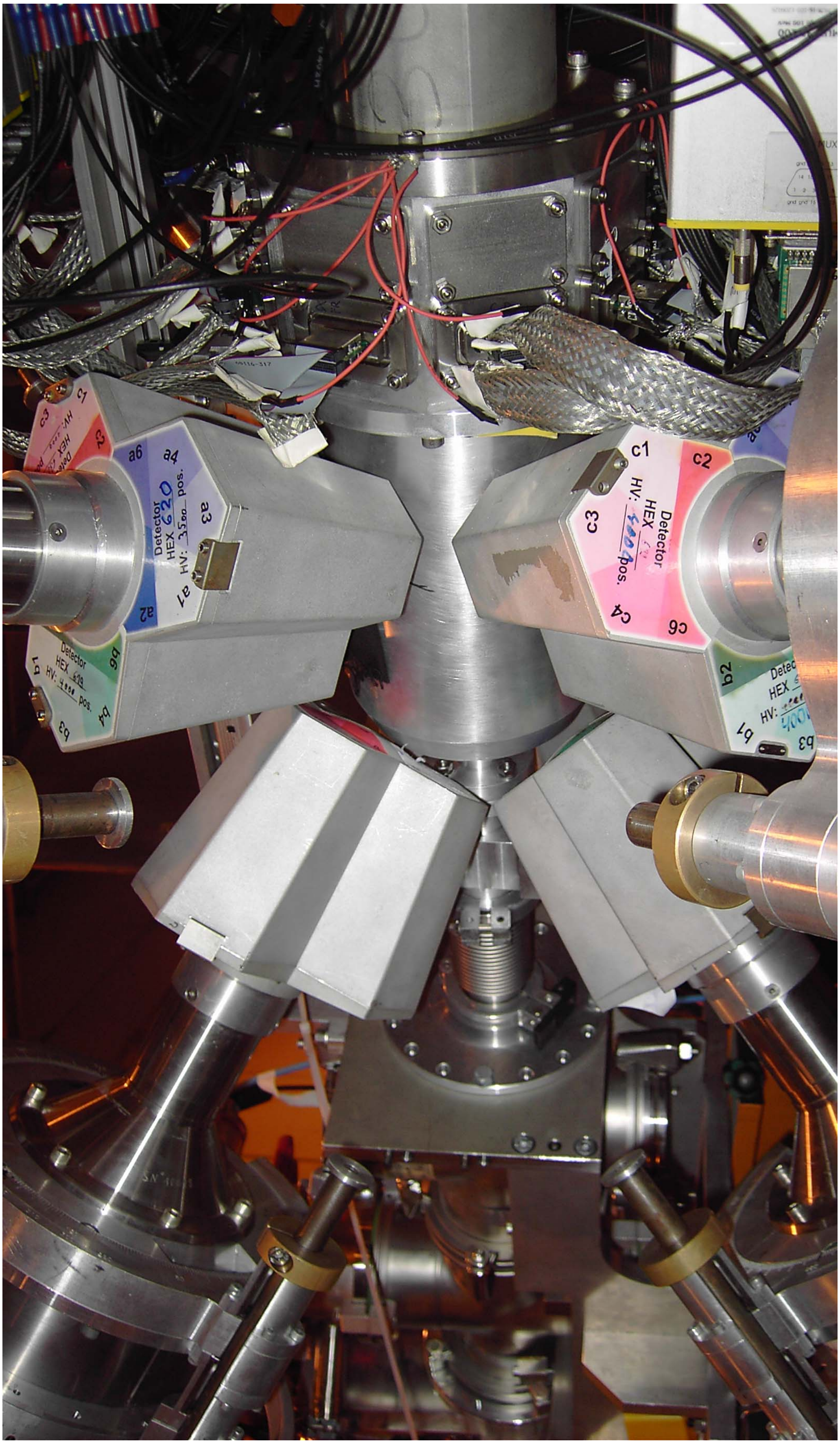

Figure 3.12: The closed vacuum chamber, surrounded by the MINIBALL detectors. Beam enters from the left.

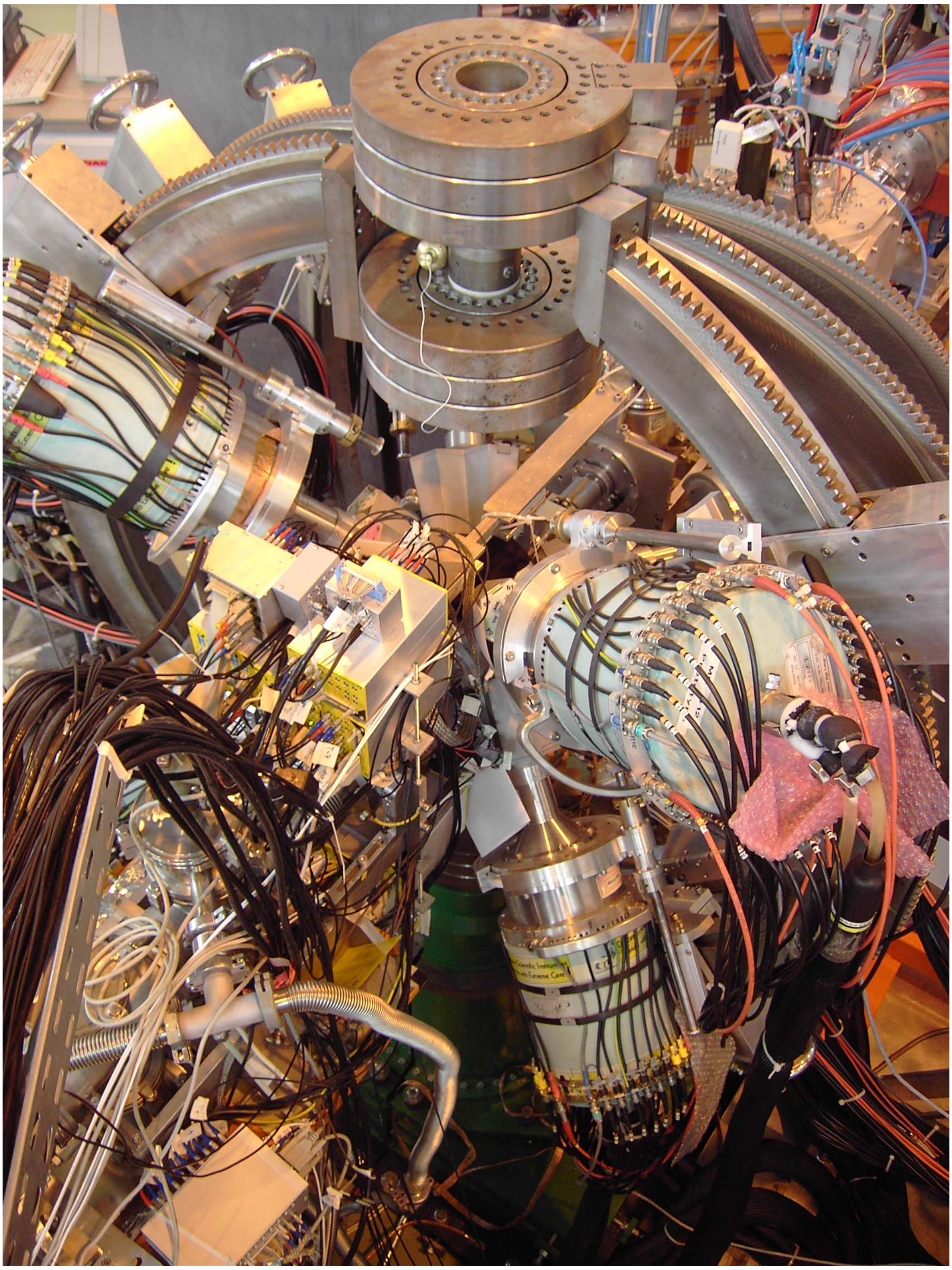

Figure 3.13: T-REX setup with seven MINIBALL clusters around it. Beam enters from the top right. The readout electronics of the barrel and CD detectors is in the left center of the picture.

Target Ladder

In order to be able to slide the vacuum chamber off the silicon barrel as described above, the target ladder which is mounted on the bottom of the vacuum chamber has to be retracted so far that its top is lower than the PCB of the CD detectors. To this end the target ladder is mounted on a magnetically coupled linear feedthrough that has a stroke of 150 mm while adding only 240 mm to the height of the chamber, thus narrowly fitting between the chamber and the mounting structure of MINIBALL. The stroke of 150 mm allows one to use target ladders with enough space for four targets plus the diamond detector that is used for the beam focusing.

A second target ladder has been designed for the use of a tritium loaded titanium foil as target for (t,p) reactions, fulfilling safety requirements of the radiation protection, see appendix B. This way the target ladder can be dismounted and transferred e.g. to a glove-box without extra safety precautions.

Cabling and Feedthroughs

Since the vacuum chamber is designed to be slid off the silicon barrel (in upstream direction) all signals from the CD and barrel detectors have to be routed downstream where a flange with 16 individual feedthroughs is located. These feedthroughs are PCBs that are glued into the metal part of the feedthroughs with connectors on the vacuum and the air side.

Each CD quadrant requires one feedthrough for its 40 channels (16 annular Rings and 24 radial Strips). These feedthroughs have a 50 pin SMC connector on the vacuum side which is connected by a special cable to the 34 (16 rings plus the guard ring and 17 ground connections) and 50 (24 strips plus the guard ring and 25 ground connections) pin connectors on the CD. On the outside of the vacuum chamber the feedthroughs have two 26 pin SMC connectors, one with the 16 rings and one with the 24 rings.

Each barrel quadrant also needs one feedthrough. These have two 26 pin SMC connectors on the vacuum side (one for the forward and one for the backward detector stack), which are directly connected to two other SMC connectors on the outside.

All cables from the feedthroughs to the preamplifiers are kept as short as possible by placing the preamplifiers as close to the feedthrough flange as possible (20–50 cm length). This and the shielding around each cable help keeping the noise level as low as possible, making a trigger threshold as low as 300 keV possible.

3.4.3 Electronics

MINIBALL Detectors

The readout of the 168 signals from MINIBALL (eight cluster × three crystals per cluster × (one core signal + six segment signals)), which were amplified by the integrated preamplifiers of the MINIBALL detectors, is done with digital electronics using XIA DGF-4C modules [XIA]. The DGF modules first digitize the signals with a 12 bit flash ADC[16] at a sampling frequency of 40 MHz, i.e. every 25 ns. In the readout mode chosen for this experiment the digitized signals are then processed inside the module to provide energy and time information of all channels above threshold.

---

[16] **A**nalog to **D**igital **C**onverter

The DGFs are gated by a so-called GFLT[17]. The GFLT is a 800 μs long window that opens when the charge-bred ions are extracted from the EBIS (the so-called on-beam window) and a second window of the same length that is opened after the readout of the data of the on-beam window has finished and allows to measure background between the EBIS pulses (the so-called off-beam window). Only signals within these GFLT time windows are processed. A more detailed description of the specific digital readout for the MINIBALL array can be found in [Lau04].

Cabling

The cables go from the feedthroughs to different adapter PCBs, which are attached to the MPR-16[18] preamplifiers in the case of the barrel signals or to the MUX-16/32[18] multiplexers in the case of the CD signals. The adapter PCBs of the MPR-16 route the strip signals to the 25 pin SUB-D connectors of the MPR-16, filter the high voltage that is applied to the other side of the strips and have two other LEMO connectors to connect the ΔE and E_{Rest} signals to the MSI-8s[18]. The adapter PCBs for the 16 CD rings are just adapters from the SMC connectors to the 25 pin SUB-D connectors of the MUX-16/32, while the adapter PCBs of the 24 CD strips reduce the number of signals to 16 by pairing off the 16 innermost strips before sending them to the MUX-16/32.

CD Detectors

Each CD detector stack has 128 Channels (4 Quadrants with each 16 annular rings and (effectively) 16 radial strips) plus 4 channels for the E_{Rest} pad detectors. Reading out each of these channels individually would require more than 4 ADCs for just one CD detector which should be hit by only one particle at a time in case of transfer reactions.

To reduce the amount of ADC channels needed so-called multiplexers (MUX-16/32[18]) were used. Each takes 16 channels as input and gives out four signals: the amplitudes of up to two channels and two analog signals that identify the channels. In addition, up to eight modules can be connected by one bus, so that just four ADC channels could read out a total of 128 channels. However, connecting two (or more) modules means that only one of them can have up to two hits (within 30 ns) otherwise the event is rejected. Since one hit of a CD quadrant creates a signal on the front-side rings as well as the backside strips the MUX that read out the front-side have to be on a different bus than the ones for the backside. This leaves the possibilities to either connect the front (and rear) strips of all quadrants with one bus or split the quadrants on two or four buses with the trade-off of less dead time per quadrant for the cost of more ADC channels.

Barrel Detectors

The readout of only one side of the resistive strips allows one to measure the position of the hit along the strip by comparing the measured energy of the strip to the total energy deposited i.e. the measured energy of the rear side of the detector. Due to the resistive charge splitting an unbiased trigger cannot be derived from the strip signals.

---

[17] **G**lobal **F**irst **L**evel **T**rigger

[18] from Mesytec [Mes]

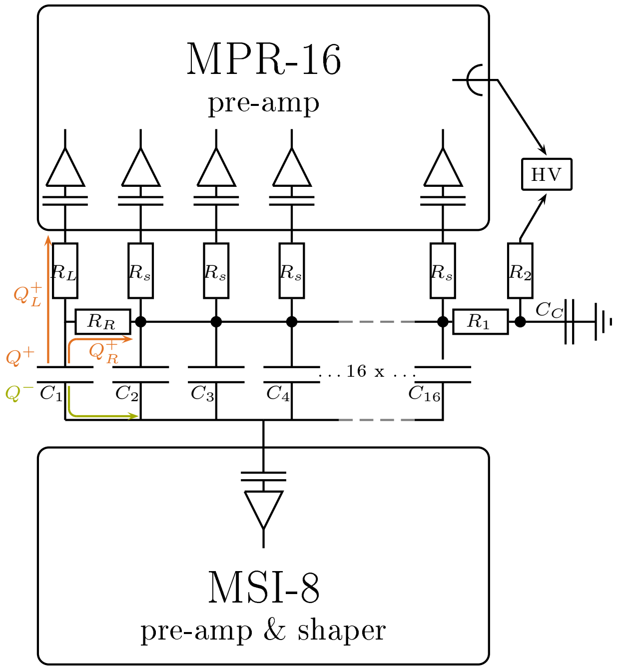

Figure 3.14: Schematic of position dependent energy of barrel rear.

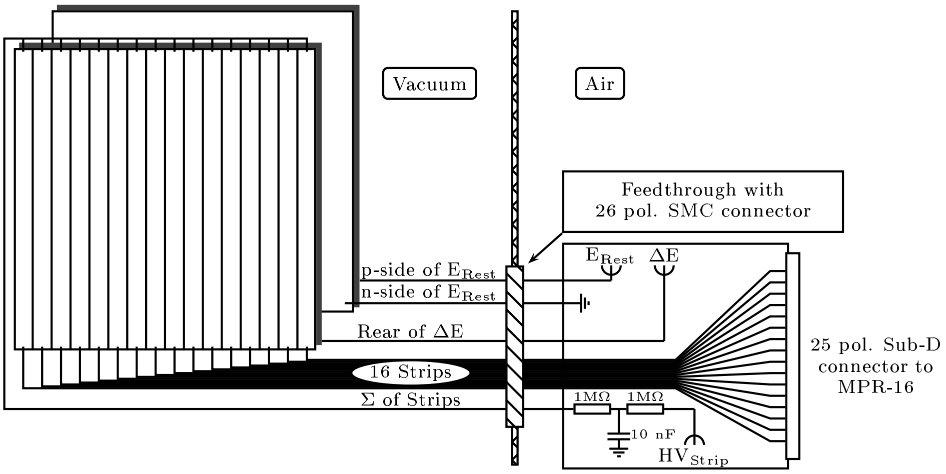

Figure 3.15: Electronics of one barrel stack.

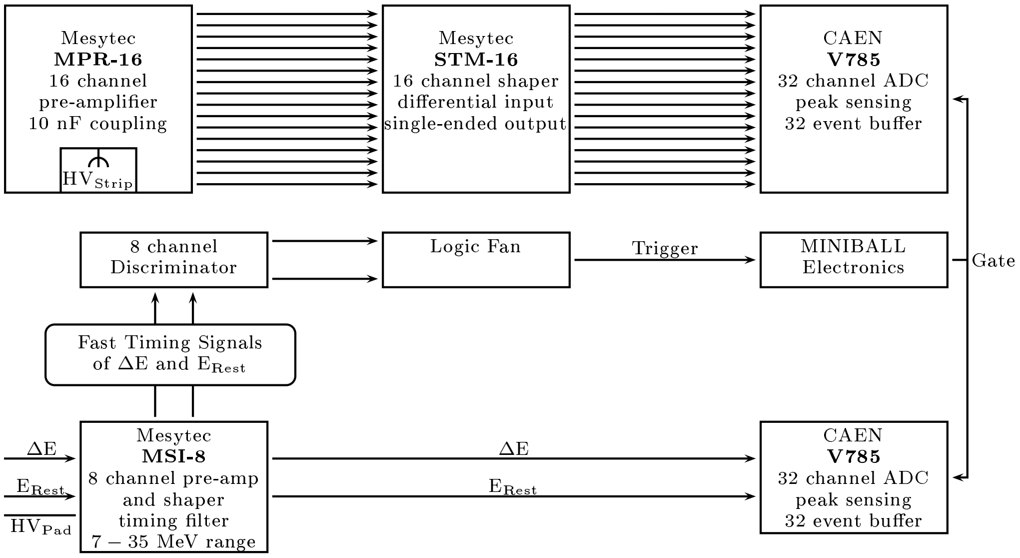

Figure 3.16: Trigger and readout logic of one barrel stack.

This means that the MUX modules are not an option for the barrel detectors, as they need to be able to trigger on each channel independently to do the multiplexing. Here conventional single strip readout was chosen. All strips are read out by 16 channel preamplifiers (MPR-16) and shapers (STM-16), so that each barrel detector stack requires 16 ADC channels for the strips and one channel each for the rear of the ΔE and the E$_{\mathrm{Rest}}$ detectors.

The charge Q^+ deposited in one strip is split in two parts which are collected on the two ends of the strip (see figure 3.14). The amount of charge that goes to the ends of the strip is determined by Ohm's law and is in first order linear to the position of the hit.

The charge that flows to the side where all strips are connected together (Q_R^+ in figure 3.14) goes mostly via all 16 strips into the MPR-16 preamplifiers with a time constant $\tau = R_S \cdot C_S 3\,\mathrm{k}\Omega \cdot 125\,\mathrm{pF} = 375\,\mathrm{ns}$, as the time constant of R_1 and C_C is even larger ($\tau = 10\,\mathrm{ms}$). Since all positive charge on the strips is mirrored by the same negative charge on the rear, a part of the rear charge Q^- that depend on the position of the hit reaches the MSI-8 preamplifier and shaper with a slower time constant, resulting in a position dependent height of the shaped signal. This position dependence has to be corrected to achieve the full resolution of the detector (see chapter 4).

ADC

For the AD conversion standard 32 channel VME[19] peak sensing ADCs (CAEN V785) with 8 V input range and 12 bit dynamic range had been used. To optimize the dead time of the system while keeping the number of ADCs needed low, the ADCs have been arranged in two independent so-called trigger groups of three ADCs each, one for the top and left detectors and one for the bottom and right detectors.

---

[19] **V**ersa **M**odule **E**urocard

The trigger groups are gated by OR-ed triggers from the rear sides of the corresponding forward ΔE - E_{Rest} detectors, backward ΔE detectors and the MUX triggers of the two quadrants of said group. The gate signals are also sent to two DGF modules to create timestamps, which allows to determine particle-γ coincidences later.

The integrated signals of the beam diagnostics detectors are fed directly into an independent ADC which is gated by the on- and off-beam windows.

Aside from the different amount of ADCs and the different creation of the trigger signals, the electronic setup is very similar to the MINIBALL setup used for Coulomb excitation reactions (see [War08]).

Scaler

For monitoring purposes a 32 channel scaler (SIS3820 [Str]) is read out every second.

3.5 Bragg Chamber

At the end of the beam line, approximately 4 m downstream of the target, a Bragg chamber is installed [Wei06]. This Bragg chamber consists of four components: an entrance foil that doubles as a cathode, a gas filled drift volume, a Frisch grid and an anode. The homogeneous electric field created by the cathode and anode is parallel to the path of the particles in the Bragg chamber, i.e. the beam line. The charge created by the ionizing particles is drifted by the electric field to the anode and cathode, creating a signal whose amplitude versus time information is equivalent to the energy loss of the particle versus the length of its path in the Bragg chamber.

The signal is digitized by a sampling ADC (SIS3300 [Str]). The maximum slope of the signal is proportional to the maximum specific energy loss of the particle which depends strongly on its charge Z, while to maximum height of the signal is the total energy deposited by the particle in the Bragg chamber and is proportional to the mass of the particle. The two quantities Z and A of a particle can thus be determined from the signal of the Bragg chamber, allowing an identification of the isotope, see also figure 5.8.

Chapter 4

Data Analysis

The data analysis framework, which was written as a part of this thesis, consists of four major units which are all based on C++ and ROOT [Bru97].

The units are unpacking and event building, calibration, particle identification and kinematic reconstruction, and a higher level physics analysis. To allow for data checks and an independent development all four units hand over the data through a file interface based on ROOT trees. The individual steps of processing the data are described in the following sections.

4.1 Unpacking and Event Building

The first program reads the files written by the data acquisition MARaBOU [Lut03] and performs an event building. This is necessary because all data during a full beam spill is written into the buffers of the modules before being read out during the spill pauses. Hence the event structure of the data stream does not contain any real physics event structure, which has to be rebuild. The output of the data acquisition is written in the MED[1] format as described in [Lut05].

The data read from the MED-file is organized into ADC and DGF subevents while the former are matched up with the events in the DGF timestamper. This allows one to put a broad coincidence window of 1 µs between particles (ADC events) and γ-rays (DGF events). This window is rather wide compared to the 150 ns used later on, which ensures that all true particle-γ coincidences are preserved while the introduced random coincidences can be sorted out later.

For data taken with beam the output is written to four separate files, one containing the independent scaler and Bragg chamber data, another the off-beam data. The two last files both contain the on-beam data, which is split into those events that lie within 125–200 µs after the EBIS pulse is registered by the corresponding DGF module, and those outside said window. The window is chosen such that it coincides with the beam (see figure 4.1) for further suppression of β-decay background. For data taken with calibration sources only two files are written, one with the scaler data and one with both the on- and off-beam data.

---

[1] **m**bs **e**vent **d**ata

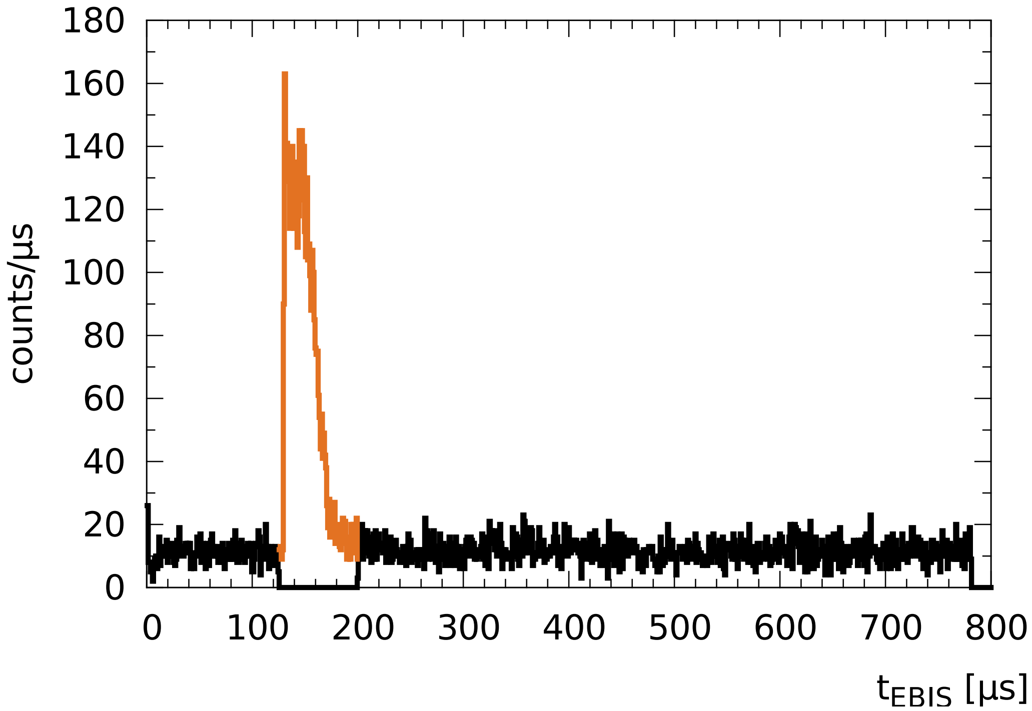

Figure 4.1: Time structure of one EBIS spill. The background is mostly from β-decay and the orange part of the spectrum marks the time window used in the later analysis.

4.2 Calibration

This part of the analysis calibrates the raw data of the ADCs and DGFs and assigns the calibrated data to the different detectors.

4.2.1 Calibration and Efficiency of MINIBALL

For the energy and efficiency calibration of the MINIBALL detectors separately a ^{60}Co and a ^{152}Eu source are mounted at the target position.

The energy calibration was performed with an automatic peak finder from [Lut03], which matches the peaks found in the uncalibrated spectra of each germanium crystal with the known lines of the source. The peak finder assumes a linear energy calibration and writes the determined gains and offsets to file.

The absolute efficiency calibration is done by using the sum-peak method [Kim03] on the ^{60}Co data to obtain absolute efficiencies at the energies of the two coincident γ lines emitted in the decay of this isotope. The relative efficiencies obtained by comparing the strength of the photo peaks in the ^{152}Eu data with literature values were corrected for the properties of a ^{152}Eu source as described in appendix A.

The resulting data points are fitted by an efficiency function parametrized as (taken from [Deb84], with $a_5 = 0$)

$$\varepsilon_{ph}(E) = a_1 \log E + a_2 \frac{\log E}{E} + a_3 \frac{\log^2 E}{E} + a_4 \frac{\log^4 E}{E}. \tag{4.1}$$

The photo peak efficiencies used in the analysis can be seen in figure 4.2.

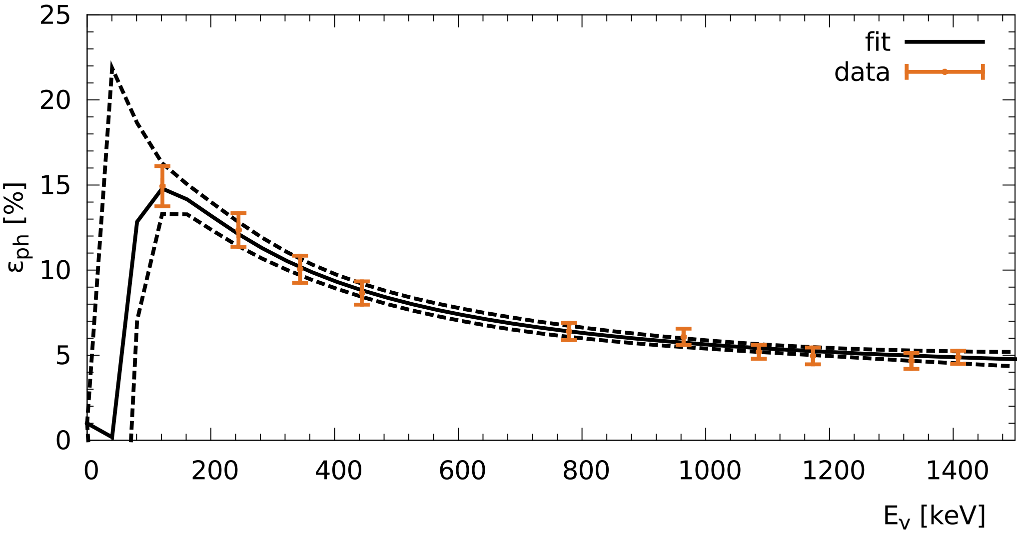

Figure 4.2: Photopeak efficiency of MINIBALL with addback. The dashed lines indicate the error of the fit.

Isotope	*Energy of α in keV*	*branching ratio in %*
^{148}Gd	3182.69	100.00
^{239}Pu	5156.59	70.77(14)
	5144.3	17.11(14)
	5105.5	11.94(7)
^{241}Am	5485.56	84.4(5)
	5442.80	13.1(3)
^{244}Cm	5804.77	76.4(10)
	5762.64	23.6(10)

Table 4.1: The energies of the quadruple α source as they are implemented in the Geant4 simulation. The remaining branches in the decay of ^{239}Pu, ^{241}Am, and ^{244}Cm are all below 0.05 %, 2 %, and 0.02 %, respectively.

4.2.2 Energy Calibration of $\triangle$E Barrel Detectors

The energy calibration of the barrel detectors is complicated by the fact that the foils in front of the forward detector cause a position dependent energy loss of the alpha particles emitted by the quadruple α source (^{148}Gd, ^{239}Pu, ^{241}Am, and ^{244}Cm, see table 4.1) that was used. This was addressed by using a simulation of the α source to determine an average energy for each α line and strip of the detectors.

Another issue with the energy calibration of the rear of the strip detectors is the position dependence of the signal (see chapter 3) that has to be corrected for. The left panel of figure 4.3 shows the correlation of the uncalibrated rear energy of one barrel detector versus the uncalibrated position along the one strip.

The position along a strip is determined by the ratio between the strip signal and the signal from the rear which itself depends on the position. To solve this circular dependence an iterative method was chosen. First the position is calculated using the uncorrected energy, i.e. the rear signal. The energy is then corrected for the position dependency. With this corrected rear energy the position is then calculated

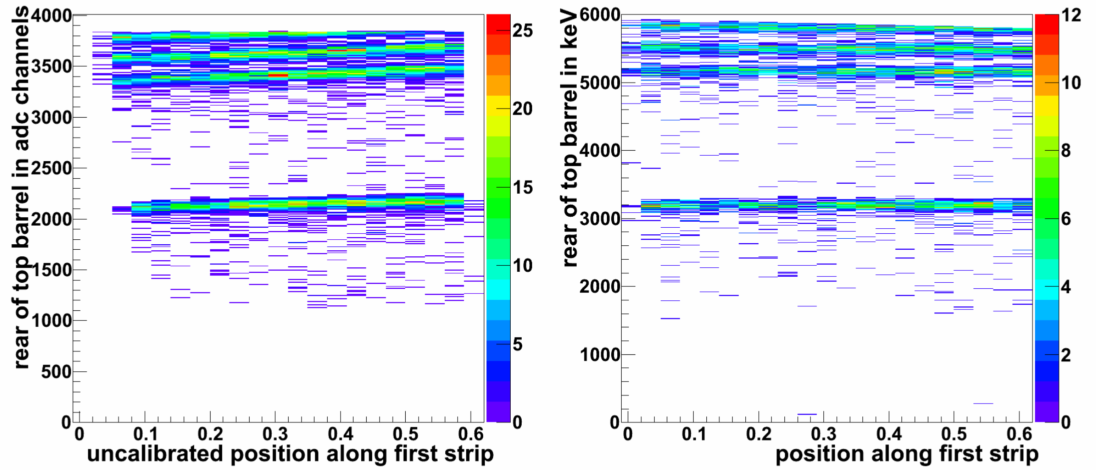

Figure 4.3: The amplitude of the signal from the rear side of the backward barrel detector versus the position along the first strip, uncalibrated on the left, calibrated on the right. The data shown is from a run with a quadruple α source which contains ^{148}Gd, ^{239}Pu, ^{241}Am, and ^{244}Cm. The energy loss in the 2 μm thin Mylar foil between the source and the detector is accounted for.

again. This corrected position could be used again to get a second order correction of the energy but since the energy doesn't show any discernible position dependence after the first correction (see right panel of figure 4.3) this is not necessary.

For a strip of length L the position resolution Δp depends mostly on the ratio between the electronic noise N and the strip signal S that is in the range between 0 and the amplitude of the rear signal R

$$\Delta p = L\sqrt{N^2\left(\frac{1+S^2/R^2}{R^2}\right)} \in \left[\frac{N}{R}L, \sqrt{2}\frac{N}{R}L\right] \tag{4.2}$$

For a typical noise $N = 100\,\mathrm{keV} FWHM$ and an energy loss $R = 2000\,\mathrm{keV}$ for protons this results in a position resolution of about 7 % which corresponds to $\Delta p \lesssim 3.5\,\mathrm{mm}$. Due to this the barrel detectors were divided into artificial pixels of $3.125 \times 3.125\,\mathrm{mm}^2$, i.e. 16 bins along each of the 16 strips of the detector.

4.2.3 Calibration of E$_{\mathrm{Rest}}$ Detectors

The E$_{\mathrm{Rest}}$ detectors can not be directly calibrated with an α source as it was done for the ΔE detectors since the latter stop any α particles. One possibility to calibrate the E$_{\mathrm{Rest}}$ detectors is data taken with γ-ray sources, where γ-rays that were Compton scattered in the E$_{\mathrm{Rest}}$ detectors are detected in the MINIBALL detectors, see figure 4.4. However the energy of the highest (strong) γ-line of a ^{152}Eu source is 1408 keV and the energy deposited in the E$_{\mathrm{Rest}}$ detectors is limited to about 1200 keV. Therefore this calibration can not be expected to be very precise at the higher energies a proton from transfer reactions can deposit in one of these detectors (which can be as high as 15 MeV).

Another method to calibrate the E$_{\mathrm{Rest}}$ detectors is to use the energy deposited by the protons and deuterons in the calibrated ΔE detectors and calculate from this the

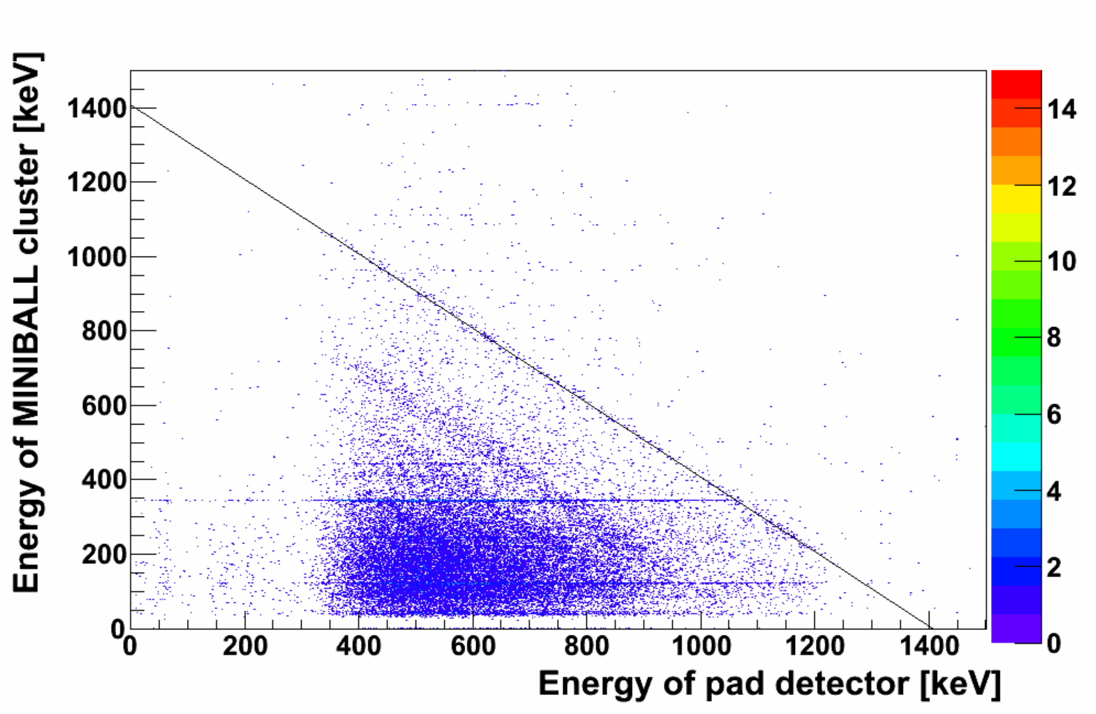

Figure 4.4: The γ-ray energy detected with MINIBALL versus the energy in the pad detectors for a ^{152}Eu source. One can clearly see the anti-correlation of the 1408 keV line, indicated with the black line.

	a_0	a_1	a_2	a_3
particles top/left	−22.47	−26.70	1000.00	−1.235
particles bottom/right	−6.670	−5.958	998.54	−1.208
γ-rays		−18.70	−10.29	−0.946
addback width		−0.768	56.21	−0.802

Table 4.2: Fit parameters of the walk correction. The delay between particles and γ-rays is different for the two halves of the barrel that are in separate trigger groups (top and left quadrants in first, bottom and right quadrants in the second group).

energy the particle has deposited in the $\mathrm{E}_{\mathrm{Rest}}$ detectors. The code to calculate the energy of the protons and deuterons after the ΔE detectors is a C++-version of the irma code [Ern84].

Both methods were used in the actual calibration of the $\mathrm{E}_{\mathrm{Rest}}$ detectors, the first to determine the offset and the second to correct and cross-check the gain of the first.

4.2.4 Timing

One important aspect of reducing background from random coincidences is the timing between γ-rays and particles. Leading edge discriminators generate the triggers used to create the particle timestamps. A digital version of this is used by the DGFs to determine the timestamp of a γ-ray event. As a result the time distribution

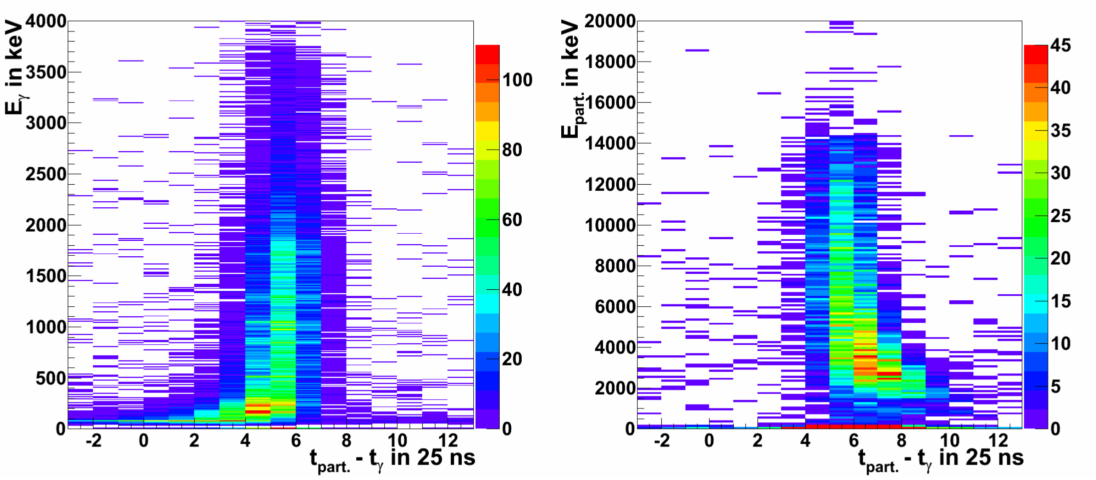

Figure 4.5: The left panel shows the γ-ray energy versus the time difference between particles and γ-rays for particle energies above 5000 keV in the top/left trigger group. The offset is due to different delays for the signals from γ-rays and particles. The right panel shows the corresponding particle energy versus time difference spectrum in coincidence with γ-ray energies above 2000 keV.

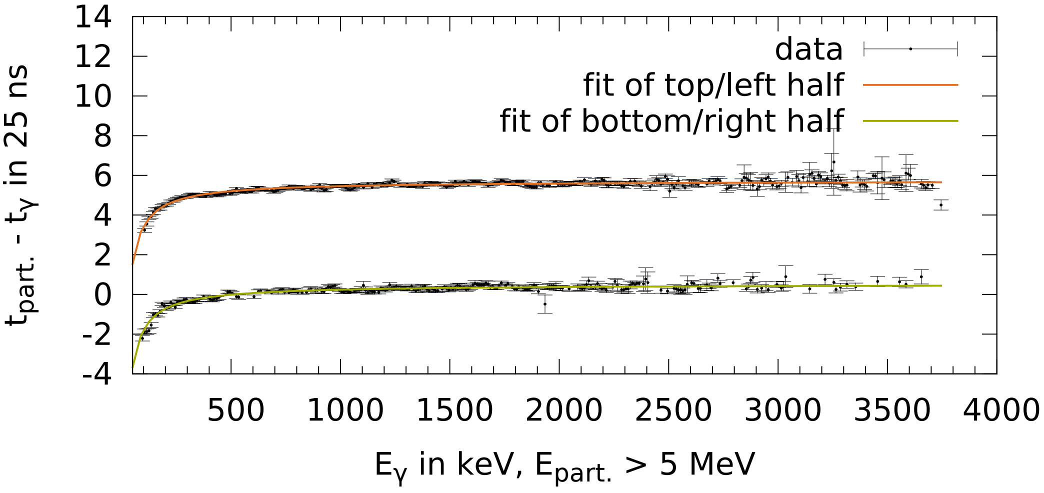

Figure 4.6: Fit of the walk of the γ-ray timing. The data points are the centroids of figure 4.5, once in coincidence with particles detected in the top/left quadrants of the barrel and once in coincidence with those from the bottom/right quadrants.

of both the γ-ray and the particles show a distinctive walk for lower energies. By cutting on events with either high γ-ray or particle energies ($>$ 2000 keV and 5000 keV, respectively) one can see the energy dependence of the particle and γ-ray timing as shown in figure 4.5.

The two spectra are for hits in one half of the silicon barrel (top and left detectors). The offset between the γ-ray and particle triggers depends on the delays in the analog electronics, which is different for the two trigger groups. Since a simple polynomial function doesn't describe the observed relation between walk and energy very well, the walk was fitted with a function derived from an exponential decay:

$$f(x) = a_0 + 1 - a_1 e^{a_2 x^{a_3}}. \tag{4.3}$$

A function of the same shape without the offset ($a_0 = 0$) was used to fit the width of the distribution. Figure 4.6 shows the fit of the walk depending on the γ-ray energy and table 4.2 shows the parameters derived from the fits.

The obtained energy dependency of the timing was used to correct the timing information of the γ-rays and particles, while the energy dependence of the width of the coincidence peak was used in the next program for the addback routine.

4.3 Kinematic Reconstruction

From the calibrated data of the detectors the kinematical properties that are not directly measured of both the γ-rays and the particles need to be reconstructed.

For a particle this means to calculate its direction from its position in the detectors. This can be used to identify what kind of particle it was and its original properties. The recovered original energy and direction of the detected recoil allow the reconstruction of the momentum four-vector of the ejectile.

4.3.1 Target Position

The expected energies of the protons and deuterons depend on two quantities. One is the beam energy, which is fixed by the magnetic rigidity selected by the bending magnet, and the other is the ϑ_{lab} angle under which it is observed. The ϑ_{lab} angle is determined by the position of the detector relative to the target. The distance of the barrel detectors to the beam axis is fixed by the mounting structure while the position of the target along the beam axis is not as well defined due to the long linear motion feedthrough. Comparison of the observed energies of the elastically scattered protons and deuterons with the energy expected from kinematic calculations which included the energy losses in the target and the foils showed a systematic discrepancy (see figure 4.7).

To determine the real position of the target, the difference between the observed and expected energies of the elastically scattered protons and deuterons was calculated for different target positions. The target position for which the differences of both the elastically scattered protons and deuterons were minimal was adopted for the further analysis. The adopted values are a shift of 2.5(3) mm for the d (^{22}Ne, p) ^{23}Ne and 2.9(4) mm for the d (^{30}Mg, p) ^{31}Mg reaction along the beam line, measured from the center of the T-REX setup (the target ladder was dismounted in between the experiments).

To avoid this problem in future experiments an additional guidance of the target ladder was installed after the 2008 experiment, see appendix E.

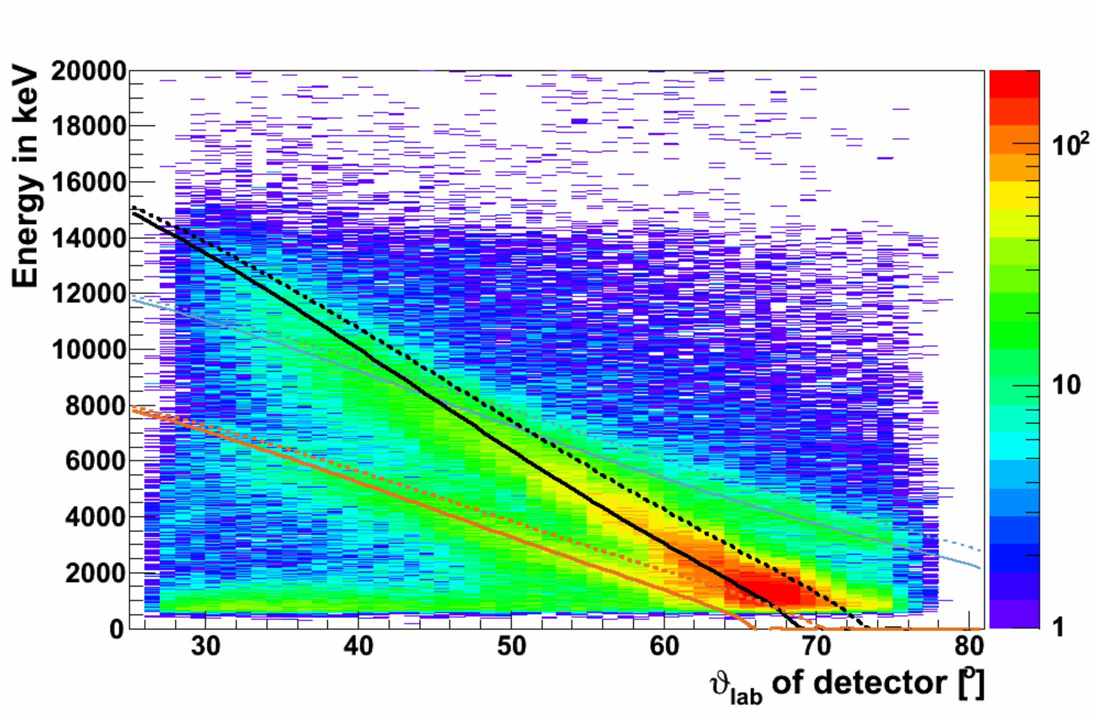

Figure 4.7: This figure shows the effect of the target shift observed in the data of the forward barrels for the d (^{30}Mg, p) ^{31}Mg reaction. The angles on the x-axis are measured from the origin of the detector coordinates. The dashed lines are the expected energies of elastically scattered protons (orange), deuterons (black), and protons from a transfer reaction to the ground state (blue), assuming that the target is positioned at the origin of the detector coordinates. The solid lines are the corresponding energies if the target is shifted by 2.9 mm in beam direction.

4.3.2 Addback of MINIBALL Detectors

As discussed in section 3.3 the coincident signals from the three crystals in one MINIBALL detector can be used to reconstruct the full energy of γ-rays that were Compton scattered from one crystal into another. To avoid the addback of uncorrelated hits in different crystals it is necessary to use a narrow coincidence window. In the present case the energy dependent width of the γ-particle coincidences was used for this. The effect of the addback can be seen in the photopeak efficiencies as shown in appendix A. An up to 30 % higher efficiency can be obtained at energies above 2.5 MeV.

4.3.3 Position of the MINIBALL Detectors

In order to perform a Doppler correction of the γ-rays, which are emitted by the ejectile at 5–8 % of the speed of light, one needs to know the direction into which the γ-ray was emitted. The position of the MINIBALL detectors can be (partially) reconstructed e.g. from the d (^{22}Ne, p) ^{23}Ne data by measuring the Doppler shift of the 1017 keV γ-line in ^{23}Ne for each segment of the MINIBALL detectors.

This shift depends on the angle between the emitting particle and the γ-ray that is determined by the polar and azimuthal angles of both the particle and the γ-ray.

	Crystal A [°]	*Crystal B* [°]	*Crystal C* [°]
Cluster 1	139	116	126
Cluster 2	62	81	62
Cluster 3	61	88	62
Cluster 4	136	133	116
Cluster 5	-	-	-
Cluster 6	65	85	64
Cluster 7	-	128	144
Cluster 8	64	65	84

Table 4.3: The angles of the MINIBALL cores as determined from the Doppler shift of the 1017 keV line from the d (^{22}Ne, p) ^{23}Ne reaction. One cluster (5) and one crystal (7A) were not operational.

However, the ^{23}Ne from the reaction has a maximum scattering angle $\vartheta_{\text{lab}} \lesssim 5°$ and the opening angle of one segment of a MINIBALL detector is of the same order. Consequently the influence of the direction of the emitting particle and the azimuthal angle of the γ-ray cannot be seen in the measured shifts. The polar angle determined does not suffer an increased uncertainty from this, as it is determined as the average over all azimuthal angles.

Therefore the measurement of the Doppler shift for one segment of MINIBALL allows determining its polar angle with sufficient accuracy to apply a Doppler correction to both the d (^{22}Ne, p) ^{23}Ne and the d (^{30}Mg, p) ^{31}Mg data sets.

Table 4.3 shows the angles of the crystals as they were determined by the described method.

4.3.4 Particle Identification

The particle identification is performed in two steps. The first one uses the ΔE - E_{Rest} signals to identify the different particles by their characteristic energy loss. The second exploits the characteristic relation between energy and ϑ_{lab} to identify the reaction that produced the particle.

The ΔE - E_{Rest} relations are calculated for each strip using the minimum and maximum effective thicknesses of the detector. For each, the energy range was made broader by adding and subtracting 400 keV to the ΔE energy to account for the detector resolutions of both the ΔE and E_{Rest} detector. If the particle deposited energy in the E_{Rest} detector, these calculations can be used to determine whether it was an electron, proton, deuteron, or triton (see figure 4.8). In the regions where the cuts are overlapping, the proton cut takes precedence over the deuteron cut which in turn takes precedence over the triton cut. This means that entries in the overlap region of the proton and deuteron cuts are assigned to be protons and those in the overlap region of deuteron and triton cuts are assigned to be deuterons. This was done to ensure that all protons are identified as such while the introduced background of wrongly identified deuterons is negligible (the same holds for deuterons and tritons).

If the particle was stopped in the ΔE detector, it is still possible to differentiate between the reaction channels due to the different kinematics. Thus for each pixel the energies of elastically scattered protons and deuterons as well as protons from transfer reactions are calculated for each of the four ϑ_{lab} angles of the corners of the pixel. This is done once for full beam energy and once for the energy of the projectile

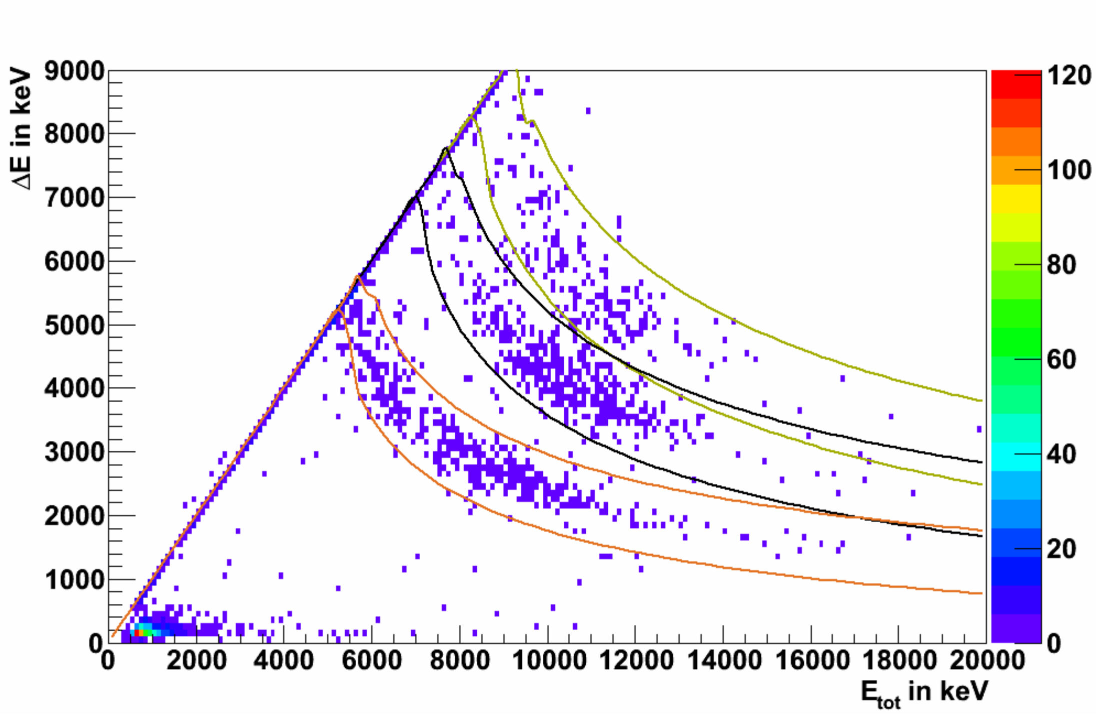

Figure 4.8: Particle identification via ΔE - E_{Rest}. Shown is the energy loss in the top barrel strip detector versus the total detected energy for one strip (strip 12). Electrons from β decays are clearly visible in the lower left corner while protons, deuterons, and tritons show up as three "bananas" at higher energies. The cuts for protons (orange), deuterons (black), and tritons (green) are from energy loss calculations for this strip. In the regions where the different cuts overlap the proton cut takes precedence over the deuteron cut which takes precedence over the triton cut.

after traversing the target (reactions at the front and back of the target). For each of these energies the energy loss in the target and foils is calculated to define the minimum and maximum energy of the recoil. These two energies are then used to identify the stopped particle if the energy deduced from the kinematics is low enough for the particle to be stopped in the ΔE detector, as shown in figure 4.9.

In order to avoid background from misidentified stopped particles the cuts for the identification of these were not broadened like the ΔE - E_{Rest} cuts. The necessary efficiency correction is discussed in section 4.4.

4.3.5 Reconstruction of Energy Loss

Once a particle is identified its energy loss in the 2 and 12 µm thick Mylar foils in front of the backward and forward barrel detectors can be calculated. Here the angle is taken into account at which the particle penetrated the protection foils to deduce its effective thickness. This energy is in turn used to calculate the "correct" energy of a particle emitted from the center of the target in the direction it was detected. The obtained energy of the light recoil at the center of the target can be used to reconstruct the four-vector of the heavy ejectile.

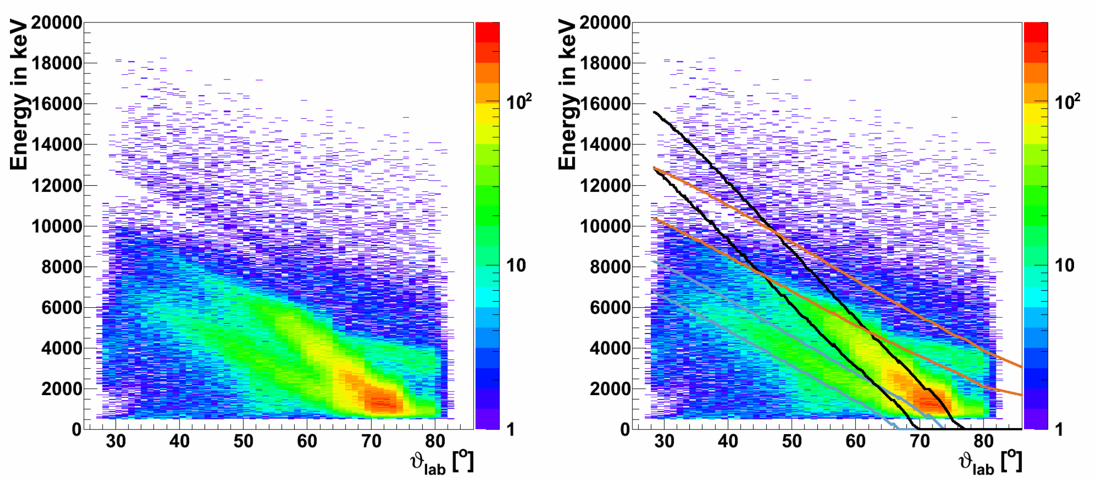

Figure 4.9: The left panel shows the energy versus ϑ angle in the laboratory frame for particles stopped in the ΔE detector. The gap at 12 MeV and 30° stems from deuterons that are energetic enough to punch through the ΔE detector and are thus not shown in this plot. The overlapping cuts used for particle identification are shown in the right panel. The band for protons from transfer reactions populating states from the ground state up to 221 keV excitation energy is orange, the cut for elastically scattered protons blue, and the cut for elastically scattered deuterons black.

4.3.6 Reconstruction of Ejectiles

The heavy ejectiles of the transfer reactions (^{23}Ne and ^{30}Mg) are not detected directly as their maximum scattering angle in the laboratory frame is only $\approx$ 3–5°. The Doppler correction however depends on the velocity of the emitting nucleus (in this case the ejectile), so it is necessary to reconstruct the kinematics of the ejectiles from the energy and angle of the recoiling protons.

This reconstruction is based on the energy and momentum conservation in the center of mass frame. The momentum of the ejectile is the inverse of the momentum of the recoil and the energy of the ejectile is the total energy in the center of mass frame before the reaction minus the energy of the recoil (in the center of mass frame).

The difference between the reconstructed energy/mass of the ejectile and the mass of the ejectile in its ground state should be the excitation energy of the state populated in the reaction. However, the energy loss of the beam in the target (1 mg cm^{-2} PE), which amounts to almost 20 %, leads to a large spread of recoil energies for a given angle. Hence the resolution of the reconstructed excitation energy of the ejectile depends strongly on the target thickness and is generally quite low, especially if compared to the small excitation energies of the 50.5 or 221 keV states in ^{31}Mg, see figure 5.11.

4.4 Reaction Analysis

The information of the γ-rays and particles can now be used to create the angular distributions of the elastically scattered protons and deuterons as well as those of protons from transfer reactions. In order to compare the data with DWBA calculations

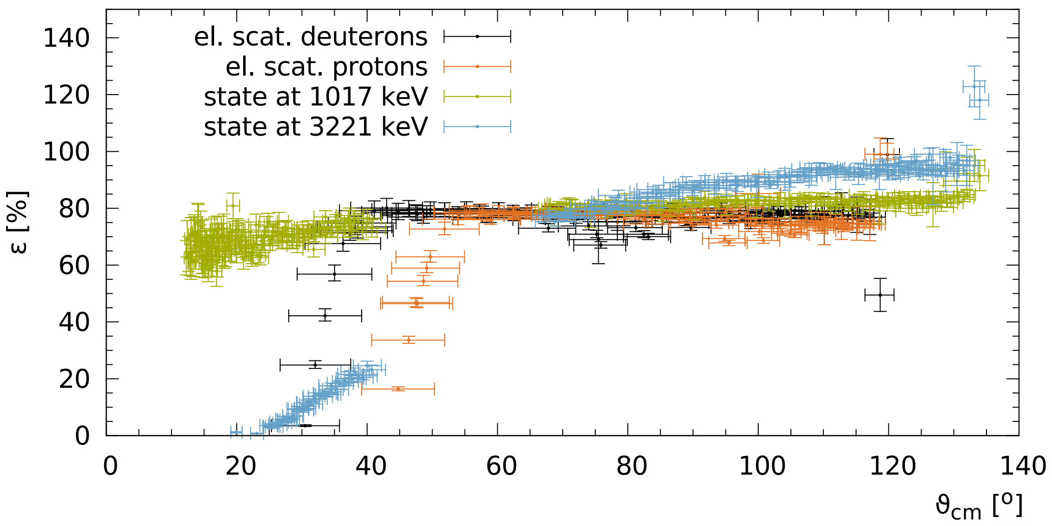

Figure 4.10: Efficiency of particle identification and excitation energy cuts for the d(^{22}Ne, p)^{23}Ne reaction. The reduced efficiencies at small ϑ_{cm} angles (corresponding to large ϑ_{lab} angles) for the elastically scattered deuterons and protons stems from the low energy of the particles at these angles, causing them to drop below the detection threshold. The same effect is visible for the protons from transfer reactions to a 3221 keV state whose energy at backward laboratory angles is very low.

it is helpful to have the angular distributions in the center of mass frame. In the following the steps needed to create such angular distributions are shown with examples from the d(^{22}Ne, d)^{22}Ne and d(^{22}Ne, p)^{23}Ne reactions.

4.4.1 Identifying the Reaction

The first step is to count for each detector pixel the hits that fulfill the following cuts:

- particle identification cut (the ΔE - E$_{\text{Rest}}$ and the E-ϑ_{lab} cut),
- cut on the excitation energy to reduce background and exclude feeding from higher lying states (the latter applies only for transfer reactions), and
- coincident γ-rays whose Doppler corrected energy is inside a certain window (only for transfer reactions that are tagged by γ-rays).

In the case of particle-γ coincidences the background from random coincidences is subtracted and the obtained number of particles is corrected for the γ-ray efficiency of the MINIBALL detectors. If a state is depopulated by more than one γ-ray transition the efficiency and background corrected distributions are added.

The cuts used for the particle identification and the cut on the excitation energy can introduce a detection efficiency that is non-uniform across the barrel detector. In order to correct for this the Geant4 simulation (appendix D) was used to determine this efficiency by comparing the number of simulated particles that would have hit a pixel with the number of particles detected and correctly identified in that pixel (see figure 4.10). One can see the effect of the detection threshold for both elastically

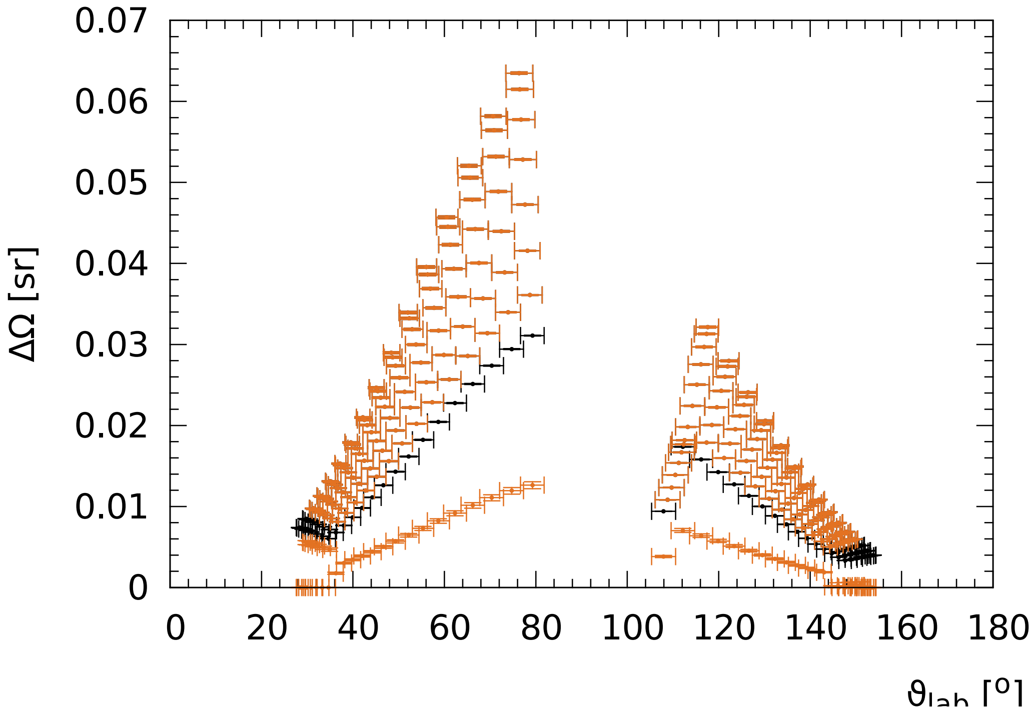

Figure 4.11: Solid angle covered by the pixels of the barrel detectors versus their ϑ_{lab} angle, assuming a target shift of 2.5 mm and including the effect of broken strips. The solid angle for particles stopped in the ΔE detector is shown in black and the solid angle for particles that are identified in the E_{Rest} detector in orange.

scattered particles and protons from transfer reactions to a 3221 keV state for which the Q-value of the reaction is close to zero.

4.4.2 Differential Cross Sections

The next step is to calculate from these counts the differential cross section by dividing them by the solid angle of the corresponding pixel in the laboratory frame. The solid angle covered by one pixel of the ΔE detector differs for particles that are stopped in the ΔE detector and those that are not. At the edges of the detector the latter might miss the E_{Rest} detector, which has the same size as the ΔE detector but is 2.4 mm further away from the beam axis, thus reducing the covered solid angle. The solid angle covered by one pixel is determined by dividing the pixel into two triangles for which the solid angle can be calculated using the expression from [Oos83]. The result for a target shift of 2.5 mm is shown in figure 4.11, calculated for the ^{22}Ne data with the forward right and backward top detector (three single strips were not working correctly and were omitted in the analysis).

To convert the obtained differential cross sections into the center of mass frame the ϑ_{cm} angle of the center of each pixel is calculated and the solid angle covered by the pixel is transformed to the center of mass frame by multiplying it with $d\Omega_{lab}/d\Omega_{cm}$.

The obtained angular distributions (both in the laboratory and the center of mass frame) have to be divided by the integrated luminosity to obtain the differential cross section. The integrated luminosity is determined from comparison of the elastically scattered deuteron data to a DWBA calculation.

4.4.3 Systematic Uncertainties

Each data point has a systematic uncertainty in ϑ, which arises from the spatial extension of each pixel.

For each data point two different types of uncertainties have to be calculated, a statistic and a systematic contribution. The statistic uncertainty depends on the uncertainty of the number of counts in a pixel and the uncertainty of the efficiency correction that is the statistic uncertainty of the Monte-Carlo simulation used to determine it.

Contributions to the systematic uncertainty are the uncertainties of the γ-ray efficiency, beam purity, and luminosity, which are all independent of ϑ. The uncertainties of the solid angle covered by each pixel and the conversion of this solid angle into the center of mass frame are ϑ dependent contributions. The uncertainty of the covered solid angle stems from the uncertainty in the position of the target (see subsection 4.3.1) which influences the z-coordinates of the barrel detectors. The uncertainty in the conversion of the solid angle to the center of mass frame is estimated by the change of the conversion factor across each pixel.

Chapter 5

Results

In this chapter the results of the d (^{30}Mg, p) ^{31}Mg one neutron transfer reaction are presented. The goal of the experiment was the determination of the orbital angular momenta of excited states in ^{31}Mg. In the first section results from the d (^{22}Ne, p) ^{23}Ne test measurement are shown, while the second section focuses on the results of the d (^{30}Mg, p) ^{31}Mg reaction.

The d (^{22}Ne, p) ^{23}Ne experiment has been used to develop, test, and verify all steps of the analysis.

5.1 ^{22}Ne Test Experiment

The d (^{22}Ne, p) ^{23}Ne reaction was performed both to calibrate the position of the MINIBALL detectors (subsection 4.3.3) and to have a reference data set with high(er) statistics to test the analysis. ^{22}Ne is used as a buffer gas in the REX-TRAP and therefore also ever-present in the REX-EBIS, which makes it an easily available stable beam for testing and calibration purposes.

5.1.1 Levels, γ-rays, and Excitation Energies

Figure 5.1 shows the level scheme of ^{23}Ne with the relevant levels and γ-ray transitions highlighted [NND]. Looking at the Doppler corrected γ-rays detected in coincidence

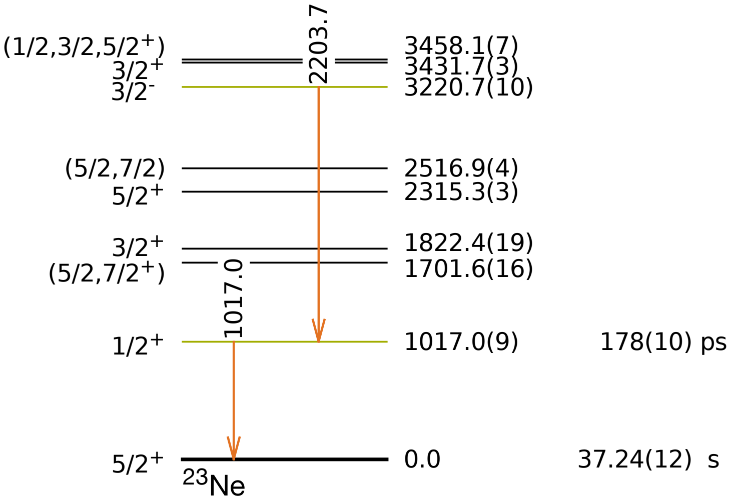

Figure 5.1: Level scheme of ^{23}Ne. Highlighted are the two most strongly populated levels (green) and their γ-rays (orange). For the ground state and the first excited state the known lifetimes are given on the right, all other states have lifetimes below 70 fs.

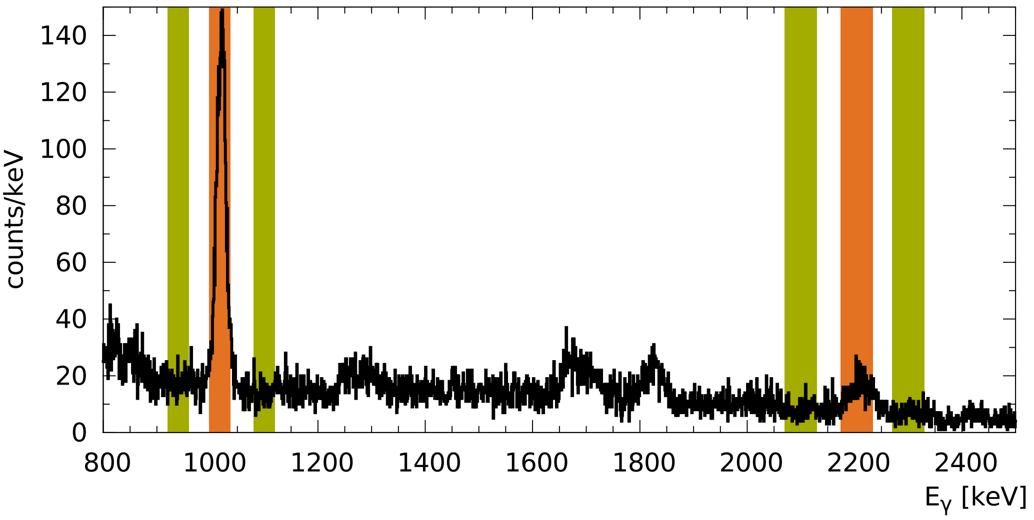

Figure 5.2: Doppler corrected γ-ray spectrum in coincidence with protons from the ^{22}Ne reaction. Highlighted are the two γ-lines at 1016.95(9) keV and 2203.58(5) keV (orange) that depopulate the states at 1016.95(9) keV and 3220.66(10) keV, respectively. The background cuts are indicated in green.

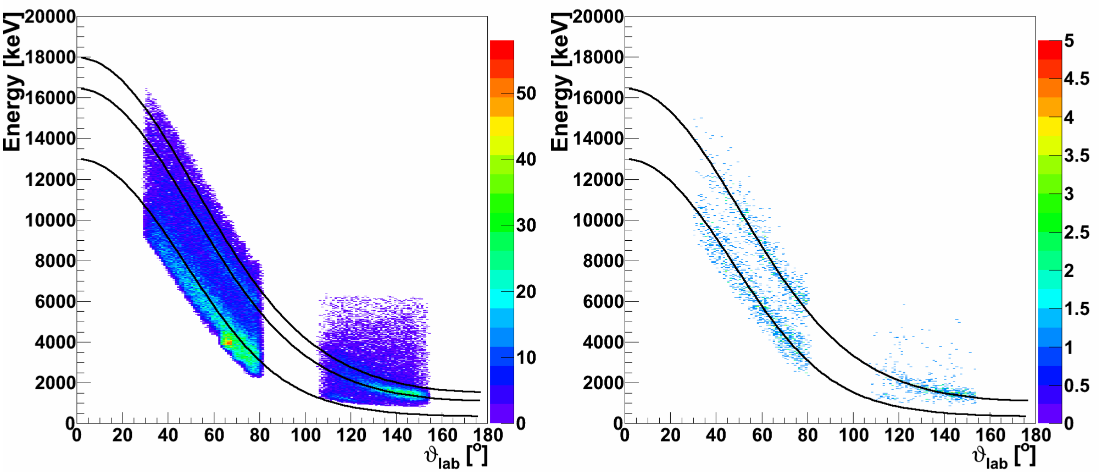

Figure 5.3: The left panel shows the energy versus ϑ_{lab} spectrum for all protons from the d(^{22}Ne, p)^{23}Ne reaction. The energy loss of the protons in the target and the foils was reconstructed. The lines indicate the expected energy versus ϑ_{lab} relation for the ground state and the states at 1017 keV and 3221 keV. On the right the same is shown for protons in coincidence with γ-rays at 1017 keV.

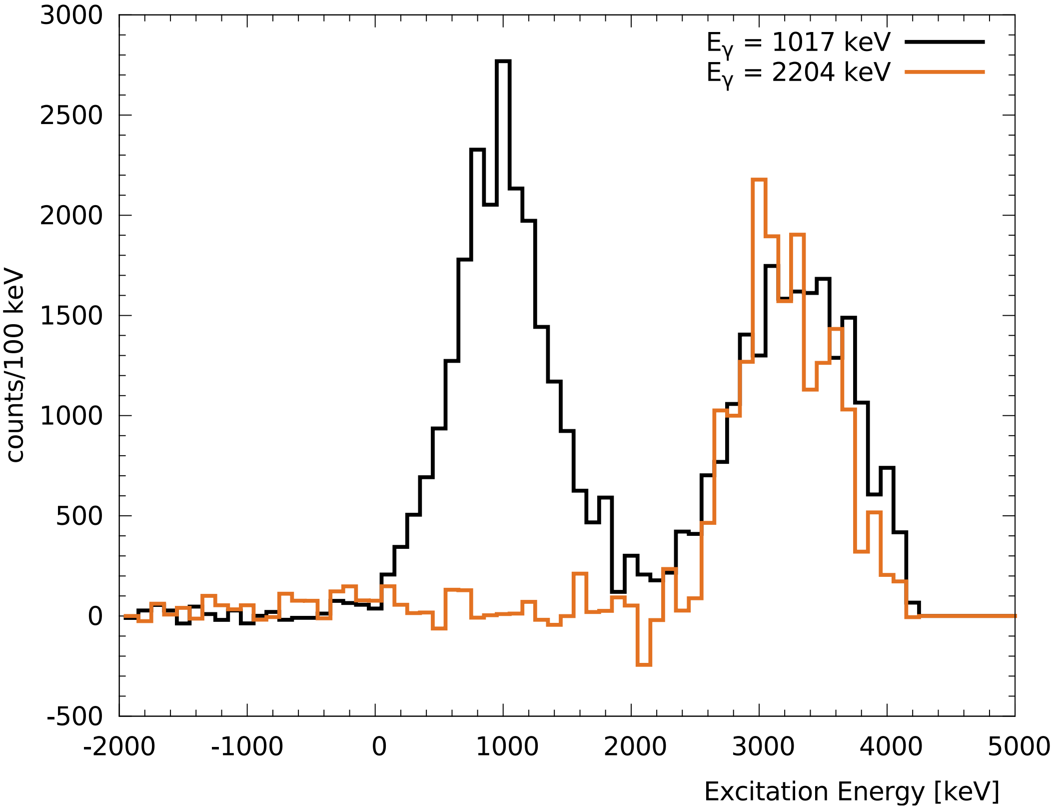

Figure 5.4: Background subtracted excitation energy spectrum for protons from the d (^{22}Ne, p) ^{23}Ne reaction with cuts on the 1017 keV (black) and the 2204 keV (orange) γ-ray. The spectra are corrected for the γ-efficiency and the branching, showing that most of the strength at 3.3 MeV stems from the 3221 keV state.

with protons in figure 5.2 one can see the strong de-excitation of the 1017 keV state to the ground state and the de-excitation of the 3221 keV state to the 1017 keV state by a 2204 keV γ-ray.

The left panel of figure 5.3 shows the energy versus ϑ_{lab} spectrum for all identified protons. The bands corresponding to the population of the ground state, the 1017 keV state, and states at $\approx$ 3.3 MeV can be seen. Cutting on the 1017 keV γ-rays, one obtains the much cleaner energy versus ϑ_{lab} spectrum shown on the right of figure 5.3. Here one can see the bands of protons from the population of the state with 1017 keV as well as from protons from the population of higher lying states that feed into this state.

One of the states that feed into the 1017 keV state is the 3221 keV state that feeds into the aforementioned state via a 2204 keV γ-ray transition. Figure 5.4 shows the excitation energy, corrected for the γ-ray detection efficiency of MINIBALL and the branching ratios, for cuts on the 1017 keV (black) and 2204 keV (orange) γ-rays. The ratio between the peaks at 3.3 MeV excitation energy is $87(2)$ %, indicating that most of the feeding into the 1017 keV state is via the 2204 keV γ-ray. One can however see that the centroid of the peak at 3.3 MeV is slightly shifted to higher energies for the cut on the 1017 keV γ-rays, i.e. there are other states that feed the 1017 keV state and are at higher excitation energies than the 3221 keV state (see also figure 5.1).

		[Loh74]	*[Per76]*	*[Boj88]*	*fitted*
real	V [MeV]	98.9814	86.9821	85.1629	
	r_V [fm]	1.05	1.15	1.18	0.99(3)
	a_V [fm]	0.86	0.81	0.7341	0.87(2)
imag.	W [MeV]	27.7657	15.6606	10.7141	
	r_W [fm]	1.43	1.34	1.27	1.417(12)
	a_W [fm]	0.6021	0.68	0.8268	
luminosity [mb^{-1}]		1328(5)	1709(9)	1529(7)	1357(20)

Table 5.1: Global ([Loh74], [Per76], and [Boj88]) and fitted optical model parameters for the d (^{22}Ne, d) ^{22}Ne reaction. The same fitted parameters were obtained for all three global parameters sets as starting values and the depths V and W fixed to the respective global values.

		[Per76]	*[Kon03]*	*fitted*
real	V [MeV]	55.4751	58.2865	
	r_V [fm]	1.25	1.1592	1.287(9)
	a_V [fm]	0.65	0.6745	0.57(2)
imag.	W [MeV]	13.5	6.42	
	r_W [fm]	1.25	1.298	0.79(3)
	a_W [fm]	0.47	0.541	
luminosity [mb^{-1}]		114.2(7)	109.5(7)	88(9)

Table 5.2: Global ([Per76] and [Kon03]) and fitted optical model parameters for the p (^{22}Ne, p) ^{22}Ne reaction. The same fitted parameters were obtained for all three global parameters sets as starting values with the depths V and W fixed to the respective global values.

5.1.2 Elastic Scattering Data

In chapter 2 the need for optical model parameters for both the ingoing and outgoing channels was discussed.

In the literature one can find a number of global optical model parameter scaling relations [Loh74, Per76, Boj88, Kon03] for neutrons, protons, and deuterons. Most of these were obtained from stable beam experiments at energies above 10 MeV whereas the ISOLDE beam energy of 2.85 MeV u^{-1} corresponds to a deuteron energy of 5.7 MeV in normal kinematics. The scaling relations for some parameters contain also a proton-neutron asymmetry dependence, which can be large for neutron rich isotopes.

Despite these problems there are some arguments for using a global parameter set instead of parameters fitted to elastic scattering data [Tho09]. In this work, in addition to the global parameter sets, new parameter sets were determined from the elastic scattering of the beam on protons and deuterons.

Figure 5.5a shows the angular distribution of elastically scattered deuterons compared to three different DWBA calculations, each based on a different global optical potential parameter set and scaled to best reproduce the angular distribution observed experimentally. All DWBA calculations in this work were performed for the effective beam energies at the center of the target. The different global parameter sets result in angular distributions that differ dramatically from the observed angular

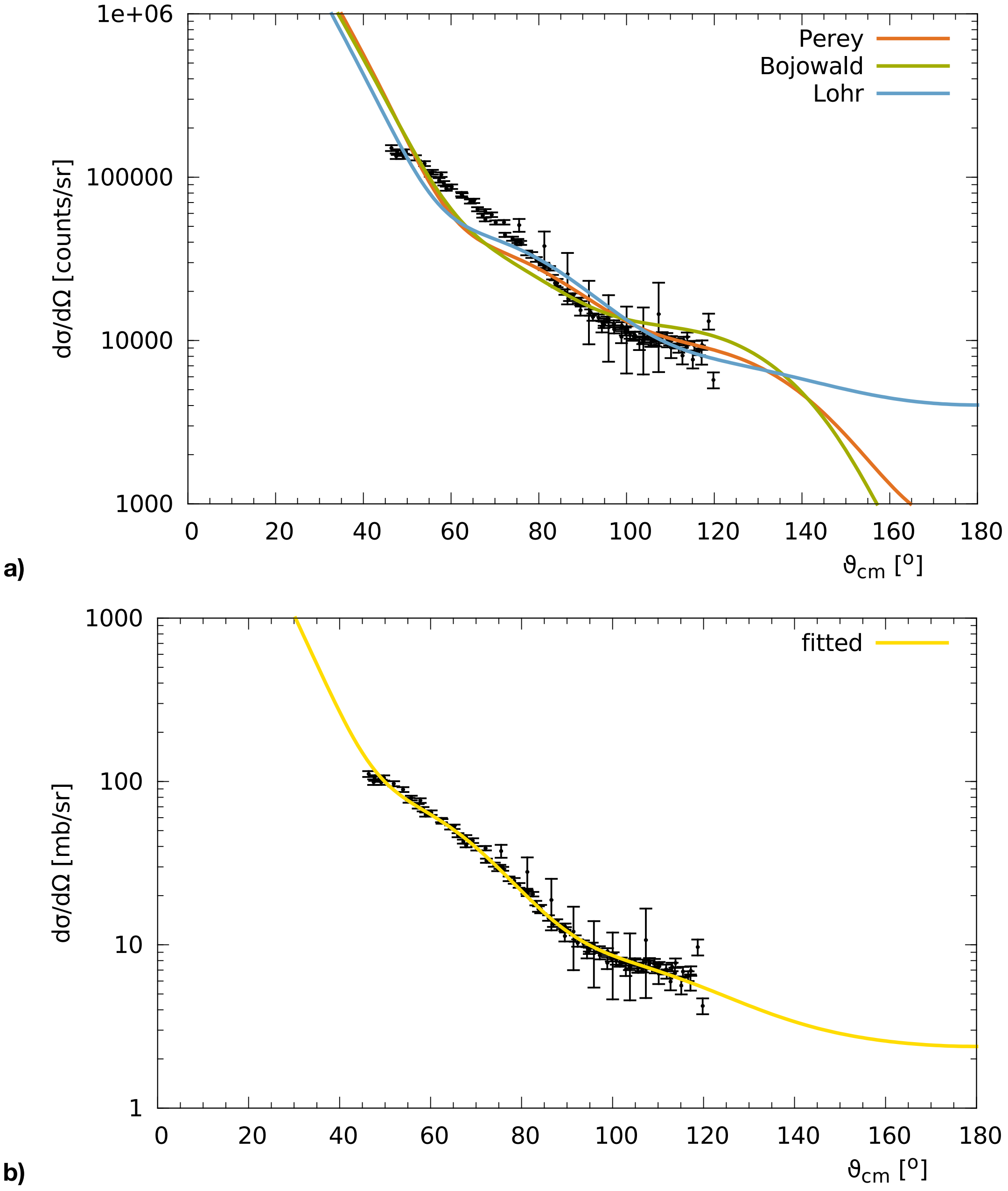

Figure 5.5: a) shows the angular distribution of elastically scattered deuterons from the d (^{22}Ne, d) ^{22}Ne reaction with DWBA calculations for three different global optical parameter sets taken from [Loh74, Per76, Boj88] and scaled to match the experimental data. b) shows the same data scaled with the luminosity and a DWBA calculation with optical parameters that were fitted to reproduce the observed angular distribution.

potential	1017 keV $S\Delta L = 0$	3221 keV $S\Delta L = 1$	$S_{3221\,\text{keV}}/S_{1017\,\text{keV}}$ S_{rel}
[Per76]	0.56(2)	0.111(8)	0.198(16)
[Kon03] & [Loh74]	0.91(3)	0.172(12)	0.189(15)
[Kon03] & [Boj88]	0.72(3)	0.162(12)	0.225(19)
fitted parameters	$0.73(2)^{+0.01}_{-0.01}$	$0.49(2)^{+0.04}_{-0.04}$	$0.67(3)^{+0.01}_{-0.01}$

Table 5.3: Cross section scaling factors for the d (^{22}Ne, p) ^{23}Ne reaction. The uncertainties given are the error of the data (i), the systematical uncertainty from the determination of the luminosity (ii) being about a factor ten smaller. For the fitted parameters the uncertainty derived from the uncertainties in the fitted parameters (iii) is given as well.

distribution and the luminosity yielded from them differs for the different parameter sets by almost 15 % (see table 5.1).

Using the SFRESCO program [Tho06] it is possible to fit the parameters of the proton and deuteron potentials to the observed angular distributions. Fitting the optical parameters to the elastic scattering data requires some caution because multiple χ^2 minima exist. Fitting all parameters at once results in physically unsound depths of the real and imaginary potentials (about 170 MeV and 7 MeV, respectively) and the diffuseness of the imaginary part becomes zero. Alternatively only the radii of both parts and the diffuseness of the real part were fitted with each of the three global parameter sets as starting values. The fit results in the same radii (r_V, r_W) and same diffuseness (a_V) for all three global sets using fixed depths and imaginary diffuseness, i.e. it does not depend strongly on the values of V, W and a_W. The resulting angular distribution is shown in figure 5.5b and the parameters are given in table 5.1. The description of the observed angular distribution is much better for the fitted optical potential, improving the red. χ^2 by more than a factor of 10.

Since the deuterated polyethylene target contains protons as well as deuterons the same comparison of calculations with global parameter sets as described above can be made for elastically scattered protons. The global parameter sets were taken from [Per76] and [Kon03], given in table 5.2 together with the fitted parameters. The results can be used not just for the core-core interaction, but also for the outgoing ^{23}Ne$+p$ channel since the difference of one neutron should have only negligible effects on the parameters.

The fitting of the optical model parameters to the elastically scattered deuterons and protons thus allows to adjust the optical potentials of the in- and outgoing channels as well as the core-core interaction, while the neutron binding potentials for the target and ejectile are taken from the global parameter sets Perey & Perey [Per76] or Koning *et al.* [Kon03].

5.1.3 Transfer to the 1017 keV and 3221 keV States

The angular distribution of protons in coincidence with 1017 keV γ-rays is shown in figure 5.6, together with the $\Delta L = 0$ DWBA calculations. Figure 5.7 shows the angular distribution of protons in coincidence with 2204 keV γ-rays that are emitted in reactions populating the 3221 keV state compared to $\Delta L = 1$ DWBA calculations. The resulting cross section scaling factors for the global parameter sets and the fitted parameters are listed in table 5.3. Three uncertainties play a role for the cross section

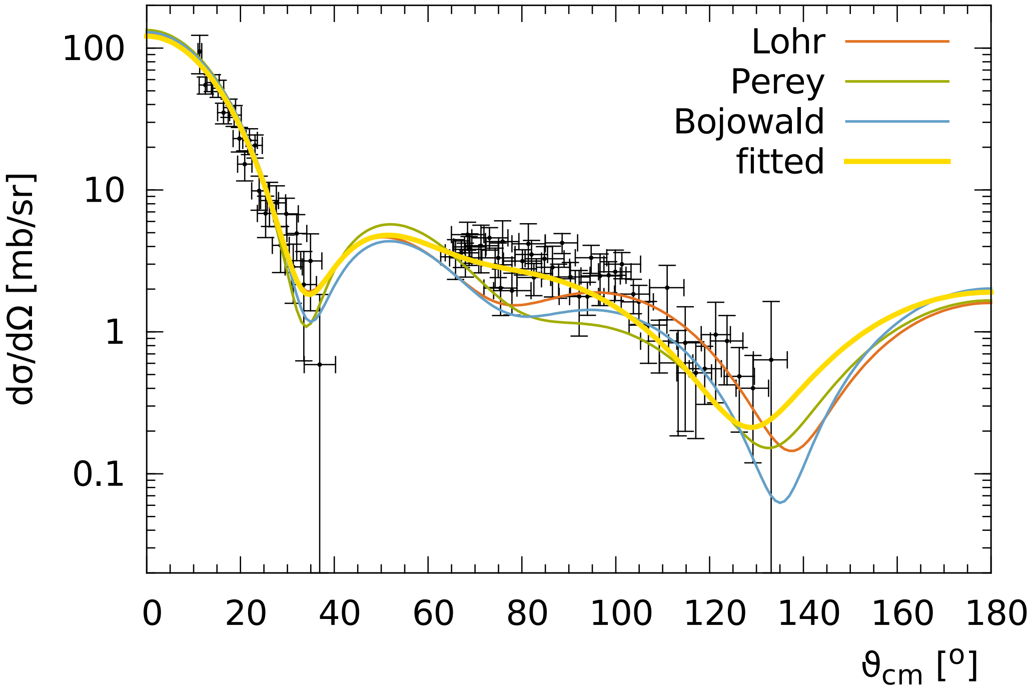

Figure 5.6: Angular distribution of protons from the 1017 keV state populated in the d (^{22}Ne, p) ^{23}Ne reaction. Shown is the data scaled with the luminosity obtained from the elastic scattered deuterons and the fitted optical potential. The calculations were done with parameters from the three global sets and the fitted parameters.

scaling factors:

(i) the error of the fit of the DWBA cross section to the data via the cross section scaling factor, i.e. the uncertainties in the data, see also chapter 4,

(ii) the systematical uncertainty from the determination of the luminosity, and

(iii) the systematical uncertainty from the fitted parameters.

The uncertainties in the data (i) are discussed in chapter 4 and are relatively small, while the uncertainty in the determination of the luminosity (ii) is about a factor ten smaller than these, due to the higher statistics of the elastic scattering data. The uncertainty in the fitted parameters (iii) is also smaller than (i) and accounted for by varying each fitted parameter within the range resulting from the fit of the parameters and adjusting the other parameters according to the corresponding covariance matrix. With the two additional parameter sets obtained for each fitted parameter the same fitting of the cross section scaling factor is repeated. From these cross section scaling factors the minimal and maximal possible factors are determined that are reported in table 5.3.

5.1.4 Discussion

The cross section scaling factors for the 1017 keV and 3221 keV state determined in this work and others are shown in table 5.4.

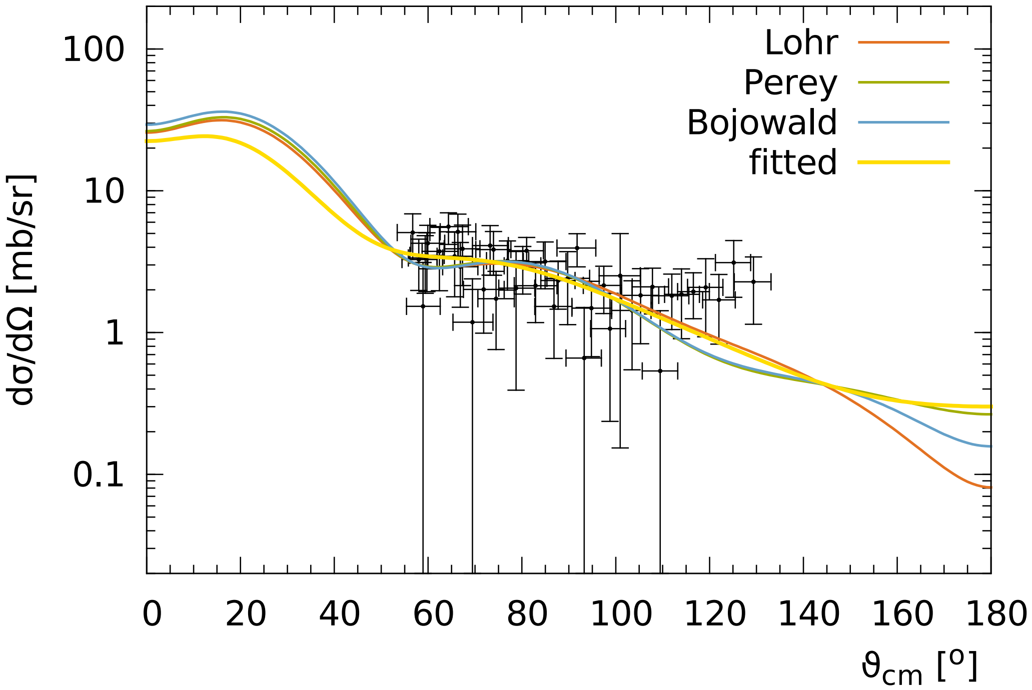

Figure 5.7: Angular distribution of protons from the population of the 3221 keV state in the d (^{22}Ne, p) ^{23}Ne reaction. Shown is the data scaled with the luminosity obtained from the elastically scattered deuterons and the fitted optical potential. The calculations were done with parameters from the three global sets and the fitted parameters.

deuteron energy	*1017 keV state*	*3221 keV state*	*reference*
2.5 MeV		0.34	[Cha69]
3.0 MeV		0.34	[Cha69]
4.81 MeV	0.60		[Nan69]
5.7 MeV	0.70(2)	0.16(4)	this work
5.82 MeV	0.55		[Nan69]
12.1 MeV		0.34	[Cha69]
12.1 MeV	0.40(2)	0.81(11)	[Lut67]
16.4 MeV	0.70	0.3	[How70]

Table 5.4: Cross section scaling factors for the d (^{22}Ne, p) ^{23}Ne reaction.

For both states the cross section scaling factors obtained with T-REX agree reasonably well with the other values at various deuteron energies ranging from 2.5 MeV to 16.4 MeV. The only exception is the work of Lutz *et al.* [Lut67] where the reported factor for the 1017 keV state is lower and for the 3221 keV state higher. However the fit of the 1017 keV state in that work is at very forward angles, underestimating the cross section at larger angles. For the 3221 keV state a $\Delta L = 0$ transfer reaction to a $J^{\pi} = 1/2^{+}$ state was assumed which doesn't reproduce the observed data as good as the $J^{\pi} = 3/2^{-}$ assumed in this work and the other works shown in table 5.4.

5.2 d (^{30}Mg, p) ^{31}Mg

During the first experiment in 2007 the beam intensity was more than a factor ten lower than expected, limiting the statistics obtained quite severely. It was possible to take more data in 2008 together with the t (^{30}Mg, p) ^{32}Mg experiment, which yielded within 25 h the same statistics as the 10 d experiment in 2007. In this section the results of the 2008 experiment are presented as this data set contains less background from β decay of beam particles stopped in the chamber.

The analysis of the d (^{30}Mg, p) ^{31}Mg data is very similar to that of the d (^{22}Ne, p) ^{23}Ne data. However the ^{30}Mg beam is not pure so first the beam composition has to be determined.

5.2.1 Beam Composition

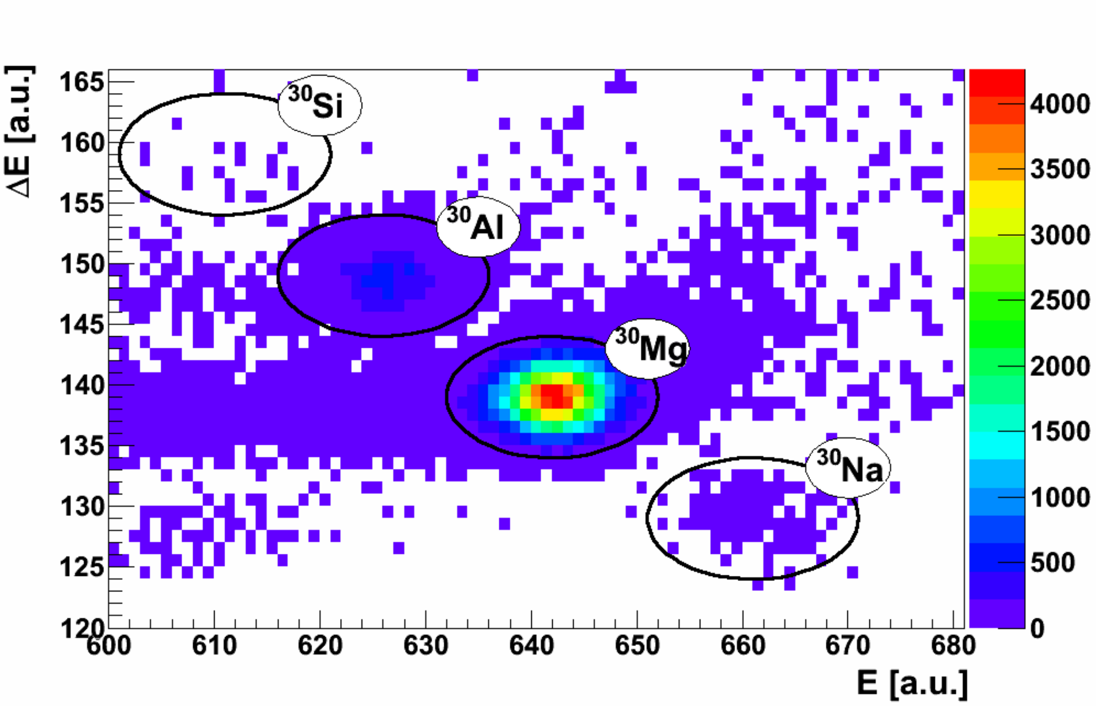

Figure 5.8: Identification of beam contaminants in the Bragg chamber. Shown is the maximum slope of the energy deposition in the chamber versus the total energy deposited. Clearly visible besides the main beam components ^{30}Mg and ^{30}Al are the small contributions from ^{30}Na and ^{30}Si.

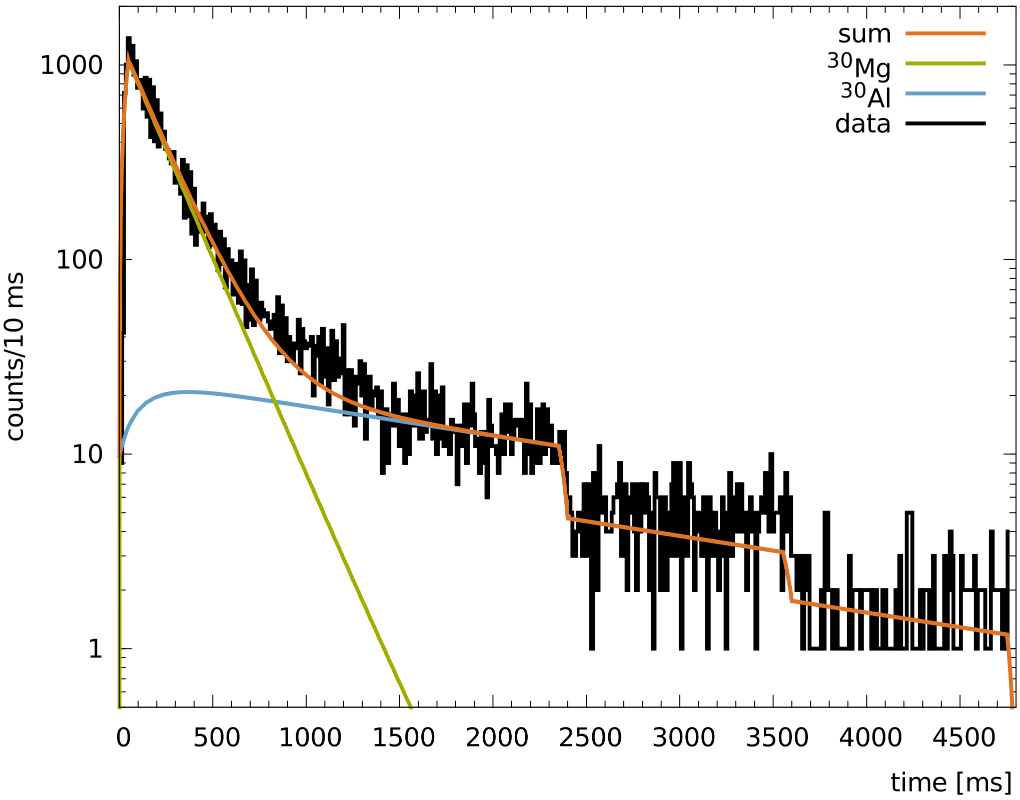

Figure 5.9: Release curve of the ^{30}Mg beam. Plotted is the time difference between any particle with an energy above 9 MeV (which excludes any electrons from β-decay) and the proton pulse. The characteristic release curve and distinct lifetimes of ^{30}Mg and ^{30}Al, allow the disentanglement of these two major beam components.

The production method used at REX-ISOLDE to produce radioactive ion beams allows for three sources of beam contamination:

(i) direct isobaric contamination from the ISOLDE target as the general purpose mass separator of ISOLDE is not able to separate all isobars,

(ii) isobaric contamination from β-decay of the radioactive beam during the capturing in the REX-trap and the charge breeding in the EBIS, and

(iii) stable contaminants from the residual gas in the EBIS if their mass to charge ratio allows them to pass the mass separator of REX.

Two methods were used to check the beam contamination of the ^{30}Mg beam.

The first is a Bragg chamber [Wei06], which was mounted at the end of the beam line, about 4 m behind the target. Figure 5.8 shows the maximum slope of the energy deposition in the chamber versus the total energy deposited in the chamber. The maximum slope of the energy deposition depends on the charge Z of the isotope, while the total energy should be constant for isobars. Since the Bragg chamber was operated behind the target (which was a 0.5 mg cm^{-2} tritium loaded titanium foil) and has an entrance window of 2 µm Mylar foil, the total energy has an inverse

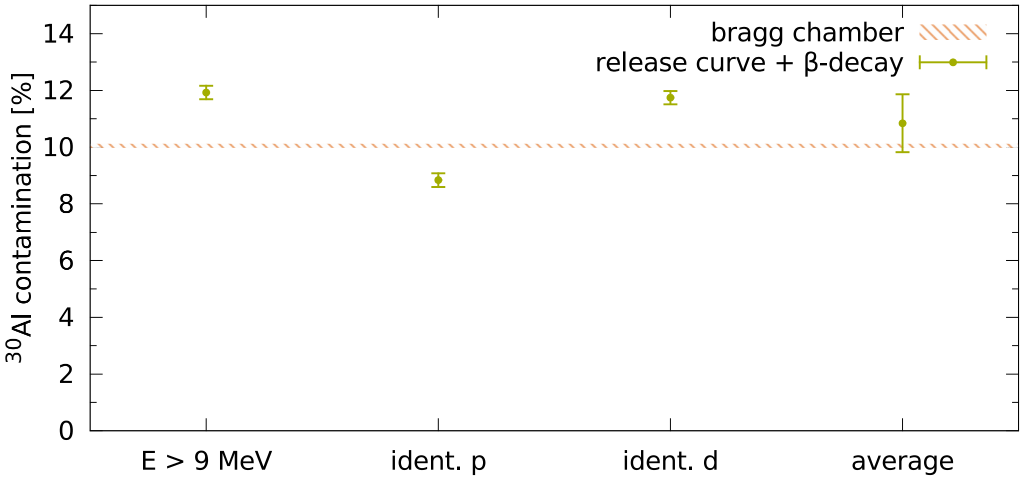

Figure 5.10: Comparison of the results from the analysis of the release curves and the Bragg chamber. The analysis of the release curves yields the beam contamination from the ISOLDE target, the effect of β-decay in the traps has to be added. All data with a cut on events less than 1.2 s after the proton pulse.

dependence on the charge Z. The main beam components visible in figure 5.8 are besides the ^{30}Mg (89.2(10) %):

- 0.280(12) % ^{30}Na, which can come directly from ISOLDE,
- 10.05(7) % ^{30}Al, which can come both directly from ISOLDE and from β-decay of ^{30}Mg and ^{30}Na, and
- 0.037(5) % ^{30}Si, which can come only from the β-decay of ^{30}Na, ^{30}Mg, and ^{30}Al.

The Bragg chamber was not operating for the whole experiment and thus provides just a snap-shot of the beam contamination which can be used to cross check the second method used to determine the beam contamination.

The second method used to determine the beam contamination is the study of the release curve of the beam. The release curve shows the intensity of the beam in relation to the time after the proton pulse impact on the ISOLDE target. Due to different release times of the various chemical elements from the target an analysis of the release curve can be used to extract the beam purity. As the intensity of a contamination that stems from the β-decay has the same time dependency as the parent nucleus this contribution is not accounted for in this method.

Figure 5.9 shows this relation as the number of detected particles with energies above 9 MeV (to suppress the constant background of electrons from β-decay) versus the time after the proton pulse. The steps in the intensity are caused by the fact that the proton pulses hit the ISOLDE target at intervals of multiples of 1.2 s.

There are two components visible in the spectrum of figure 5.9, one with a fast ($\approx$ 130 ms) and one with a slow ($\approx$ 2 s) decay, attributed to the two main beam components ^{30}Mg ($t_{1/2}$ = 335(17) ms) and ^{30}Al ($t_{1/2}$ = 3.60(16) s). The

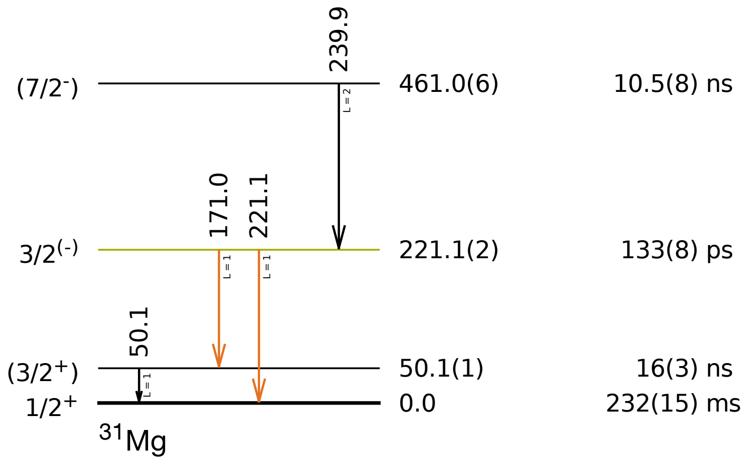

Figure 5.11: Partial level scheme of ^{31}Mg, highlighted are the level at 221 keV (green) and its γ-rays (orange). The lifetimes of the states are given on the right [NND].

determined release time is $(\lambda_f(^{30}\mathrm{Mg}) \cdot \ln 2)^{-1} = 132.5(13)$ ms, while the half-life of ^{30}Mg (335(17) ms) folded with the release time of stable magnesium (190 ms) [Kös03] gives 121(2) ms, which is a good agreement considering the different conditions during the measurements.

The analysis of the release curve was done not just for particles with energies above 9 MeV but also for all identified protons or deuterons. Since all ^{30}Mg is released within the first 1.2 s after the proton pulse hits the ISOLDE target, all further analysis could be restricted to events in the first 1.2 s, reducing the background from ^{30}Al. The different percentages of ^{30}Al, determined by the analysis of the release curves and their average value, are compared in figure 5.10 with the results from the Bragg chamber, giving a beam contamination of 10.8(10) %.

5.2.2 Levels and γ-rays

The partial level scheme of ^{31}Mg is shown in figure 5.11. The spectrum of the Doppler corrected γ-rays in coincidence with protons (figure 5.12) shows mainly the 171 keV and 221 keV de-excitations of the 221 keV state. Even though for each 171 keV γ-ray a coincident 50 keV γ-ray is emitted (internal conversion is neglectable), the number of detected 50 keV γ-rays is much smaller than the number of detected 171 keV γ-rays. This is mostly due to the long lifetime of the 50 keV state, during 16 ns a particle at 5 % speed of light travels about 24 cm so that the de-excitation of the ^{31}Mg occurs outside the MINIBALL array.

5.2.3 Elastic Scattering Data

The deuterons are not only scattered by the ^{30}Mg but also by the 10.8(10) % ^{30}Al in the beam (the ^{30}Na and ^{30}Si contributions are negligible). Therefore the DWBA calculations with global parameter sets were done for both ^{30}Mg and ^{30}Al, scaled with their respective contribution to the beam composition. The sum of the two resulting angular distributions is then scaled to the data as shown in figure 5.13a.

As for the ^{22}Ne, the resulting calculated angular distributions have a different shape than the observed data and the luminosities determined differ by about 10 %. Therefore the optical potentials were fitted to the elastic scattering data as it was done for the d(^{22}Ne, d)^{22}Ne and p(^{22}Ne, p)^{22}Ne (only r_V, a_V, and a_W). Since the

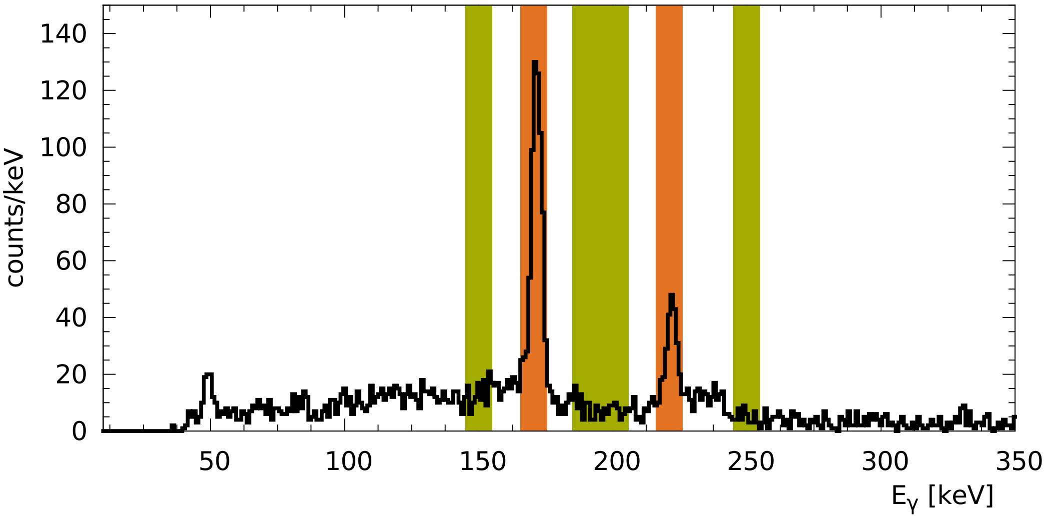

Figure 5.12: γ-ray spectrum in coincidence with protons from the d (^{30}Mg, p) ^{31}Mg reaction. Highlighted are the two γ-lines at 171.0 keV and 221.1 keV (orange) that depopulate the state at 221.1 keV. The background cuts are indicated in green, with two of them touching at 195 keV. The line at 50.1 keV is visible as well, but due to the long lifetime of the 50.1 keV state (16(3) ns) the statistics are too low to produce an angular distribution in coincidence with it.

		[Loh74]	*[Per76]*	*[Boj88]*	*fitted*
	V [MeV]	99.6263	87.5657	85.5791	87.5657
real	r_V [fm]	1.05	1.15	1.18	0.68(3)
	a_V [fm]	0.86	0.81	0.7448	1.05(3)
	W [MeV]	22.5792	15.6635	11.0315	15.6635
imag.	r_W [fm]	1.43	1.34	1.27	1.156(12)
	a_W [fm]	0.6255	0.68	0.8333	0.68
luminosity [mb^{-1}]		358(2)	415(2)	381(2)	529(12)

Table 5.5: Global ([Loh74], [Per76] and [Boj88]) and fitted optical model parameters for the d (^{30}Mg, d) ^{30}Mg reaction.

		[Per76]	*[Kon03]*	*fitted*
	V [MeV]	58.2071	60.6074	58.2071
real	r_V [fm]	1.25	1.1734	1.167(3)
	a_V [fm]	0.65	0.6733	0.675(10)
	W [MeV]	13.5	7.0041	13.5
imag.	r_W [fm]	1.25	1.2932	1.04(7)
	a_W [fm]	0.47	0.5396	0.47
luminosity [mb^{-1}]		39.9(3)	38.0(3)	42.0(5)

Table 5.6: Global ([Per76] and [Kon03]) and fitted optical model parameters for the p (^{30}Mg, p) ^{30}Mg reaction.

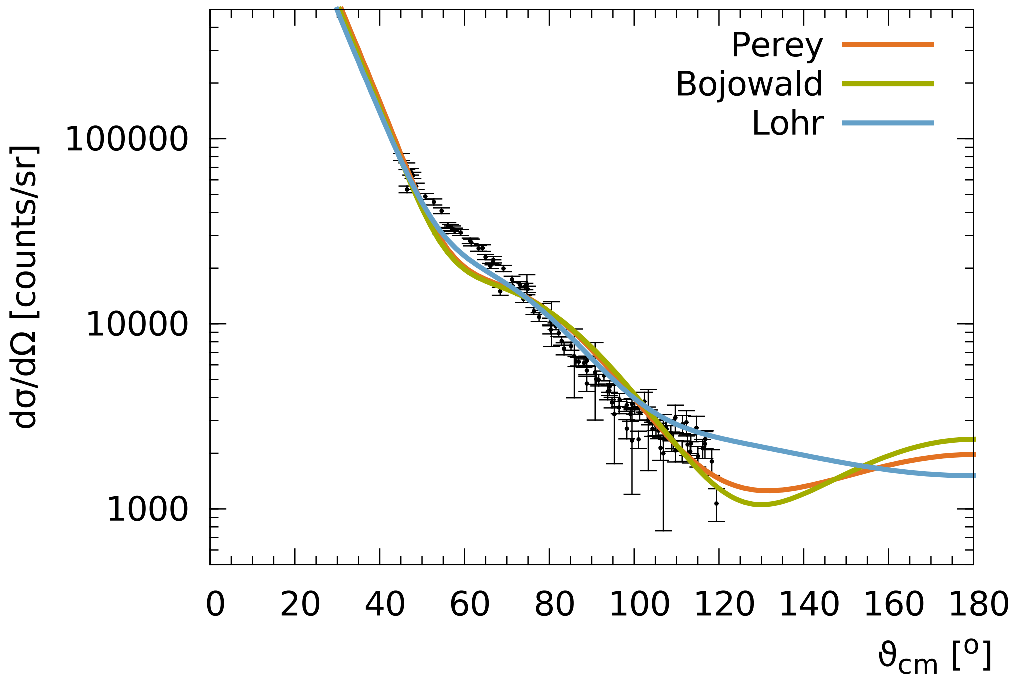

a)

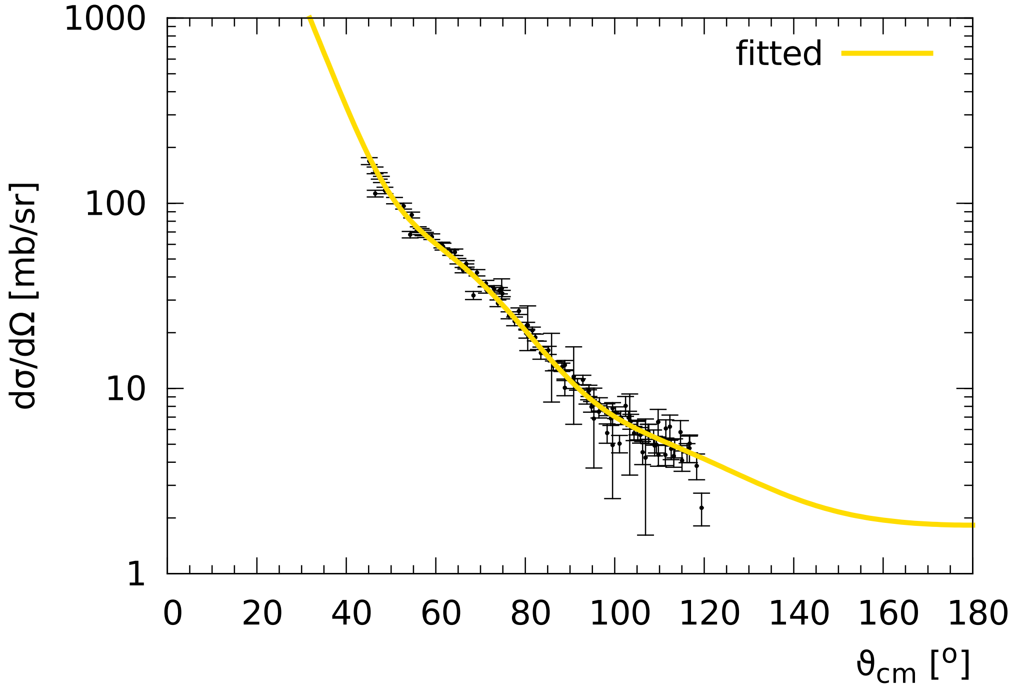

b)

Figure 5.13: a) shows the angular distribution of elastically scattered deuterons from the d (^{30}Mg, d) ^{30}Mg reaction compared to DWBA calculations for three different global optical parameter sets taken from [Loh74, Per76, Boj88] and scaled to match the experimental data. b) shows the same data with optical parameters that were fitted to reproduce the observed angular distribution.

		[Per76]	*[Kon03] & [Loh74]*	*[Kon03] & [Boj88]*	*fitted parameters*
$S\Delta L = 0$	S	0.123(6)	0.186(8)	0.145(7)	0.134(6)
	red. χ^2	2.56	1.18	3.02	1.25
$S\Delta L = 1$	S	0.0401(18)	0.066(3)	0.0411(19)	0.084(4)
	red. χ^2	1.06	0.97	1.10	1.36
$S\Delta L = 2$	S	0.139(6)	0.231(11)	0.164(8)	0.221(11)
	red. χ^2	2.77	2.66	3.22	3.59
$S\Delta L = 3$	S	0.081(4)	0.147(7)	0.091(5)	0.227(10)
	red. χ^2	2.79	3.52	4.13	2.03

Table 5.7: Cross section scaling factors and reduced χ^2 values of fit for the 221 keV state in ^{31}Mg. The uncertainties given are, as for the d (^{22}Ne, p) ^{23}Ne reaction, the error of the data, the systematical uncertainty from the determination of the luminosity being about a factor ten smaller. For the fitted parameters the uncertainty derived from the uncertainties in the fitted parameters is neglectable as well. For all optical model parameters set the $\Delta L = 1$ calculation gives the best agreement with the observed angular distribution of the 221 keV state in ^{31}Mg.

resulting values of r_V, a_V, and r_W depend in this case on the other (fixed) values, the global parameter set given in [Per76] was used for the latter, see also table 5.5.

For the fitted parameters it is not possible to separate the ^{30}Mg and ^{30}Al contributions, i.e. the obtained scaling factor has to be multiplied by the contribution of ^{30}Mg to the beam (0.892(10)) to obtain the ^{30}Mg luminosity.

The results of the analysis of the p (^{30}Mg, p) ^{30}Mg data are shown in table 5.6 and for the neutron binding potentials of the target and ejectile the global parameter sets Perey & Perey [Per76] and Koning *et al.* [Kon03] were used.

The ^{30}Al in the beam causes no background in the angular distributions of protons from transfer reactions as the kinematics of protons from the d (^{30}Al, p) ^{31}Al reaction is very different from those of the d (^{30}Mg, p) ^{31}Mg reaction, because the Q-value is much larger (almost 5 MeV compared to 154(15) keV).

5.2.4 Transfer to the 221 keV State

From lifetime measurements and Weisskopf estimates [Klo93] the γ-ray transitions from the 221 keV second excited state to the 50 keV first excited state and the ground state were determined to be dipole transitions which, together with the ground state spin $1/2^+$, limits the spin to $1/2, 3/2$. The spin assignment of $j = 3/2$ for the 221 keV state is from a proton knockout experiment [Mil09] where the difference between the number of 170 keV and 221 keV γ-rays in the forward and backward rings of the SeGA Germanium detector array were compared to the expected angular distributions for dipole transitions.

The direct measurement of the orbital angular momentum of the 221 keV state in ^{31}Mg was the main goal of the d (^{30}Mg, p) ^{31}Mg experiment. To this end the observed angular distribution was compared to different DWBA calculations assuming a $2s1/2^+$, $2p3/2^-$, $1d3/2^+$, and $1f7/2^-$ configuration for each of the three global parameter sets and the fitted parameter set. The cross section scaling factors and goodness of fit is reported in table 5.7.

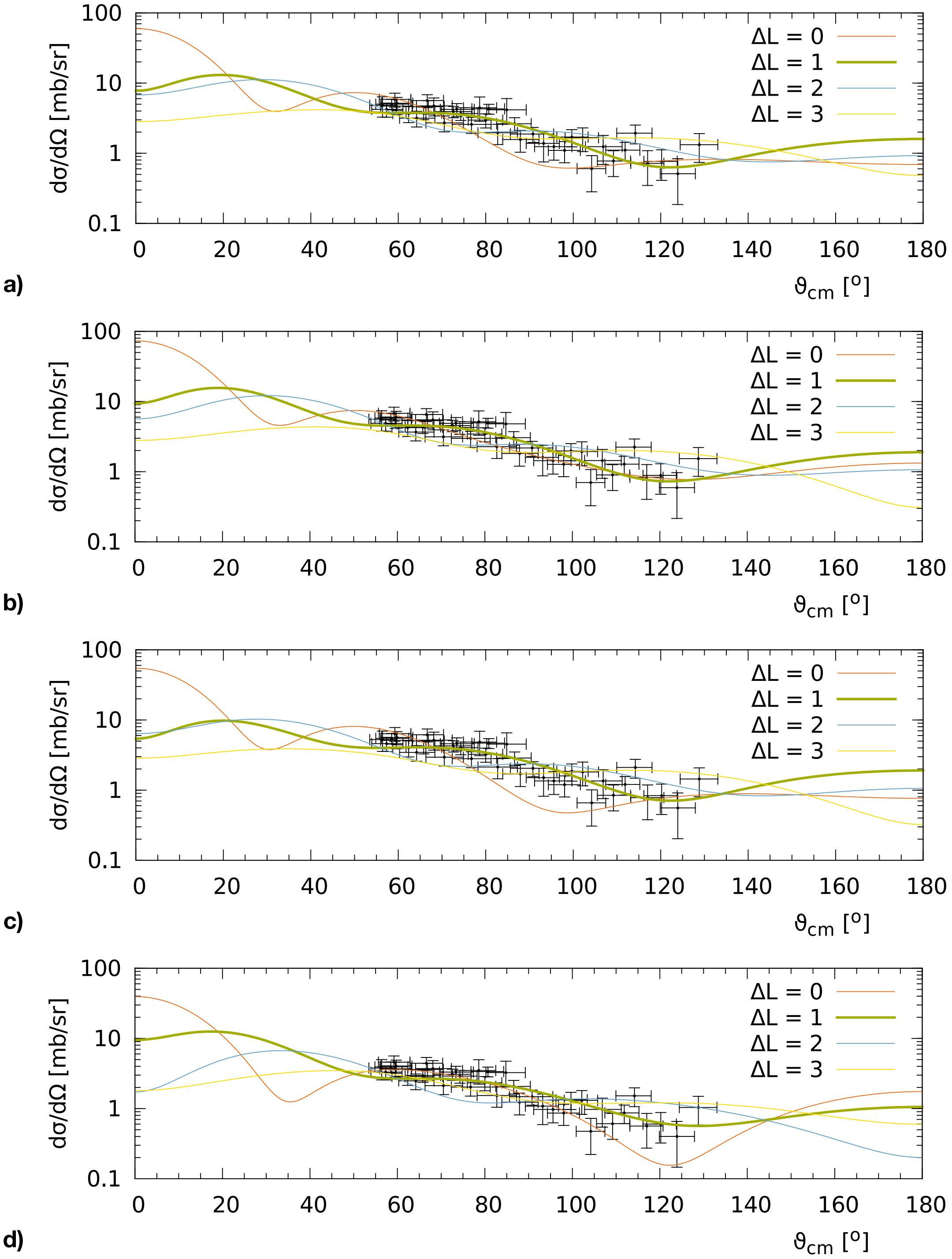

Figure 5.14: Angular distribution of protons from the population of the 221 keV state in ^{31}Mg. Each panel shows the same data set, scaled with the respective luminosities determined from the d(^{30}Mg, d)^{30}Mg data. The data is compared to $\Delta L = 0$ (orange), $\Delta L = 1$ (green), $\Delta L = 2$ (blue), and $\Delta L = 3$ (yellow) DWBA calculations for the global parameter sets taken from [Per76] (a), [Kon03] and [Loh74] (b), [Kon03] and [Boj88] (c), and fitted parameters (d). For all optical parameter sets the $\Delta L = 1$ calculation shows the best agreement with the observed angular distribution of the 221 keV state in ^{31}Mg.

	[Per76]	*[Kon03] & [Loh74]*	*[Kon03] & [Boj88]*	*fitted parameters*
a) free fit of all transfer protons				
$S_{\Delta L=0}$	0.111(9)	0.27(2)	0.144(10)	0.312(18)
$S_{\Delta L=1}$	0.084(4)	0.096(10)	0.087(5)	0.046(16)
$S_{\Delta L=2}$	0.124(14)	0.21(2)	0.142(17)	0.32(2)
$S_{\Delta L=1}/S_{\Delta L=0}$	0.76(2)	0.36(5)	0.60(5)	0.15(5)
$S_{\Delta L=1}/S_{\Delta L=2}$	0.68(8)	0.46(6)	0.61(8)	0.14(5)
$S_{\Delta L=2}/S_{\Delta L=0}$	1.12(16)	0.78(9)	0.99(14)	1.00(8)
b) fit of all transfer protons with $S_{\Delta L=1}$ fixed				
$S_{\Delta L=0}$	0.160(8)	0.326(15)	0.206(8)	0.272(7)
$S_{\Delta L=1}$ (fixed)	0.0401	0.066	0.0411	0.084
$S_{\Delta L=2}$	0.234(9)	0.25(2)	0.279(10)	0.274(13)
$S_{\Delta L=1}/S_{\Delta L=0}$	0.251(13)	0.202(9)	0.200(8)	0.309(8)
$S_{\Delta L=1}/S_{\Delta L=2}$	0.171(7)	0.26(2)	0.147(5)	0.307(15)
$S_{\Delta L=2}/S_{\Delta L=0}$	1.46(9)	0.77(7)	1.35(7)	1.01(5)

Table 5.8: Cross section scaling factors of the ground, 50 keV and 221 keV states for the three global parameter sets and the fitted parameters. a) shows the cross section scaling factors that were obtained by fitting the sum $\Delta L = 0$, $\Delta L = 1$, and $\Delta L = 2$ DWBA to the angular distribution of all protons from transfer reactions. b) shows the results from fixing the $\Delta L = 1$ contribution with the cross scaling factor determined in subsection 5.2.4.

For all parameter sets the $\Delta L = 1$ angular distribution ($2p3/2^-$ configuration) describes the observed data best, only for the global parameter set from [Kon03] & [Loh74], and the fitted parameters is the calculation for $\Delta L = 0$ as good as the $\Delta L = 1$ calculation.

A $2s1/2^+$ configuration is however excluded by a proton knockout experiment [Mil09], which determined the spin of this state to be $J = 3/2$.

5.2.5 Ground State and 50.5 keV State

Even though it is not possible to resolve the ground state (which emits no γ-rays) and the 50 keV state (which de-excites outside of MINIBALL) of ^{31}Mg in this experiment, it is possible to gain some information about them.

The angular distribution of all transfer protons should contain the contributions from the $2s1/2^+$ ground state, the (potential $1d3/2^+$) state at 50 keV, and the (known) contribution from the $2p3/2^-$ state at 221 keV (see subsection 5.2.4). It contains also some small contribution from higher lying states. The angular distribution of all transfer protons was produced from the identified protons that are inside the excitation energy cut for protons from transfer reactions (see chapter 4), to reduce any background from fusion or compound reactions.

By fitting the sum of $\Delta L = 0$ (ground state), $\Delta L = 2$ (50 keV state), and $\Delta L = 1$ (221 keV state) DWBA calculations to said angular distribution the cross section scaling factors for the three contributions can be determined (see table 5.8). Fixing the $\Delta L = 1$ contribution to the value determined by the fit of the angular distribution of protons in coincidence with γ-rays from the 221 keV state yields different values for the other two ΔL values without changing the goodness of the fit.

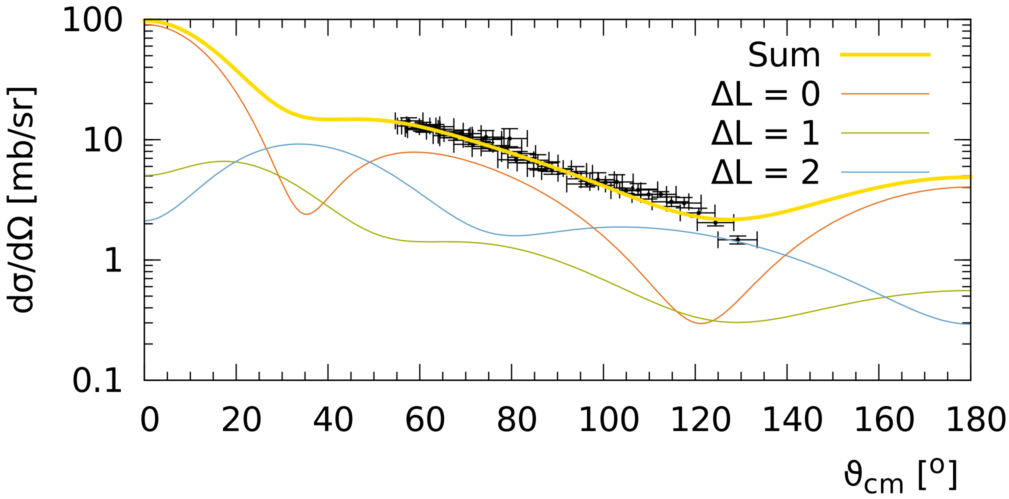

a)

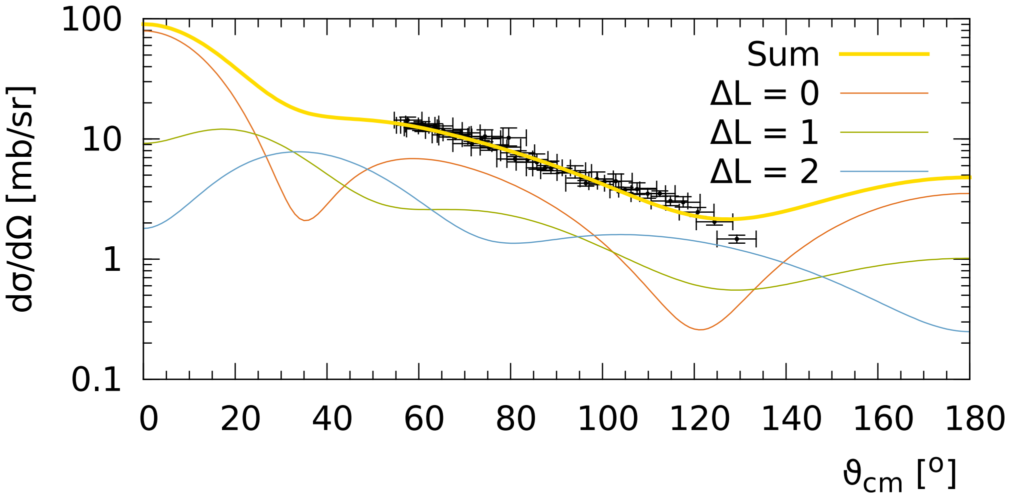

b)

Figure 5.15: a) shows the angular distribution of all transfer protons, fitted with the sum of $\Delta L = 0$, $\Delta L = 1$, and $\Delta L = 2$ DWBA calculations. b) shows the angular distribution of all transfer protons, fitted with the sum of $\Delta L = 0$ and $\Delta L = 2$ DWBA calculations and a fixed $\Delta L = 1$ contribution.

The resulting fits and the contribution from the different DWBA calculations is shown for the example of the fitted parameters in figure 5.15. The resulting transfer cross section scaling factors and their ratios differ quite a lot for the different optical model parameter sets, but for all four parameter sets and for all three fits the factor of the 221 keV state is about a factor two to four smaller than those for the ground and first excited state. The factor for the ground state seems to be slightly smaller than the factor of the 50 keV state (except for the [Kon03] & [Loh74] parameter set).

5.2.6 Discussion

Figure 5.16 shows the Nilsson diagram for ^{31}Mg [Ham07] with the positive parity levels shown as solid lines and the intruding negative parity levels as dashed or dash-dotted lines. For prolate deformations around $\beta = 0.5$ the ground state configuration of ^{31}Mg has two neutrons in the $K^{\pi}[Nn_z\Lambda] = 1/2^{-}[330]$ level (which belongs to the

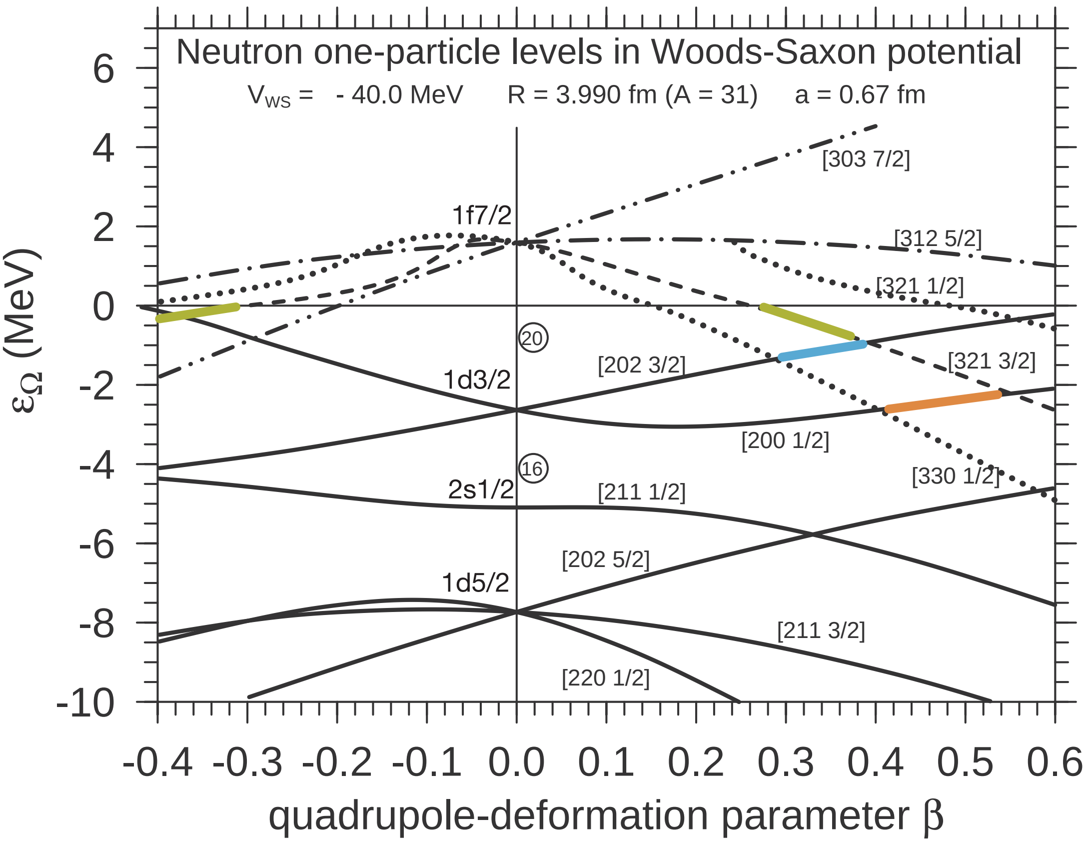

Figure 5.16: Nilsson diagram for ^{31}Mg, taken from [Ham07]. Orbitals are denoted by $[Nn_z\Lambda\ K]$. Highlighted are the orbitals of the valence neutron (or the hole in the ^{32}Mg core) for the ground state (orange), the 50 keV state (blue), and the 221 keV state (green).

Figure 5.17: Calculated potential energy surface for ^{30}Mg [Rod08]. The black lines show the energy surface for particle number projected (dashed) and angular momentum projected (solid) calculations. The blue line shows the probability density for finding a configuration with a given deformation β in the ground state.

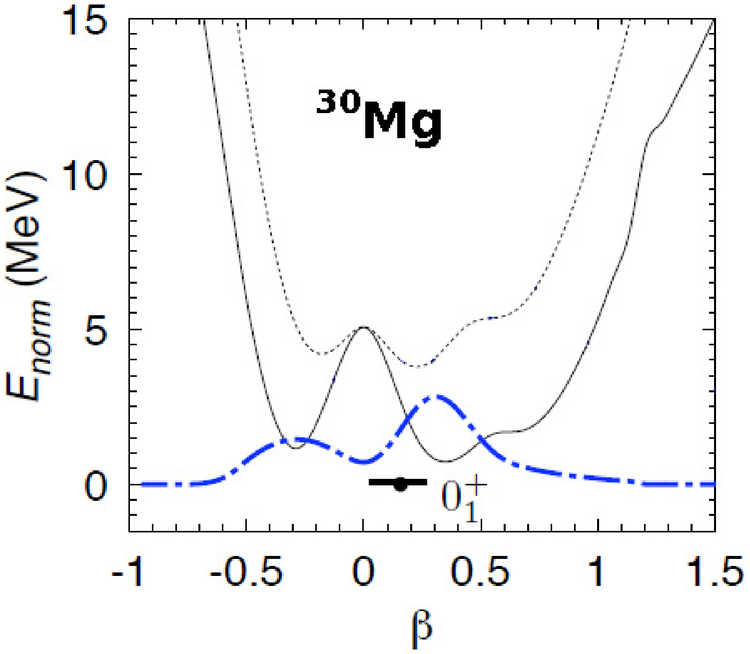

$1f7/2^-$ orbital) and one neutron in the $1/2^+[200]$ level containing contributions from the $1d3/2^+$ and $2s1/2^+$ orbitals. For the first excited level the neutron is lifted from the $1/2^+[200]$ level into the $3/2^+[202]$ level originating from the same $1d3/2^+$ orbital.

The comparison of the DWBA calculations for different transferred orbital angular momenta with the observed angular distribution shows that the 221 keV level in ^{31}Mg is an $l = 1$ state. Together with the results of a proton knockout experiment [Mil09], which determined from the angular distribution of γ-rays the spin of this state to be $J = 3/2$, the 221 keV level is a $K^\pi = 3/2^-$ level.

Comparing the cross section scaling factors determined for the 221 keV state with those obtained for the ground and 50 keV first excited state, shows that the latter are about a factor two to four larger than the former, see table 5.8.

The cross section of transfer reactions is proportional to the probability to find the final state of the reaction to be one neutron coupled to the projectile. For deformed nuclei in the description of the Nilsson model this probability depends on the configuration mixing of the spherical configuration with $J = j$ (see chapter 2). The transfer cross section also depends on the probability to find the projectile in its ground state in the same configuration (and deformation) that this ‘‘core’’ has in the ejectile, i.e. the probability that the initial and final state have similar deformations. If the deformation in the projectile were substantially different, a re-arrangement of several nucleons would need to take place during the transfer reaction, which is unlikely.

Looking at the results of beyond mean-field calculations [Rod08] in figure 5.17, one can see that the overall rather spherical ground state of ^{30}Mg has prolate contributions ($\beta \approx 0.3$) as well as oblate contributions ($\beta \approx -0.3$). The latter are weaker in this calculation than the former, which would lead to smaller transfer cross sections to oblate deformed states than to prolate deformed states in ^{31}Mg. It is thus possible to populate the deformed states in ^{31}Mg via a transfer reaction starting from the spherical ^{30}Mg.

For the $1/2^+[200]$ ground state configuration only contributions to the Nilsson wave function that originate from the $2s1/2^+$ orbital are populated in the transfer reaction. The repulsion of the $1/2^+[211]$ level originating from the $2s1/2^+$ orbital by the $1/2^+[200]$ level originating from the $1d3/2^+$ orbital in figure 5.16 indicates a strong mixing of the $2s1/2^+$ orbital to the wave function of the $1/2^+$ ground state at $\beta \approx 0.5$. Consequentially the cross section for populating the ground state in a transfer reaction would be expected to be relatively high. The $3/2^+[202]$ level that forms the first excited level in ^{31}Mg originates from the same $1d3/2^+$ orbital, so that the transfer cross section for this state would be expected to be even higher.

There are two possible $K^\pi = 3/2^-$ levels, one at prolate deformations similar to those of the ground and first excited states and one at oblate deformations, both originating from the $1f7/2^-$ orbital. Only the configuration mixing from the $2p3/2^-$ orbital in the $K^\pi = 3/2^-$ level can however contribute to the transfer cross section.

In figure 5.16 no evidence can be seen for such a mixing in the $3/2^-[321]$ level at prolate deformations. The $1/2^-[321]$ level that can be seen going from unbound to bound for deformations $\beta > 0.5$ originates from the $2p3/2^-$ orbital. The $3/2^-$ level stemming from the same orbital would be upsloping with increasing prolate deformation, thus making a mixing with the $3/2^-[321]$ level rather unlikely.

For oblate configurations however, the $K^\pi = 3/2^-$ level originating from the $2p3/2^-$ orbital is expected to come down so that a larger mixing can be expected. Indeed, the complicated behavior of the $K^\pi = 1/2^-$ level for oblate deformations indicates the influence of the $2p3/2$ and $2p1/2$ levels. The slope of the $K^{\pi} = 1/2^{-}$ for $\beta < -0.3$ indicates that the $2p3/2$ level lies below the $1f7/2$ level, while the slope for $-0.2 < \beta < -0.14$ indicates that the $2p1/2$ orbital lies above the $1f7/2$ orbital, see also [Ham07].

It is thus more likely that the $K^{\pi} = 3/2^{-}$ state has an oblate configuration, leading to a shape coexistence in ^{31}Mg. However, further information about the expected transfer cross sections in the above mentioned calculations as well as more detailed structure calculations are needed to validate the above, rather qualitative, considerations.

Chapter 6

Summary and Outlook

In this thesis the d (^{30}Mg, p) ^{31}Mg reaction was used to study ^{31}Mg, an isotope on the ‘‘shore’’ of the ‘‘Island of Inversion’’. The angular distribution of protons in coincidence with γ-rays from the de-excitation of the second excited state at 221 keV identified the state for the first time as an $l = 1$ state.

The experiment was performed with the new T-REX charged particle detector setup. The T-REX setup is optimized for transfer reactions with radioactive beams in inverse kinematics and was developed, built, installed, and used as part of this thesis. The T-REX setup consists of ΔE - $\mathrm{E_{Rest}}$ telescopes made out of position sensitive silicon detectors that cover almost 4π of the solid angle and the setup can be combined with the MINIBALL γ-ray detector array. It has a large solid angle for the detection and identification of the light recoils from transfer reactions and allows, in combination with the MINIBALL Germanium detector array, the tagging of the excited states by their characteristic γ-rays, thus achieving an optimal resolution in excitation energy.

The first radioactive beam experiment performed with T-REX was the d (^{30}Mg, p) ^{31}Mg experiment. The d (^{30}Mg, p) ^{31}Mg reaction populated mainly the ground state and the two lowest excited states of ^{31}Mg at 50 keV and 221 keV. The angular distribution of protons in coincidence with γ-rays from the de-excitation of the second excited state at 221 keV identified it for the first time as an $l = 1$ state. Together with the results of a proton knockout experiment [Mil09], which determined from the angular distribution of γ-rays the spin of this state to be $J = 3/2$, the 221 keV level is $K^{\pi} = 3/2^{-}$.

Due to its long half life the γ-rays of the first excited state could not be detected in the MINIBALL array with good efficiency, so that it was impossible to tag the population of this state (or the ground state) by coincident γ-rays. An analysis of the angular distributions of all protons from transfer reactions, however, allowed to determine the cross section scaling factor for the second excited state to be a factor two to four smaller than those of the ground state and the first excited state. The cross section scaling factors of the first excited and the ground state are of the same order.

This result agrees with an interpretation of ^{31}Mg in the Nilsson model. Here the ground state is formed by one neutron in the $K^{\pi}[Nn_z\Lambda] = 1/2^{+}[200]$ level which originates from the spherical $1d3/2^{+}$ orbital but contains strong mixing from the $2s1/2^{+}$ level (which alone is populated in transfer reactions). In the first excited state one neutron occupies the $3/2^{+}[202]$ level, which stems from the spherical $1d3/2^{+}$ orbital as well and can be directly populated by transfer reactions, implying an even larger cross section than for the ground state.

For the second excited state two possible configurations exist in the Nilsson model. According to [Ham07] the $3/2^-[321]$ level that originates from the $1f7/2^-$ orbital can be bound at prolate as well as oblate deformations. It has to contain a mixing with the $2p3/2^-$ level which alone contributes to the transfer cross section. However, in this calculation the $3/2^-[321]$ level is already unbound at $\beta = 0$ and should rise for $\beta > 0$. Therefore one naively would not expect such a mixing. The oblate deformed $3/2^-[321]$ level on the other hand seems to contain some mixing from the $2p3/2^-$ level. This would be able to explain the smaller transfer cross section scaling factor by the smaller contribution of oblate configurations to the ground state of ^{30}Mg that forms the ‘‘core’’ of any state populated in the transfer reaction.

To get a more quantitative interpretation of the configuration of the 221 keV level in ^{31}Mg further theoretical studies of the expected configurations and the expected transfer cross sections are required.

Another way to acquire information on the shape of the state could be Coulomb excitation of ^{31}Mg as it was performed in 2008 [Sei1x]. The electric dipole excitation from the $1/2^+$ ground state to the $3/2^-$ state at 221 keV is not as strong as the electric quadrupole excitation within the rotational band build on the $1/2^+$ ground state so that only the $(3/2^+)$ state at 50 keV and the $(5/2^+)$ state at 945 keV were populated sufficiently strong. The confirmation of the shape coexistence of an oblate $3/2^-$ state at 221 keV is thus still missing.

Future experiments could take advantage of HIE-ISOLDE, which will provide higher beam intensities and, even more important for transfer reactions in inverse kinematics, higher beam energies of up to 5 MeV u^{-1} in the first stage and later up to 10 MeV u^{-1} [Lin08]. The increased beam energy results in more pronounced angular distributions and makes transfer experiments with higher mass beams feasible. The intensity upgrade could increase the beam intensities by a factor ten, which would allow access to more exotic nuclei, making perhaps a d(^{32}Mg, p)^{33}Mg or t(^{32}Mg, p)^{34}Mg experiment possible. Such experiments could yield valuable information on the evolution of single particle states across the Island of Inversion.

With the higher beam energy and intensity the d(^{30}Mg, p)^{31}Mg experiment could also be repeated to determine the single particle properties of the excited states that were not accessible in the data presented in this work. With a factor 20 higher statistics than it was obtained during the 25 h beam time presented in this work, angular distributions of protons in coincidence with γ-rays of the 50 keV, 461 keV, 673 keV, and 1436 keV levels of ^{31}Mg would be accessible [Bil05]. The higher beam energies would also give rise to more pronounced angular distributions, making the distinction of different transferred angular momenta stronger.

The development and construction of T-REX has started a program of one and two neutron transfer reactions at REX-ISOLDE. The lightest beam used was ^{11}Be with which the three Beryllium isotopes ^{10,11,12}Be were studied, using the d(^{11}Be, t)^{10}Be, d(^{11}Be, d)^{11}Be, and d(^{11}Be, p)^{12}Be reactions to study the halo states and the vanishing of the $N = 8$ magic number in these nuclei [Bor04]. It is planned to continue the exploration of this region of the chart of nuclei with a ^{12}Be beam to reach the unbound ^{13}Be.

The t(^{30}Mg, p)^{32}Mg experiment in 2008 studied the shape coexistence of the second 0^+ state in ^{32}Mg [Wim10a, Wim10b], further exploring the Island of Inversion with the help of T-REX. The t(^{44}Ar, p)^{46}Ar and d(^{44}Ar, p)^{45}Ar experiments in 2010 aimed at the investigation of the shape-coexistence in a region with a weakening

$N = 28$ shell gap and spin assignments of the excited states in ^{46}Ar [Wim09].

The d (^{66}N, p) ^{67}Ni reaction was used to study ^{67}Ni, a nucleus just one neutron shy of the closed sub-shell $N = 40$ and with a closed proton shell at $Z = 28$. Studying the excited states of ^{67}Ni can lead to more insight on the nature of the semi double-magic ^{68}Ni that will also be studied in a planned t (^{66}Ni, p) ^{68}Ni experiment [Pat08] in the next years.

The heaviest beam used so far for transfer reactions at REX-ISOLDE is ^{78}Zn, which was used to study ^{79}Zn by the d (^{78}Zn, p) ^{79}Zn reaction. ^{79}Zn lies with $Z = 30$ and $N = 49$ two protons above and one neutron below the double shell closure at ^{78}Ni. The single particle structure of the low-lying states in ^{79}Zn (especially the behavior of the $g9/2$ and $d5/2$ orbitals) will provide information on the persistence of the $N = 50$ shell gap for this neutron rich region in the chart of nuclei [Orl09].

A planned transfer reaction in the Island of Inversion is the study of ^{29}Na via the d (^{28}Na, p) ^{29}Na reaction [Krö10]. ^{29}Na is like ^{31}Mg on the "shore" of the Island of Inversion, with ^{27,28}Na showing no significant intruder configuration and the ground states of ^{30,31}Na being completely dominated by intruder configurations. Unlike in the Magnesium isotopes the transition seems to be smoother with the ground state of ^{29}Na being half and half [Uts04].

The use of even heavier beams than ^{78}Zn will be made possible by the HIE-ISOLDE upgrade mentioned above.

Also further technical improvements of T-REX are planned, e.g. the bridging of the gap between forward and backward barrel by a $\vartheta_{\text{lab}} = 90°$ detector mounted on the target ladder. Details are described in appendix E.

Appendix A

MINIBALL Efficiency

The efficiencies determined from the decay of ^{152}Eu have to be corrected for two effects. If during the de-excitation of the daughter nucleus (^{152}Sm or ^{152}Gd) more than one γ-ray is emitted to one detector, the efficiency to detect one γ-ray with its full energy (photo-peak efficiency) is reduced by the total efficiency to detect any energy deposited by the second γ- or x-ray, which would shift the total energy detected out of the photo-peak of the first γ-ray.

The other effect is that alternate paths might exist between two energy levels, which are the emission of a single γ-ray or two in cascade. The latter may be summed by coincident full energy detection and thus contribute to the single γ-ray photo peak. To correct for these additional counts the photo-peak efficiencies ϵ_t of the three γ-rays involved need to be known. One can however use the photo-peak efficiencies determined without these corrections as an approximation since the corrections for both effects are only a few percent, see figure A.1.

The factors for these corrections were taken from [Sch83] with a few corrections calculated from [NND] (see table A.1). The photo peak efficiencies needed for the correction were taken from a fit (see also chapter 4) of the uncorrected data points, as mentioned above.

The total detection efficiencies ε_t are taken to be

$$\varepsilon_t = \Delta\Omega \exp(-\mu(E)L) \tag{A.1}$$

where the attenuation coefficient $\mu(E)$ is taken from [NIS], L is the length of one crystal in g cm^{-2} ($\approx$ 40 g cm^{-2} for MINIBALL detectors), and $\Delta\Omega$ is the solid angle covered by one crystal/one cluster. The solid angle covered by one crystal is calculated at the average penetration depth d_p of a γ-ray

$$d_p = -\frac{\log\left(1 + \exp(-\mu(E)L)\right)/2.}{\mu(E)} \tag{A.2}$$

from the geometry of the crystals using a distance of 120(10) mm between target and front of the crystal, leading to a coverage of 1.7–0.8 % of $4\,\pi$.

If the addback method is used, the energies from the three crystals in one MINIBALL cluster are added together to obtain the photo peak efficiency of the cluster, otherwise the resulting photo peak efficiency is that of the crystals. Since one MINIBALL cluster consists of three crystals the solid angle covered by the cluster is a factor three larger, which leads to a larger correction for the efficiencies determined with the ^{152}Eu source. A more complete analysis of the corrections needed for a ^{152}Eu

γ-ray energy in keV	*correction factors*		
121.782	1.0	$-\,0.772\;\varepsilon_t\,(42.5)$	$-\,0.105\;\varepsilon_t\,(244.697)$
		$-\,0.247\;\varepsilon_t\,(964.1)$	$-\,0.235\;\varepsilon_t\,(1112.074)$
		$-\,0.073\;\varepsilon_t\,(867.373)$	$-\,0.364\;\varepsilon_t\,(1408.01)$
		$-\,0.005\;\varepsilon_t\,(719.349)$	$-\,0.029\;\varepsilon_t\,(443.965)$
		$-\,0.008\;\varepsilon_t\,(295.9392)$	$-\,0.009\;\varepsilon_t\,(1457.643)$
		$-\,0.024\;\varepsilon_t\,(1212.948)$	
244.697	1.0	$-\,1.060\;\varepsilon_t\,(42.5)$	$-\,0.461\;\varepsilon_t\,(121.782)$
		$-\,0.628\;\varepsilon_t\,(867.373)$	$-\,0.040\;\varepsilon_t\,(719.349)$
		$-\,0.016\;\varepsilon_t\,(295.9392)$	$-\,0.210\;\varepsilon_t\,(1212.948)$
344.279	1.0	$-\,0.003\;\varepsilon_t\,(42.5)$	$-\,0.061\;\varepsilon_t\,(411.1)$
		$-\,0.006\;\varepsilon_t\,(764.9)$	$-\,0.353\;\varepsilon_t\,(778.9)$
		$-\,0.023\;\varepsilon_t\,(367.8)$	$-\,0.047\;\varepsilon_t\,(1089.7)$
		$-\,0.013\;\varepsilon_t\,(678.8)$	$-\,0.013\;\varepsilon_t\,(586.2648)$
		$-\,0.044\;\varepsilon_t\,(1299.1)$	
443.965[a]	$(1.0$	$+\;\frac{0.0003\;\varepsilon_p(148.010)\;\varepsilon_p(295.9392)}{\varepsilon_p(443.965)})\;\cdot$	
	$(1.0$	$-\,0.243\;\varepsilon_t\,(121.782)$	$-\,0.095\;\varepsilon_t\,(244.697)$
		$-\,0.527\;\varepsilon_t\,(964.1)$	$-\,0.369\;\varepsilon_t\,(1085.869))$
778.904	$(1.0$	$+\;\frac{0.065\;\varepsilon_p(411.1163)\;\varepsilon_p(367.7887)}{\varepsilon_p(778.904)})\;\cdot$	
	$(1.0$	$-\,0.028\;\varepsilon_t\,(42.5)$	$-\,0.962\;\varepsilon_t\,(344.2785)$
		$-\,0.004\;\varepsilon_t\,(520.227))$	
964.1	1.0	$-\,1.064\;\varepsilon_t\,(42.5)$	$-\,0.385\;\varepsilon_t\,(121.782)$
		$-\,0.116\;\varepsilon_t\,(443.965)$	
1085.84[b]	$(1.0$	$+\;\frac{0.589\;\varepsilon_p(121.782)\;\varepsilon_p(964.1)}{\varepsilon_p(1085.869)})\;\cdot$	
	$(1.0$	$-\,0.771\;\varepsilon_t\,(42.5)$	$-\,0.116\;\varepsilon_t\,(443.965))$
1408.01	$(1.0$	$+\;\frac{0.011\;\varepsilon_p(244.697)\;\varepsilon_p(719.349)}{\varepsilon_p(1408.01)}$	
		$+\;\frac{0.079\;\varepsilon_p(443.965)\;\varepsilon_p(964.1)}{\varepsilon_p(1408.01)}$	
		$+\;\frac{0.016\;\varepsilon_p(295.9392)\;\varepsilon_p(1112.074)}{\varepsilon_p(1408.01)})\;\cdot$	
	$(1.0$	$-\,1.046\;\varepsilon_t\,(42.5)$	$-\,0.461\;\varepsilon_t\,(121.782))$

Table A.1: The correction factors for the efficiency calibration with ^{152}Eu. ε_t denotes the total efficiency to detect a γ-ray while ε_p denotes the photo peak efficiency. 42.5 keV is taken as the average energy of the x-rays emitted after the removal of an electron from the K-shell due to conversion.

---

[a] Missing in [Sch83], values taken from [NND].

[b] Sum peak probability updated by values from [NND].

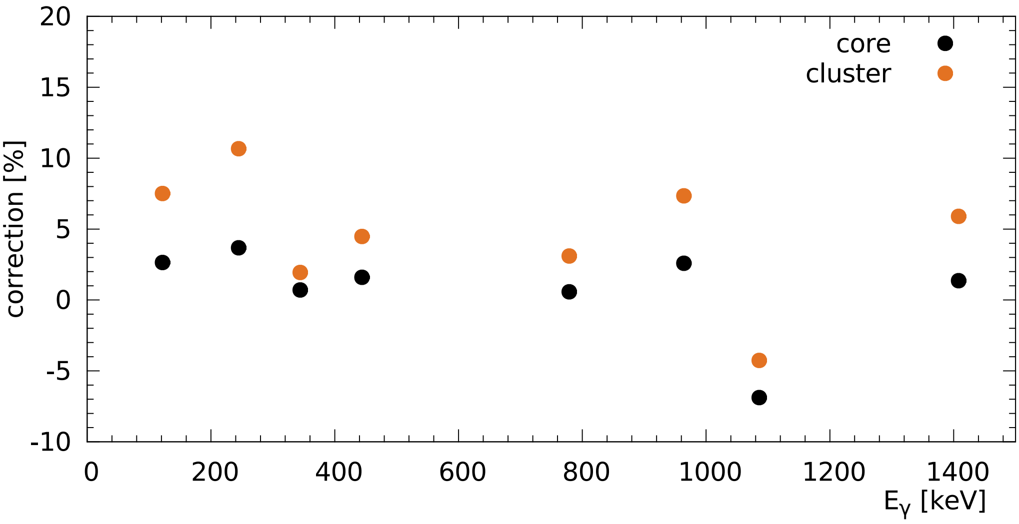

Figure A.1: The correction factors for the efficiency calibration with ^{152}Eu as calculated from A.1, once for a single crystal and once for a whole cluster consisting of three crystals.

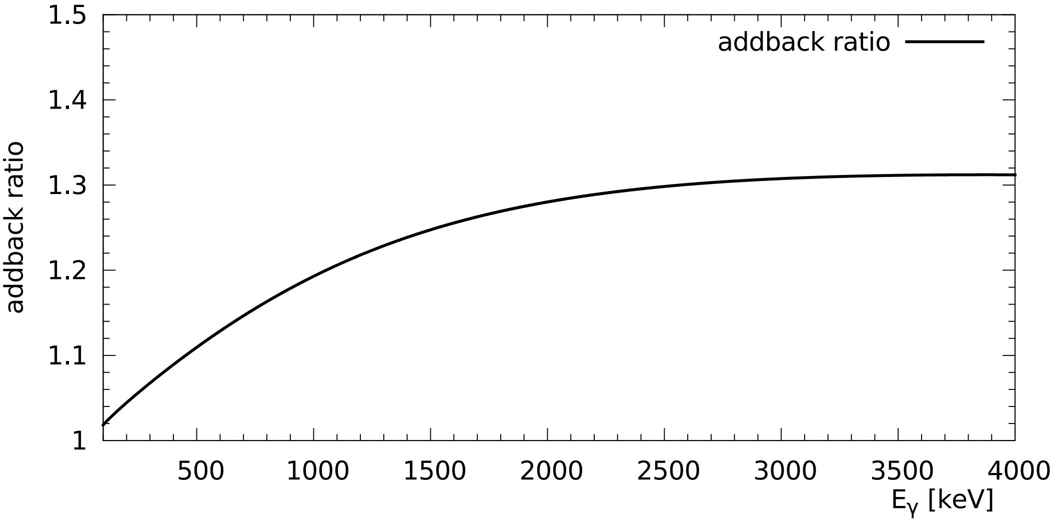

Figure A.2: The ratio of the photopeak efficiency of MINIBALL with and without addback.

source would require a full Monte-Carlo simulation of the source and the detectors, e.g. to account for the angular distributions of the γ-rays and the absorption of x- and γ-rays in material between the source and detectors.

Appendix B

New Beam Diagnostics and Target Mounting

To improve the beam diagnostics for the low intensity radioactive ion beams two new detectors were integrated in the T-REX setup:

(i) a PCB with four PiN diodes ($10 \times 10\,\mathrm{mm}^2$) around a 10 mm hole is placed as an active collimator in front of a tantalum collimator, see also figure 3.5 and

(ii) a $10\,\mu\mathrm{m}$ thick poly-crystalline CVD diamond detector which is segmented into 9 pixels (figure 3.9) can be mounted on the lowest position of the target ladder and used to ensure that the beam is centered and focused at the target position.

The readout of these auxiliary detectors is presented in the first section of this appendix.

In order to maintain the close setup of the particle detectors the target mounting had to be realized within as little space as possible and to a good accuracy. This was accomplished by using target ladders that are slid into the small gap between forward and backward barrel detectors and are shown in the second section of this appendix.

B.1 Readout of Beam Diagnostics Detectors

The readout of the signal generated by each particle impinging on the beam diagnostics detectors (especially the diamond detector) would require very fast electronics since the instantaneous beam rate can be as high as $\approx 5 \times 10^7\,\mathrm{s}^{-1}$. But as long as it is not necessary to count each particle individually to see the position of the beam, the signals of the nine pixels of the diamond detector, its unsegmented rear side, and the four PiNs of the active collimator can be integrated by collecting their charge individually in small capacitors. The total charge deposited in one such capacitor is converted in to a voltage signal by an operational amplifier. The capacitor can be discharged by applying a TTL[1] signal to a photo-MOSFET[2] which is similar to closing a switch that discharges the capacitor, see also figure B.1. This can be used as a fast-reset of the signal integration so that all charge created in the detectors during one beam pulse can be integrated.

---

[1] **T**ransistor-**T**ransistor-**L**ogic

[2] photoelectric **M**etal-**O**xide-**S**emiconductor **F**ield-**E**ffect-**T**ransistor

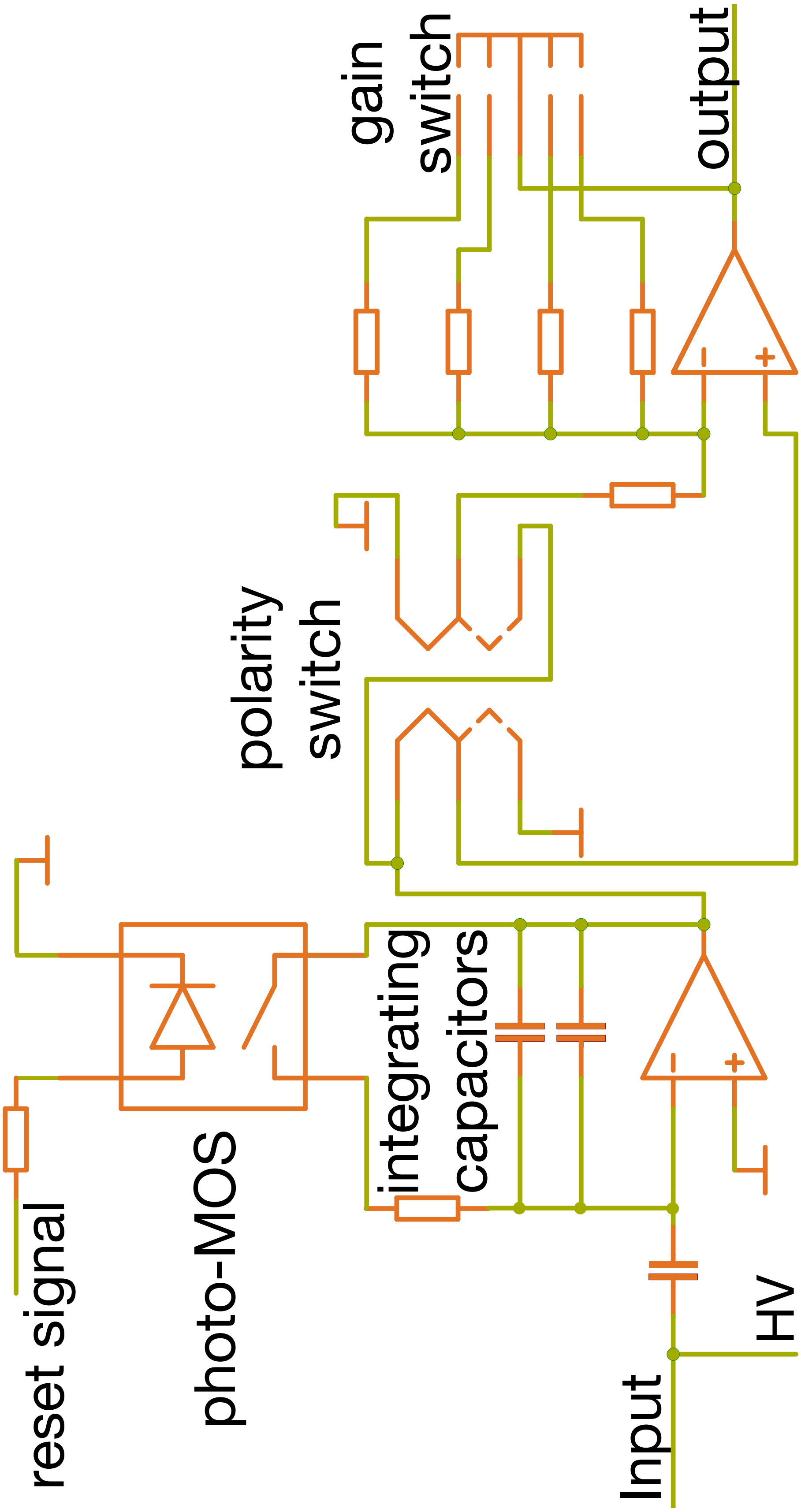

Figure B.1: Schematics of the integrator for the beam diagnostic detectors.

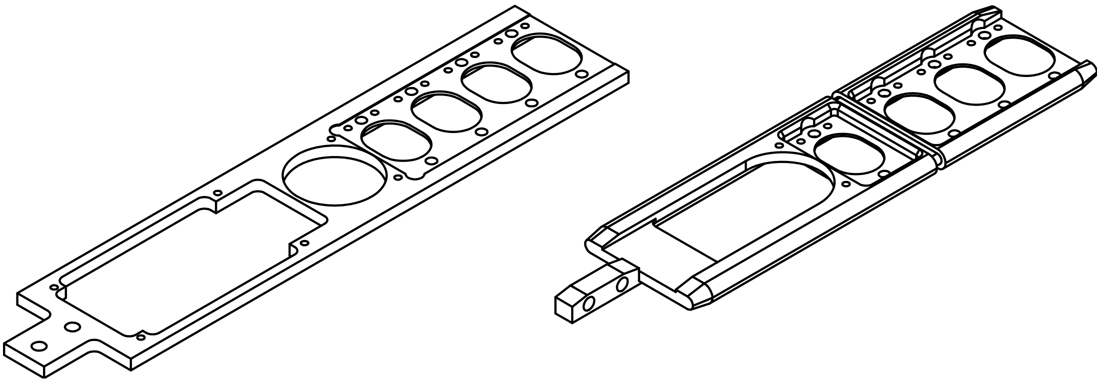

Figure B.2: Technical drawings of the target ladders, the side facing the beam upward. On the left the older target ladder with four target positions and space for the diamond detector. On the right is the newer tritium target ladder with three normal target positions and one for the tritium target. The tritium target ladder has space below the lowest target (in this case the tritium target) for beam monitoring detectors.

The integrated signals of the beam diagnostics detectors are fed directly into an independent ADC which is gated by the on- and off-beam windows. The peak sensing of the ADC thus allows to measure the maximum charge accumulated in an on- and off-beam window so that the charge accumulated in the preamplifiers due to leaking currents can be subtracted from the on-beam values.

B.2 Target Ladders

In order to perform (t,p) experiments like the t(^{30}Mg, p)^{32}Mg experiment a tritium target is needed. This was realized by using a 500 μg cm^{-2} titanium foil loaded with 40 μg cm^{-2} tritium.

The low energies of the β-particles from the decay of tritium (end point energy of 18.590(2) keV) make their shielding very easy. In the highly improbable case that gaseous tritium were to be released from the target however it would be very dangerous, so keeping it contained is a mayor issue for radiation protection. The release of tritium from the titanium foil should only happen at high temperatures, which are reached at high beam intensities, much above the beam intensities available at REX-ISOLDE. But as an extra precaution a new target ladder was designed to seal the target mounted at the lowest position airtight once the target ladder is fully retracted.

The two target ladders are shown in figure B.2, the conventional one on the left and the new tritium target ladder on the right.

Appendix C

Different Setup Options

In this appendix different possible setups for the particle detectors that were considered for the T-REX setup will be discussed concerning their expected performance.

In order to keep the number of electronic channels small it was agreed early in the planning stage to use position sensitive resistive strip detectors with two different possible geometries:

(i) $40 \times 40\,\mathrm{mm}^2$ detectors with 4 position sensitive resistive strips which were already available from an other experiment at CEA Saclay and were made by Canberra

(ii) $50 \times 50\,\mathrm{mm}^2$ detectors with 16 position sensitive resistive strips which could be bought from Micron Semiconductors

All considered barrel detector configurations have in common that they were planned to consist of ΔE - $\mathrm{E}_{\mathrm{Rest}}$ telescopes in the forward direction in order to allow particle identification. This is necessary to distinguish between elastically scattered protons and deuterons, tritons from the (d,t) reaction, and protons from the (d,p) reaction. Kinematics allow the elastic scatted particles and tritons from the (d,t) reaction to be only emitted under laboratory angles above 90°, so at first no such ΔE - $\mathrm{E}_{\mathrm{Rest}}$ telescopes were considered necessary in backward directions.

C.1 Hexagonal Setup without Overlaps

In this scenario two times six $40 \times 40\,\mathrm{mm}^2$ detectors are placed in the shape of a hexagon around the target (figure C.1). With this setup the symmetry between the CD detectors (which are segmented in four quadrants) and the barrel detectors is quite low and the gaps between the detectors (due to the size of the PCB) mean that a large part of the φ angles is not covered. Since in this setup the strips of the barrel detectors are parallel with the beam direction and the distance between the beam axis and the detectors is rather large the ϑ resolution is rather good (the position resolution of the strips is more than a factor 10 better than the strip width of $\approx$10 mm).

C.2 Hexagonal Setup with Overlaps

In order to reduce the gaps between the detectors and increase the covered solid angle an other setup considered was with the same $40 \times 40\,\mathrm{mm}^2$ detectors but

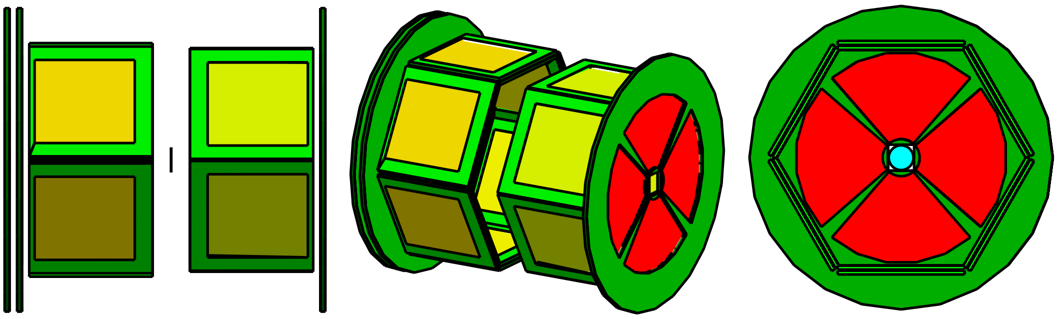

Figure C.1: Schematic of hexagonal setup without overlaps. View from the left side on the left, view from $\vartheta = 90°, \varphi = 0°$ in the middle and view in beam direction without the backward CD on the right.

rotated so that in this case the strips are perpendicular to the beam direction (see figure C.2). This and the fact that the detectors are much closer to the beam axis decreases the ϑ resolution quite a bit in comparison to the "normal" hexagonal setup. The symmetry between barrel and CD detectors is also even less than in the previous setup.

C.3 Quadratic Setup

In this setup two times four $50 \times 50\,\text{mm}^2$ detectors are positioned in a square around the target at a distance of 29 mm from the beam axis so that these detectors cover the same φ range as the CD detectors (81.6° out of 90°). This setup guarantees a high symmetry between the barrel and CD detectors, as both cover exactly the same φ range.

Two possible options for the arrangement of the barrel detectors were considered: placing the detectors with the strip parallel or perpendicular to the beam axis. The first would yield a much better ϑ_{lab} resolution since the position resolution of the detector along a strip is much better (less than 0.5 mm) than the strip width of 3.125 mm. However the necessary space needed to contact the strips requires more space between the target and the barrel detectors as well as between these and the CD detectors thus reducing the covered ϑ_{lab} range.

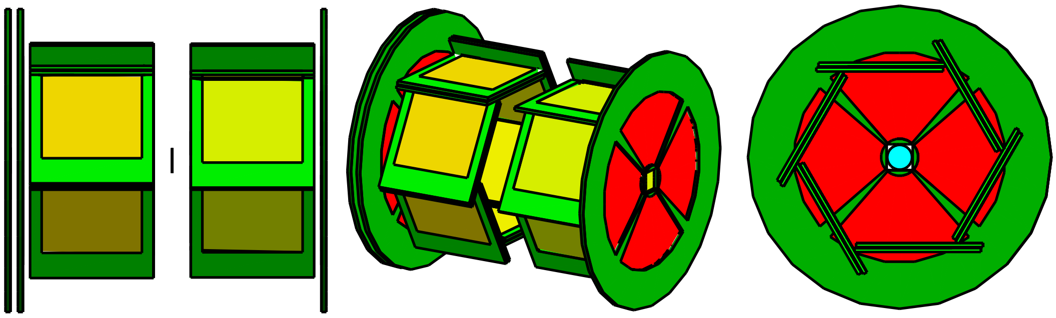

Figure C.2: Schematic of hexagonal setup with overlaps. View from the left side on the left, view from $\vartheta = 90°, \varphi = 0°$ in the middle and view in beam direction without the backward CD on the right.

C.4 Other Setups

Other setups that were considered as alternatives were an octagonal setup with eight barrel detectors in each the forward and backward direction, arranged in a similar overlapping shape as that of figure C.2, and quadratic setups with either shorter detectors to move the CD detectors closer to the target, detectors with less strips or the strips rotated so that they are parallel to the beam axis. The octagonal setup is very big and reduces thus the γ-ray detection efficiency since the MINIBALL detectors have to be moved further away from the target. The other quadratic setups are very similar to the one presented above so only the results will be shown in the next section.

C.5 Comparison of Setups

Five different setups have been simulated for a ^{30}Mg beam with 3 MeV u^{-1} on a deuterated PE target:

(i) $40 \times 40\,\text{mm}^2$ detectors with 4 position sensitive strips arranged in a hexagonal shape without overlaps

(ii) $40 \times 40\,\text{mm}^2$ detectors with 4 position sensitive strips arranged in a hexagonal shape with overlaps

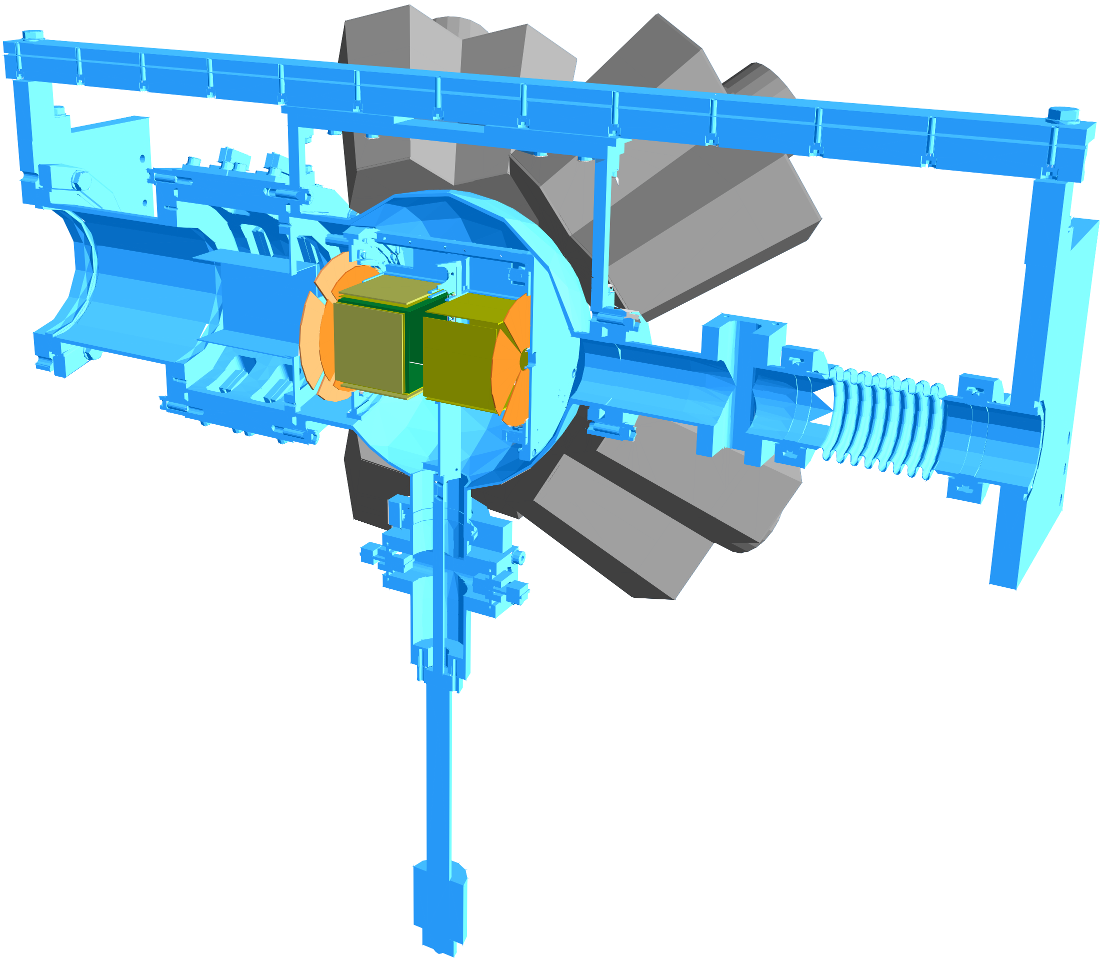

Figure C.3: Schematic of quadratic setup as it was used in 2007.

	ϑ Range in °				
Barrel Type	*CD*	*forward*	*backward*	*$\Delta\vartheta$ in °*	*ΔPosition in mm*
hex.	8–34	44–83	97–133	2.30–4.00	1.58–2.88
hex. overl.	8–26	30–72	108–150	4.18–6.44	1.63–4.09
quad.	8–27	31–78	103–148	3.22–6.13	1.86–4.64
quad. 8 str.	8–27	31–78	103–148	3.51–6.26	1.87–4.64
quad. short	8–29	35–75	106–145	3.07–5.49	1.57–3.77
quad. rot.	8–27	31–78	103–148	1.75–2.22	0.89–2.25

Table C.1: Comparison of covered ϑ range and resolution for different setup options, assuming a $5\,\mu$m deuterated PE target, 5 mm beamspot, and 50 keV energy resolution of the CD and barrel detectors. The ϑ and position resolution along a strip is given as a minimum and maximum since it depends strongly on the ϑ_{lab} angle.

	Detection efficiency in %								
	iso. d(^{30}Mg,^{31}Mg)			*iso. d(^{30}Mg,^{30}Mg)*			*iso. lab-system*		
Barrel Type	*CD*	*Barrel*	*Total*	*CD*	*Barrel*	*Total*	*CD*	*Barrel*	*Total*
hex.	19	42	60	47	16	63	13	46	59
hex. overl.	12	60	72	42	31	73	10	60	70
quad.	13	62	75	42	30	72	10	61	71
quad. 8 str.	13	62	75	42	30	72	10	61	71
quad. short	16	54	70	44	27	71	11	52	64

Table C.2: Comparison of setup efficiency for the different setup options.

(iii) 50 × 50 mm^2 detectors with 16 position sensitive strips arranged in a quadratic shape

(iv) 50 × 50 mm^2 detectors with 16 position sensitive strips arranged in a quadratic shape (every 2 strips bonded together)

(v) 50 × 40 mm^2 detectors with 16 position sensitive strips arranged in a quadratic shape (strips are only 40 mm long)

For each setup different combinations of target thickness (1 ng cm^{-2} and 5 μm), beam width (0 and 5 mm), and detector resolution (0, 50 and 100 keV) have been simulated. The detector resolution (energy and position wise) of the barrel was implemented by adding to the energy deposited in a detector a random number generated with a Gaussian distribution of a certain FWHM. This was done for the total energy deposited in the detector (corresponds to the backside of the detector) as well as for the energy deposited in one strip multiplied with the fraction of the detector length where the energy was deposited.

The analyzed data was then compared to the simulated data to determine the achievable ϑ resolution. The ϑ and position resolutions of the barrel detectors were obtained by calculating the root mean square of the difference between the simulated and the measured values and multiplying it with $2\sqrt{2\log 2}$.

An overview of the covered ϑ range and resolution for the different setups, assuming a 5 μm deuterated polyethylene target, 5 mm beam spot and 50 keV energy resolution for CD and Barrel is given in table C.1.

The efficiency of the different setups, which were obtained comparing the number of detected particles to the simulated particles are shown in table C.2. This was done for a simulation of transfer reactions with an isotropic distribution in the cm-system (first three columns), elastically scattered particles with an isotropic cm-distribution (next three columns) and for protons, deuterons, and tritons that were isotropic distributed in the laboratory system.

If the φ ranges covered by CD and barrel detectors were different, coupled with the fact that the MINIBALL array only covers certain φ ranges, the detection efficiency for particles in coincidence with detected γ-rays could be very different for the barrel detectors and the CD detectors. These (however small) uncertainties in the shape of the angular distribution of protons detected in coincidence with γ-rays can be avoided by using the quadratic setup, where the barrel and CD detectors cover the same φ range.

The ϑ_{lab} resolution ranges for this between 6.1 and 3.2° for the middle of the strip closest and furthest away from 90°, respectively. This resolution was deemed sufficient for radioactive beam experiments since the expected limited statistics doesn't allow for a binning of the ϑ_{lab} of much less than 5° anyway. Coupled with the relatively small size of the setup and the high solid angle covered by it this setup was deemed the best choice for T-REX.

Appendix D

Simulation

Before T-REX was built, as it is presented in chapter 3, different designs were studied (see also appendix C) using a Geant4 simulation. The same simulation was also used to determine the efficiency of the various cuts used in the analysis of the experimental data (see chapter 4).

This appendix describes the basic features of the simulation which is based on a MINIBALL simulation package [Boi09].

Besides the MINIBALL triple cluster which are implemented in the above mentioned simulation package, the simulation contains the following materials:

- the aluminum vacuum chamber,
- forward and backward segmented CD detectors,
- the CDE pad detectors,
- the barrel stack detectors,
- the target, and
- the screening foils,

where all detectors consist of the silicon mounted on a PCB.

The shape of the vacuum chamber can be either completely spherical (original Coulex chamber), spherical with a large flange in forward direction (T-REX chamber from 2007) or cylindrical with flanges in forward and backward direction (current T-REX chamber). The parameters of the shape, like length of flanges, diameter, wall thickness etc. can be adjusted via a settings file which is read in at the start of the simulation and controls the thickness and positions of the detectors and foils as well. Which detectors and foils are to be used in the simulation can be changed by the use of different command line flags.

The Geant4 simulation framework itself is geared towards the high energy physics at LHC and is thus missing low energy reactions like transfer reaction and Rutherford scattering. For this reason an event generator was implemented that generates the ejectiles, recoils, and γ-rays of such reactions.

The event generator of the simulation can be set via command line flags to simulate either

- an α-source (^{244}Cm, ^{241}Am and ^{239}Pu with or without ^{148}Gd),

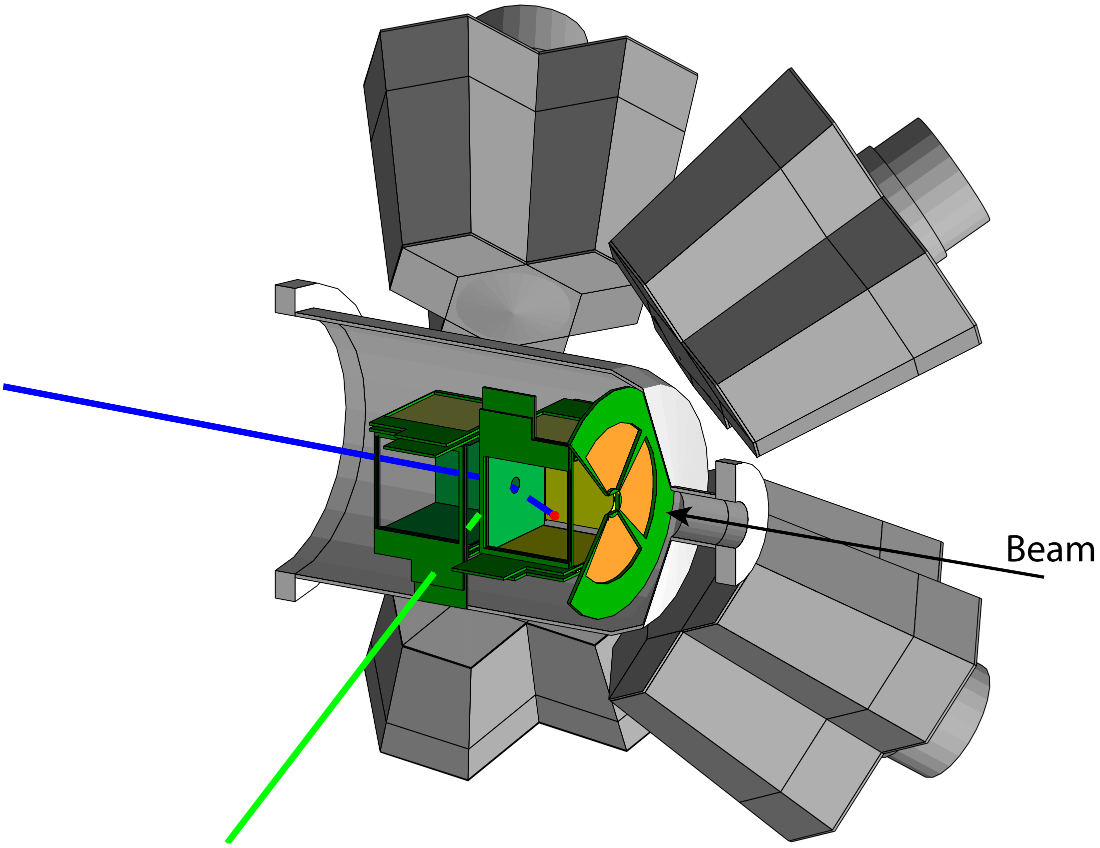

Figure D.1: The Geant4 simulation of the T-REX setup from 2008 together with a single transfer event with positive particles in blue, neutral γ-rays in green, and negative electrons (from ionization processes in the backward barrel detector) in red. The left side of the MINIBALL array, vacuum chamber, and particle detectors is cut away for visualization purposes.

- a ^{152}Eu or ^{60}Co γ-ray source or
- transfer and elastic scattering reactions combined with β-decay.

For the last option the calculated cross-sections can be used or the user specifies the percentage of transfer reactions and elastic scattering to be simulated. For both the transfer and the elastic scattering reactions the user provides the angular distributions in the center of mass system (e.g. the results of a DWBA calculation).

The data output format of the simulation is the same as the output of the calibration program, so that the output of the simulation can be used as input for the particle identification, energy loss calculations and the reconstruction of the ejectiles (see section 4.3).

Appendix E

Changes and Improvements of T-REX

T-REX has seen improvements to the setup between each years experiments, which will be outlined in this appendix.

The biggest change was after the first experiment in 2007, where the advantage of ΔE - E$_{\mathrm{Rest}}$-detectors in backward detection, to reduce the background from β-decay of radioactive beam that was stopped in the setup, was recognized. The change of detectors went hand in hand with a change of the vacuum chamber and a second target ladder which is suitable for tritium targets, see also subsection 3.4.2.

The problem of determining the target position along the beam axis, that came apparent in the analysis (see subsection 4.3.1), was solved by using rails which are mounted inside the barrel and guide the target ladder when it is moved in, see figure E.1. At the same time the mounting of the whole barrel was changed, so that the distance between the barrel and the feedthrough flange can be easily changed. This is not important for the T-REX setup for transfer experiments but for the future plans to use the T-REX setup for Coulomb excitation experiments as well (see section E.1).

The changes for the 2010 campaign were improved electronics for the readout of the active collimator and diamond detector (involving a few bug-fixes and the integration of all 16 channels in one housing), an aperture to shield the active collimator during beam tuning, and the installation of a fusion veto at the end of T-REX [Now1x].

One of the major drawbacks of the target ladder is the need to have a gap between forward and backward barrel detectors. At the moment this gap is quite big, 10 mm between the PCBs and an additional 3 mm on each PCB, giving a total gap of 16 mm between the active areas of the forward and backward barrel. There are different options to expand the covered ϑ_{lab} range covered by T-REX toward 90°. The easiest is to reduce the gap between the PCBs, since the reason to have such a large gap (to avoid any contact between the target ladder and the barrel detectors) is no longer valid due to the rails. The target ladder itself doesn't need to be thicker than 2–3 mm, meaning that the gap could be reduced by 6–7 mm (leaving 1 mm space between target ladder and detectors), which would reduce the gap around 90° from 78.2–101.8° to 82.6–97.4° (or $\Delta\vartheta_{\mathrm{lab}}$ from 23.6° to 14.8°).

To cover angles even closer to $\vartheta_{\mathrm{lab}} = 90°$, one would either need to move only the left and right barrel detectors closer together, which would create an asymmetry in the setup which might make later analysis more difficult, or one could install additional

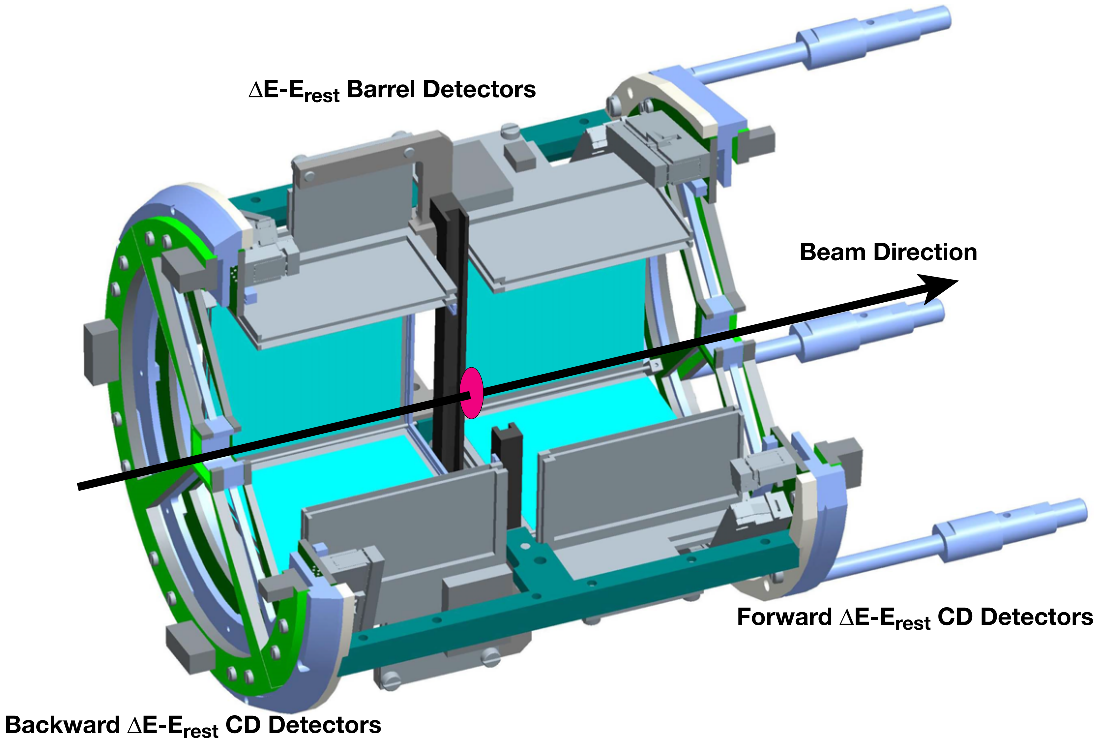

Figure E.1: Technical drawing of the silicon barrel as it was used in 2009. The main difference to the 2008 setup are the rails to guide the target ladder, which are shown in black.

detectors on each side of the target ladder. The latter could be easily achievable by adding two PiN-diodes to the right and left side of uppermost target. This would only require the readout of two more signals and the ϑ_{lab} range covered by these detectors would be at $\approx 15^\circ$ less than a factor of three bigger than the ϑ_{lab} range covered by the barrel strips closest to 90°. In any case the target would have to be tilted away from 90° to reduce its effective thickness at those angles. The feasibility of such an improvement to the T-REX setup is being studied and might be implemented in the future.

E.1 Coulex Experiments with T-REX

As mentioned above, it is planned to use the T-REX setup in future not only for transfer experiments, but also for Coulomb excitation experiments, which would eliminate the need for lengthy setup periods between transfer and Coulex experiments. The slightly lower γ-ray detection efficiency of the T-REX setup (mainly due to the larger distance of the MINIBALL detectors from the target) is offset by the higher solid angle being covered by particle detectors as well as the larger ϑ_{lab} range covered by the particle detectors.

In order to make the Coulex setup as flexible as possible, the setup can consist of either four position sensitive strip detectors of 500 μm thickness (which were used in 2007 for the backward barrel) coupled with a CD detector (all at forward angles), the CD with two barrel detectors on the left and right (with the barrel detectors around 90°) or with just the CD detector which can be placed any chosen distance from the

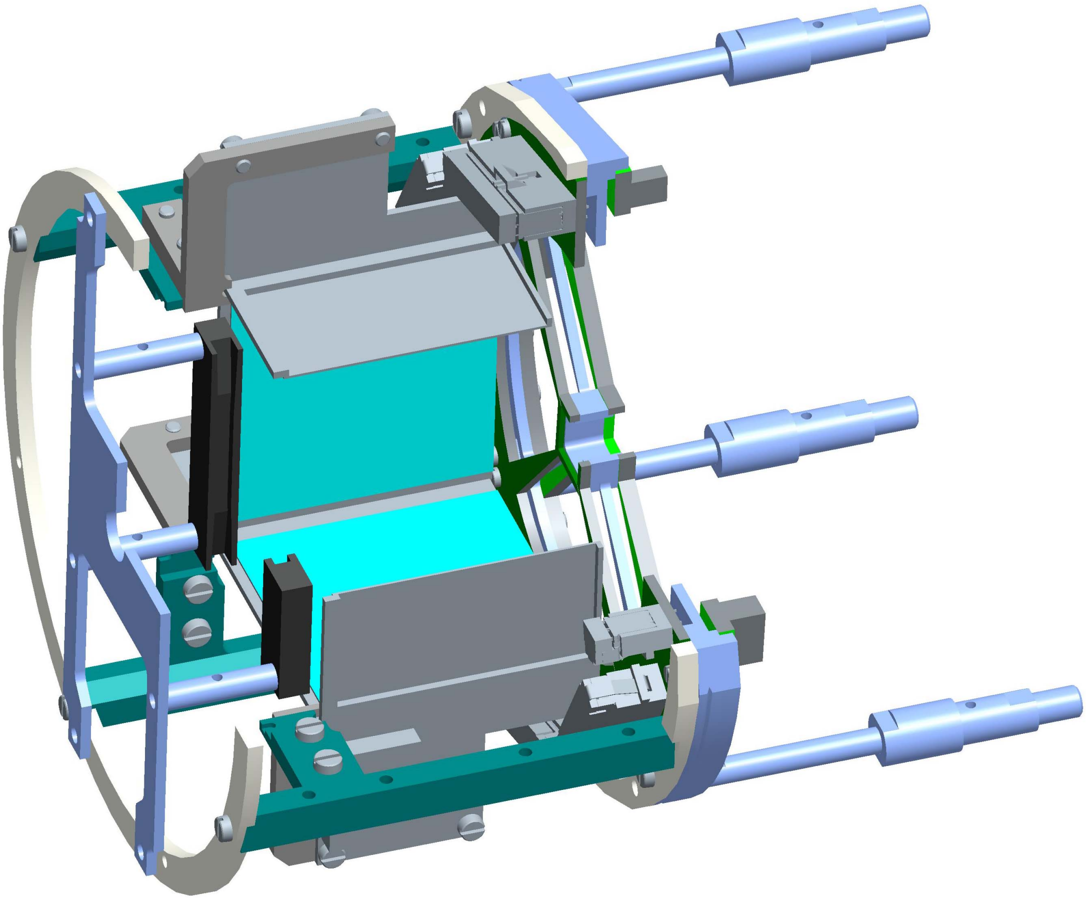

Figure E.2: Technical drawing of the planned setup for Coulomb excitation experiments with T-REX.

target, see also figure E.2. An additional barrel frame is planned which allows the use of a backward CD together with barrel detectors and a forward CD to study e.g. multi-step Coulomb excitation. This flexibility allows the adjustment of the covered ϑ_{lab} range to each experiment by changing the four bolts that attach the particle detectors to the feedthrough flange as well as those four that attach the rails to the particle detectors. For more details of the expected performance see [Wim10a].

It is planned to perform final tests of the Coulex T-REX setup (C-REX) with stable beam during the 2010 shutdown period and use it from 2011 on for Coulomb excitation experiments at REX-ISOLDE.

List of Figures

List of Tables

Bibliography

[Ame05] F. Ames, G. Bollen, P. Delahaye, et al. *Nucl. Instr. Meth. A*, **538**, 17 (2005).

[Bil05] V. Bildstein. Diplomarbeit, Universität Heidelberg (2005).
URL `http://www.mpi-hd.mpg.de/cb/theses.html`

[Boi09] H.-H. Boie. Dissertation, Universität Heidelberg (2009).
URL `http://www.ub.uni-heidelberg.de/archiv/9535`

[Boj88] J. Bojowald, H. Machner, H. Nann, et al. *Phys. Rev. C*, **38**, 1153 (1988).

[Bor04] M. Borge, J. Cederkäll, P. Delahaye, et al. *Study of neutron-rich Be isotopes with REX-ISOLDE*. CERN-INTC-2004-023 (2004). Proposal to the INTC.

[Bru97] R. Brun and F. Rademakers. *Nucl. Instr. Meth. A*, **389**, 81 (1997).
URL `http://root.cern.ch/`

[Cam75] X. Campi, H. Flocard, A. Kerman, and S. Koonin. *Nucl. Phys. A*, **251**, 193 (1975).

[Can] Canberra. *Canberra Industries, Inc.*
URL `http://www.canberra.com/`

[Cas05] R. F. Casten. *Nuclear Structure from a simple perspective* (Oxford University Press, 2005).

[Ced04] J. Cederkäll, F. Ames, P. Butler, et al. *Nucl. Phys. A*, **746**, 17 (2004).

[Cha69] B. Chambon, D. Drain, M. Yaker, et al. *Nucl. Phys. A*, **136**, 311 (1969).

[Dav02] T. Davinson. *private communication* (2002).

[Deb84] K. Debertin. *Nucl. Instr. Meth.*, **226**, 566 (1984).

[Ebe01] J. Eberth, G. Pascovici, H. Thomas, et al. *Prog. Part. Nucl. Phys.*, **46**, 389 (2001).

[Ern84] H. Ernst and K. Lesko. *IRMA code* (1984).

[Fed00] V. Fedoseyev, G. Huber, U. Köster, et al. *Hyperf. Int.*, **127**, 409 (2000).

[Goe49] M. Goeppert Mayer. *Phys. Rev.*, **75**, 1969 (1949).

[Gun00] C. Gund. Dissertation, Universität Heidelberg (2000).
URL `http://www.mpi-hd.mpg.de/cb/theses.html`

[Hab00] D. Habs, O. Kester, T. Sieber, et al. *Hyperf. Int.*, **129**, 43 (2000).

[Ham07] I. Hamamoto. *Phys. Rev. C*, **76**, 054319 (2007).

[Hax49] O. Haxel, J. Jensen, and H. Suess. *Phys. Rev.*, **75**, 1766 (1949).

[How70] A. Howard, J. Pronko, and J. C.A. Whitten. *Nucl. Phys. A*, **152**, 317 (1970).

[ISO] ISOLDE. *Homepage of the ISOLDE facility*.
URL `http://isolde.web.cern.ch/ISOLDE/`

[Kan09] R. Kanungo, C. Nociforo, A. Prochazka, et al. *Phys. Rev. Lett.*, **102**, 152501 (2009).

[Kes03] O. Kester, T. Sieber, S. Emhofer, et al. *Nucl. Instr. Meth. B*, **204**, 20 (2003).

[Kim03] I. J. Kim, C. S. Park, and H. D. Choi. *Applied Radiation and Isotopes*, **58**, 227 (2003).

[Klo93] G. Klotz, P. Baumann, M. Bounajma, et al. *Phys. Rev. C*, **47**, 2502 (1993).

[Kon03] A. Koning and J. Delaroche. *Nucl. Phys. A*, **713**, 231 (2003).

[Kös03] U. Köster, V. N. Fedoseyev, A. N. Andreyev, et al. *Nucl. Instr. Meth. B*, **204**, 347 (2003).

[Krö10] T. Kröll, M. von Schmid, J. Leske, et al. *Study of single particle properties of neutron-rich Na isotopes on the "shore of the island of inversion" by means of neutron-transfer reactions*. CERN-INTC-2010-007 (2010). Proposal to the INTC.

[Kug00] E. Kugler. *Hyperf. Int.*, **129**, 23 (2000).

[Lau04] M. Lauer. Dissertation, Universität Heidelberg (2004).
URL `http://www.mpi-hd.mpg.de/cb/theses.html`

[Lin08] M. Lindroos, P. Butler, M. Huyse, and K. Riisager. *Nucl. Instr. Meth. B*, **266**, 4687 (2008).

[Loh74] J. M. Lohr and W. Haeberli. *Nucl. Phys. A*, **232**, 381 (1974).

[Lut67] H. Lutz, J. Wesolowski, L. Hansen, and S. Eccles. *Nucl. Phys. A*, **95**, 591 (1967).

[Lut03] R. Lutter, O. Schaile, K. Schöffel, K. Steinberger, and C. Broude. *MARaBOU data aquisition system* (2003).
URL `http://www.bl.physik.uni-muenchen.de/marabou/html/`

[Lut05] R. Lutter. *MED data structure* (2005).
URL `http://www.bl.physik.uni-muenchen.de/marabou/html/doc/MedStructure.pdf`

[Mac05] H. Mach, L. M. Fraile, O. Tengblad, et al. *Eur. Phys. J. A*, **25**, 105 (2005).

[Mah08] M. Mahgoub. Dissertation, TU München (2008).

[Mar05] F. Maréchal, D. L. Balabanski, D. Borremans, et al. *Phys. Rev. C*, **72**, 044314 (2005).

[Mes] Mesytec. *mesytec GmbH & Co. KG*.
URL http://www.mesytec.com/

[Mic] Micron. *Micron Semiconductor Ltd.*
URL http://www.micronsemiconductor.co.uk/

[Mil09] D. Miller, P. Adrich, B. A. Brown, et al. *Phys. Rev. C*, **79**, 054306 (2009).

[Mot95] T. Motobayashi, Y. Ikeda, K. Ieki, et al. *Phys. Lett. B*, **346**, 9 (1995).

[Nan69] H. Nann, R. Bass, K. Groeneveld, and F. Saleh-Bass. *Zeitschrift der Physik*, **218**, 190 (1969).

[Ney05] G. Neyens, M. Kowalska, D. Yordanov, et al. *Phys. Rev. Lett.*, **94**, 022501 (2005).

[Nie05] O. Niedermaier, H. Scheit, V. Bildstein, et al. *Phys. Rev. Lett.*, **94**, 172501 (2005).

[Nil55] S. G. Nilsson. *Dan. Mat. Fys. Medd.*, **29** (1955).

[NIS] NIST. *National institute of standards and technology - x-ray mass attenuation coefficients - germanium*.
URL http://physics.nist.gov/PhysRefData/XrayMassCoef/ElemTab/z32.html

[NND] NNDC. *National nuclear data center - decay radiation of ^{152}Eu*.
URL http://www.nndc.bnl.gov/chart/decaysearchdirect.jsp?nuc=152Eu&unc=nds

[Now1x] K. Nowak. Dissertation, TU München (201x).

[Oos83] A. V. Oosterom and J. Strackee. *IEEE Trans. Biomed. Eng.*, **30**, 125 (1983).

[Orl09] R. Orlandi, R. Chapman, J. Smith, et al. *Probing the $n = 50$ shell gap near ^{78}Ni*. CERN-INTC-2009-017 (2009). Proposal to the INTC.

[Ost02] A. Ostrowski, S. Cherubini, T. Davinson, et al. *Nucl. Instr. Meth. A*, **480**, 448 (2002).

[Ots01] T. Otsuka, R. Fujimoto, Y. Utsuno, et al. *Phys. Rev. Lett.*, **87**, 082502 (2001). See also the Comment [Zuk03] and the Reply [Ots03].

[Ots02] T. Otsuka, Y. Utsuno, R. Fujimoto, et al. *Eur. Phys. J. A*, **15**, 151 (2002).

[Ots03] T. Otsuka, R. Fujimoto, Y. Utsuno, et al. *Phys. Rev. Lett.*, **91**, 179202 (2003). Reply to comment [Zuk03].

[Ots05] T. Otsuka, T. Suzuki, R. Fujimoto, H. Grawe, and Y. Akaishi. *Phys. Rev. Lett.*, **95**, 232502 (2005).

[Ots06] T. Otsuka, T. Matsuo, and D. Abe. *Phys. Rev. Lett.*, **97**, 162501 (2006).

[Ots10a] T. Otsuka, T. Suzuki, J. D. Holt, A. Schwenk, and Y. Akaishi. *Phys. Rev. Lett.*, **105**, 032501 (2010).

[Ots10b] T. Otsuka, T. Suzuki, M. Honma, et al. *Phys. Rev. Lett.*, **104**, 012501 (2010).

[Pan05] M. Pantea. Dissertation, TU Darmstadt (2005).

[Pat08] N. Patronis, R. Raabe, N. Bree, et al. *One nucleon transfer reactions around* ^{68}*Ni at REX-ISOLDE*. CERN-INTC-2008-007 (2008). Proposal to the INTC.

[Per76] C. M. Perey and F. G. Perey. *Atomic Data and Nuclear Data Tables*, **17**, 1 (1976).

[Rod08] T. Rodriguez and J. Egido. *private communication* (2008).

[Sch83] F. J. Schima and D. D. Hoppes. *Int. J. Appl. Radiat. Isot.*, **34**, 1109 (1983).

[Sei1x] M. Seidlitz and P. Reiter. *to be published* (201x).

[Str] Struck. *Struck Innovative Systeme GmbH*.
URL `http://www.struck.de/`

[Ter08] J. R. Terry, B. A. Brown, C. M. Campbell, et al. *Phys. Rev. C*, **77**, 014316 (2008).

[Thi75] C. Thibault, R. Klapisch, C. Rigaud, et al. *Phys. Rev. C*, **12**, 644 (1975).

[Tho06] I. Thompson. *FRESCO, coupled reaction channels calculations* (2006).
URL `http://www.fresco.org.uk`

[Tho09] I. J. Thompson and F. M. Nunes. *Nuclear reactions for Astrophysics* (Cambridge University Press, 2009).

[Uts04] Y. Utsuno, T. Otsuka, T. Glasmacher, T. Mizusaki, and M. Honma. *Phys. Rev. C*, **70**, 044307 (2004).

[War08] N. Warr. *MINIBALL electronics at may 2008* (2008).
URL `http://www.ikp.uni-koeln.de/~warr/doc/electronics_May2008.pdf`

[Wei06] W. Weinzierl. Diplomarbeit, TU München (2006).

[Wim09] K. Wimmer, R. Krücken, V. Bildstein, et al. *Study of the onset of deformation and shape coexistence in* ^{46}*Ar via the inverse kinematics (t,p) reaction*. CERN-INTC-2009-034 (2009). Proposal to the INTC.

[Wim10a] K. Wimmer. Dissertation, TU München (2010).

[Wim10b] K. Wimmer, T. Kröll, R. Krücken, et al. *Phys. Rev. Lett.*, (2010).

[XIA] XIA. *X-ray instrumentation associates (XIA)*.
URL `http://www.xia.com/`

[Zuk03] A. P. Zuker. *Phys. Rev. Lett.*, **91**, 179201 (2003). Comment on [Ots01]. See also the Reply [Ots03].

Acknowledgments

Finally I would like to thank everybody who helped, assisted, and supported me during the thesis.

Special thanks go to Reiner Krücken for giving me the wonderful opportunity to not just build a new setup but also use it for a nice experiment. I would also like to thank Roman Gernhäuser for his always open door and the constructive criticism during the whole thesis. I'm grateful to Thorsten Kröll for bearing with me, our discussions on physics, whisky and everything else. I owe Kathrin Wimmer a deep debt of gratitude for the collaboration, helping understand the analysis and solving my FRESCO problems.

I'm very grateful to Rudi Lutter for his support with the data acquisition and lively discussions about good programming habits. I want to offer many thanks to Ludwig Maier for his support and tips for the programming of the analysis, testing the integrator, learning to administer our computer system, and many discussions on (non-)physics topics. The development of the detector PCBs and the electronics developed in this thesis would not have been possible without the help of Michael Böhmer, who also made sure that the caffeine supply of E12 never ran out.

The experiment and the development of T-REX would not have been possible without the REX-ISOLDE team, in particular Frederik Wenander and Didier Voulot, and the T-REX collaboration, of which I would like to set Piet Van Duppen apart, a great supporter from the very beginning on. Many thanks go also to the workshop of E12, thank you Ralf and Michi for making the construction of T-REX possible by helping with all our last minute modifications.

I will forever be indebted to my office mates, Katrin Eppinger/Straub, Anuj Parikh, Kathrin Wimmer, Konrad Steiger and Clemens Herlitzius for the moral support, coffee breaks, organizing (and winning) the USSO, and generally for making my time at E12 enjoyable.

My time in Munich would not have been as enjoyable as it was without the great friends I've found in my room mates Höbl, Tobi and Sush, thanks for the great time.

Finally I would like to thank my friends and my family for their support, encouragement, and the distraction from physics.